Experimental Investigation of the Generalised Multi-Band Carrier-less Amplitude and Phase Modulation in Visible Light Communications

Khald Abdelrhiem Werfli

A thesis submitted in partial fulfilment of
the requirements of the University of
Northumbria at Newcastle for the degree of
Doctor of Philosophy

Research undertaken at the Faculty of Engineering
and Environment

March 2018

Abstract

The existing lighting infrastructure for homes and offices features a number of lighting sources that are used in order to provide the required level of illumination. This can be utilised, from the communications point of view, to increase the data throughput in visible light communication (VLC) systems. In general, VLC systems, which utilise white light-emitting diodes (LEDs), only offer a bandwidth limited to the lower MHz region. Therefore, realising VLC-based high data rate communication systems is a challenging task. In the last decade, numerous solutions were proposed to overcome the LED's limited bandwidth. One of straight forward solutions is to adopt an advanced modulation technique such as carrier-less amplitude and phase (CAP) or orthogonal frequency division multiplexing.

In this thesis, a solution based on multiplexing in both the frequency and space domains is proposed. This thesis investigates and analyses the performance of a new modulation scheme, known as multi-band carrier-less amplitude and phase (*m*-CAP) modulation, within the context of VLC. The principle of *m*-CAP is outlined and to further enhance its bandwidth performance the decision feedback equaliser (DFE) is proposed.

An experimental investigation of the *m*-CAP VLC system shows that a transmission data rate of 31.5 Mb/s over a link span *L* of 1 m is possible in an indoor environment. Coupling DFE with high order *m*-CAP systems (i.e., $m = 5, 10$) is found to be impractical, due to the ability of *m*-CAP in mitigating the inter-symbol interference imposed by the limited LED's bandwidth. In addition, the impact of some of the utilised parameters, such as the roll-off factor and the pulse shaping finite impulse response (FIR) filter length, on the performance of *m*-CAP-VLC links is investigated. The proposed new *m*-CAP system offers 80%, 75%, ~67% and 50% in system complexity, which is achieved by reducing the number of FIR filters in comparison with the conventional 10, 8, 6, and 4-CAP, respectively. In addition, by adopting a nonuniform distribution of *m* over the total signal bandwidth B_{tot} (i.e., variably distributing the bandwidth of the allocated sub-carriers so that *x* sub-carriers are located within the LED's modulation bandwidth B_{mod} region, and the remaining $y = m\text{-}x$ sub-carriers are spread equally on the across of the roll-off region of the LED's frequency response), an improvement in the data transmission of ~36% for the $6_{1/5}$-CAP scheme is attainable in comparison to the conventional 6-CAP system. Results show that, both imaging multiple-input multiple-output (MIMO) and *m*-CAP have a remarkable capabilities to improve transmission speeds in VLC systems, and hence, here, the two schemes are combined to further improve the net transmission data rate.

In addition, an experimental test-bed of a 4 × 4 imaging MIMO based *m*-CAP VLC system (i.e., space multiplexing) is developed in order to assess and validate the proposed system performance. Furthermore, an investigation of the link performance as a function of the number of sub-carriers *m*, *L*, and signal bandwidth B_{sig}, is carried out. For all values tested, a maximum data rate of ~249 Mb/s is achieved for $m = 20$, $B_{sig} = 20$ MHz, and $L = 1$ m, at a bit error rate of 3.2×10^{-3}, using LEDs with ~4 MHz bandwidth.

Table of Contents

List of Figures

List of Tables

Glossary of Abbreviations

A/D	Analogue to digital
AFG	Arbitrary function generators
ANN	Artificial neural network
APD	Avalanche photodetector
ASK	Amplitude shift keying
AWGN	Additive white Gaussian noise
BER	Bit error rate
BPSK	Binary phase shift keying
CAP	Carrier-less amplitude and phase
CP	Cyclic prefix
DC	Direct current
D/A	Digital to analogue
DD	Direct detection
DFE	Decision feedback equaliser
DMT	Discrete multi-tone
DSL	Digital subscriber lines
EVM	Error vector magnitude
FDM	Frequency division multiplexing
FEC	Forward error correction
FET	Field-effect transistor
FFT	Fast Fourier transform
FIR	Finite impulse response
FOV	Field of view
FPGA	Field programmable gate array
FSO	Free space optical
GaAs	Gallium arsenide
GaN	Gallium nitride
ICI	Inter-carrier interference
IFFT	Inverse fast Fourier transform
IM	Intensity modulation
IoT	Internet-of-Things
IR	Impulse response

ISI	Inter-symbol interference
ITU	International telecommunications union
LED	Light emitting diode
Li-Fi	Light fidelity
LMS	Least mean squares
LOS	Line-of-sight
LPF	Low-pass filter
m-CAP	Multi-band CAP
MIMO	Multiple-input multiple-output
MISO	Multiple-input single-output
OFDM	Orthogonal frequency division multiplexing
O-OFDM	Optical orthogonal frequency division multiplexing
OOK	On-off keying
OPPM	Overlapping PPM
OWC	Optical wireless communications
PAM	Pulse amplitude modulation
PAPR	Peak-to-average power ratio
PD	Photodetector
PPM	Pulse position modulation
PRBS	Pseudo-random binary sequence
P/S	Parallel to serial
PSD	Power spectral density
PSK	Phase shift keying
QAM	Quadrature amplitude modulation
RC	Resistor and capacitor
RF	Radio frequency
RGB	Red, green and blue
RLS	Recursive least squares
Rx	Receiver
SISO	Single-input single-output
SNR	Signal-to-noise ratio
S/P	Serial to parallel
SRRC	Square root raised cosine
SSD	Signal space diversity
SSL	Solid-state lighting
TIA	Transimpedance amplifier

Tx	Transmitter
VLC	Visible light communications
WDM	Wavelength division multiplexing
Wi-Fi	wireless fidelity
WPLED	White phosphor LED
ZFE	Zero forcing equaliser

Glossary of Symbols

b	Number of bits/symbol
b_n	Filter tap coefficients value of the feedback filters
B_{ch}	Channel bandwidth
B_{mod}	Modulation bandwidth
B_{Rx}	Receiver bandwidth
B_{sc}	Sub-carrier bandwidth
B_{sig}	Signal bandwidth
B_{sys}	System bandwidth
B_{tot}	Total signal bandwidth
c_n	Filter tap coefficients value of the feedforward filters
C_{pu}	Fixed capacitance of PD per unit area
d	Number of reflections
$\hat{d}_{m-n}$	Estimate of the previous symbol
d_r	Spacing between Rxs
d_t	Spacing between Txs
f	Frequency
f_c	Carrier frequency
$f_{I,i}(t)$	Impulse responses of the in-phase SRRC filters
$f_{I,i}(-t)$	Time reversed $f_{I,i}(t)$
$f_{Q,i}(t)$	Impulse responses of the quadrature SRRC filters
$f_{Q,i}(-t)$	Time reversed $f_{Q,i}(t)$
f_l	Lens focal length
$f_{3\text{dB}}$	Cut-off frequency
$g_{I,i}(t)$	In-phase up-sampled signal
g_m	FET transconductance
$g_{Q,i}(t)$	Quadrature up-sampled signal
G	Open-loop voltage gain
$h(t)$	Channel impulse response
$H(f)$	Transfer function
I_p	Photo current
I_{bg}	Background light induced current

I_c	Current
I	In-phase
I_2, I_3	Bandwidth factors
k	Boltzmann's constant
L	Link span
L_f	Filter length
L_r	Distance between the lens and the Rx
L_s	Truncated symbols
L_t	Distance between the Tx and the lens
m	Number of sub-carriers
M	QAM cardinality
η_{net}	Net spectral efficiency
n_{samp}	Number of samples/symbol
η_s	Spectral efficiency
$n(t)$	Noise signal
N_s	Number of symbols
N_o	Total noise variance
N_1	Length of the feedforward filters
N_2	Length of the feedback filters
P_{dc}	DC power
P_f	Continues signal power
P_{max}	Maximum normalised ideal symbol power
P_r	Average received signal power
P_t	Average transmit power
q	Electron charge
Q	Imaginary
R	Resistor
R_b	Data rate
R_{net}	Net data rate
$S_r(n_s)$	Received symbols
$S_t(n_s)$	Ideal transmitted symbols
T_b	Symbol duration
T_k	Absolute temperature
T_s	Symbol duration
$x_{QAM}(t)$	QAM constellation symbols
$x(t)$	Continuous optical signal

y_{m-n}	Current symbol
$y(t)$	Received signal
$Y(f)$	Fourier transform of the system response
α	Magnification factor of a lens
β	Roll-off factor
$\sigma_{thermal}^2$	The thermal noise variance
σ_{shot}^2	The ambient induced shot noise variance
Υ	FET channel noise factor
ζ	Minority carrier lifetime
ζ_{NR}	Non-radiative components
ζ_R	Radiative components
$\mathcal{R}$	PD's responsivity
$\otimes$	Convolution

Dedications

To the most important people in my life, my parents, wife and two children Salam and Abdulraheem. Also, to whom might find this thesis useful.

Acknowledgments

First, I would like to express my deepest apology in case I have unintentionally missed anyone.

Second, I would like to express my thanks to my sponsor the Libyan government, which without their financial support this PhD journey would not have been possible.

Third, a sincere special thanks goes to my principle supervisor Professor Zabih (Fary) Ghassemlooy for his advice, guidance, constant enthusiasm and support throughout this PhD journey. Without his constant and unlimited support, this work would not has been accomplished on time. Thank you so much Fary.

Fourth, besides my advisor, I am highly indebted to Dr Paul. A. Haigh for his valuable support and help. Also, my thanks and appreciation goes to Navid Bani Hassan and Dr Andrew Burton, Sincere thanks guys.

Fifth, I would like to express my sincere thanks to my colleagues from Czech Technical University in Prague Professor Stanislav Zvanovec and Petr Chvojka for the valuable collaboration and technical feedback through my PhD journey.

Finally, I specially thank my parents and my partner Anisa for her, encouragement, patience, understanding, and unlimited support that she has provided to me throughout all my PhD study from the first day up to the end. I also would like to acknowledge the joy that my little two angels Salam and Abdulraheem brought to my life.

Declaration

I hereby declare that this thesis is entirely my own work and that I have exercised reasonable care to ensure that the work is original, and does not to the best of my knowledge breach any law of copyright, and has not been submitted in support of another degree or qualification.

I declare that the Word Count of this Thesis is 33,846 words

Signature:

Name: Khald Werfli

Date: 05th March 2018

Chapter 1 INTRODUCTION

1.1 Background

Since the dawn of humanity, light has been utilised for illumination purposes, transitioning from the simple use of fire for illumination and breaking through towards the use of more advanced technologies such as traditional incandescent and fluorescent bulbs. In addition to illumination, light has also been used to convey information, as humankind, throughout history, has been able to convey messages through short and long distances using natural resources. For instance, as far back as 800 BC, ancient Romans and the Chinese used fire beacons to convey messages of an invading threat by foreigners. Moreover, around 150 BC, native Indian Americans used smoke as a way of communications in order to send information over vast distances [1]. Light is also widely used for navigation purposes such as navigating ships through harbours. In early 1880, the world witnessed the birth of the first sophisticated practical demonstration of an optical communications system "Photophone" by the Scottish scientist Alexander Graham Bell [2]. Bell successfully managed to modulate and send his voice onto sunlight by oscillating a mirror placed at the transmitter (Tx), which alternated the amount of light reflected from its surface towards the receiver (Rx). In the experimental setup, the Rx consisted of a selenium cell that was placed within the focal point range of a parabolic mirror in to order to convert the optical signal into an electrical current. A successfully

communicated link distance of 213 m from Franklin school to Bell's laboratory in Washington D.C. was achieved. Less than a hundred years later, in 1962, James R. Biard "Bob" and Gary E. Pittman from the Semiconductor Research and Development Laboratory in Texas Instruments invented the first p-n junction infrared light emitting diode (LED) using gallium arsenide (GaAs) as a semiconductor material [3].

As the semiconductor technology became more mature, a new era of the so-called solid-state lighting (SSL) emerged, where an extensive amount of research work on the subject was done by physics. Later in the same year, i.e., 1962, Nick Holonyak Jr. and S.F. Bevacqua of General Electric developed the first visible-spectrum red-LED using GaAs phosphide (GaAsP) [4]. Since then, the sustained rapid development of SSL technology has enabled the invention of improved LEDs with different wavelengths such as green, yellow and orange [5]. The real breakthrough towards achieving a white light illumination source utilising LED technology was not realised until 1994, when Shuji Nakamura, T. Mukai and M. Senoh published a letter in Applied Physics demonstrating the first practical blue LED using gallium nitride (GaN) as a semiconductor material [6]. Thanks to the invention of the blue LED, the first practical white LED was manufactured a few years later in 1996 by the means of coating the blue emitters with a yellow layer [1, 7, 8]. In addition to the illumination functionality, LEDs provide the extra capability of encoding data onto light beams. This has enabled the invention of optical wireless communications (OWC), and its sub-disciplines visible light communications (VLC), and free space optical (FSO) communications [9, 10].

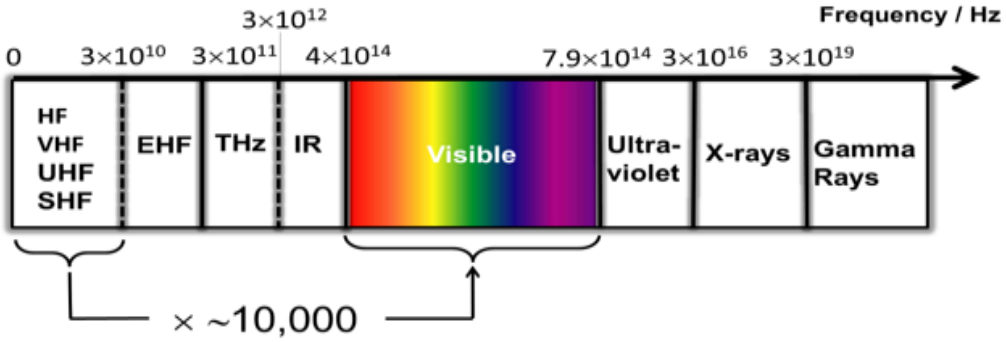

Figure 1.1. Frequency distribution of the visible light spectrum, RF and other electromagnetic radiation portions of the electromagnetic spectrum [11]

VLC has gained a lot of research attention over the past two decades due to the significant advantages it offers such as a huge unregulated ~400 THz bandwidth (i.e., free license) in the ~380-780 nm band of the electromagnetic spectrum, which is visible to the human eye and occupies ~10,000 times larger portion of the electromagnetic spectrum than the radio frequency (RF). In addition, VLC offers higher power efficiency, worldwide availability and environmentally green, no health hazard, RF-interference free communications [1, 12-15]. The frequency distribution of visible light, RF and other electromagnetic radiation portions of the electromagnetic spectrum are shown in Figure 1.1 (adopted from [11]). VLC utilises LEDs as the source of illumination as opposed to traditional incandescent or fluorescent bulbs due to their low cost and lower power consumption (> 50% energy efficiency) [1]. A key advantage of LEDs over other light sources is that they can be modulated at very high speeds that exceed the human eye perception (>> 100 Hz), which enables them to meet the requirements of human eyes safety. Thus, LEDs offer a unique ability of combining the implementation of solid-state illumination with data transmissions. Moreover, implementing VLC systems that utilise LEDs can provide additional advantages including high brightness levels, longer life span, environment friendliness, reliability, inherent data security, higher data rates transmission and compatibility with existing infrastructures [1, 13, 16].

All of these features make VLC one of the most promising technologies for satisfying the end users' demands for capacity and offering a complementary alternative to the dominant traditional RF-based communication technologies for indoor wireless data communication applications. More recently, VLC has been dubbed as light fidelity (Li-Fi) [17] in accordance with wireless fidelity (Wi-Fi) nomenclature in the RF domain.

1.2 Problem Statement and Motivations

As introduced in the previous section, VLC is an emerging OWC technology that utilises the vast unlicensed visible light portion of the electromagnetic spectrum and provides a dual functionality of illumination and data communications simultaneously [14, 15]. Nowadays, the ever-growing traffic on wireless networks due to the increased use of mobile devices and the emergence of Internet-of-Things (IoT)) has led to a tremendous demand for reliable high-speed data communications. Cisco forecasts that by 2020 the demand for the data traffic will exceed the boundary of 30 EB/month (in particular categories: web, data and voice over IP - 5 EB/month; video streaming - 23 EB/month; audio streaming - 1.8 EB/month; file sharing - 0.6 EB/month), thus indicating a growth of 53% annually from 2015 (web, data and voice over IP 31%, video 62%, audio 45%, file sharing 66%) [18]. The existing RF technology is facing a serious challenge in dealing with such data traffic growth, thus resulting in a spectral congestion. As a relief to the traditional spectrum-limited and expensive RF-based wireless communication systems, VLC can be utilised as a complementary communication method in order to help unlock the spectrum congestion that RF-based communication systems currently encounter, thus contributing towards achieving a high data communication infrastructure [15, 19, 20]. As an example, the current UK RF allocation chart is shown in Figure 1.2 (adopted from [21]). In order to enable a comparison between the traditional RF-based communication

systems and VLC systems, a number of key parameters have been summarised in Table 1.1. Compared to RF-based links, VLC systems offer an inherent security advantage as the light beam is well confined and cannot penetrate through the surfaces of the surrounding environment. In addition, another key parameter for VLC-based links is that the light beam can be controlled and focused by means of lenses and diffractive elements, therefore boosting the received power at the Rx, unlike RF-based links where the radiation pattern is difficult to restrain within the antenna size. VLC also offers the capability of delivering low interference communications as the light beam does not suffer from RF interference.

The advantages mentioned above along with VLC systems' low cost, high power efficiency and compatibility with existing infrastructure [1, 14] have led to significant number of research investigations on VLC systems among the scientific community in the past decade, as evident by the large volume of research and development results being reported (e.g., [15, 22-26]) and the references therein. In VLC both data communications and illumination are achieved by means of intensity modulation (IM) of an LED and direct detection (DD) using a photodetector (PD) [14].

Table 1.1. Comparison of RF-based links and VLC technology; adopted from [1, 27]

Property	**RF**	**VLC**
Bandwidth	Limited, regulated and congested	Huge and unregulated ~400 THz
Infrastructure	Requires custom infrastructure (i.e., base station and terminal)	Can use the existing LEDs lighting infrastructure
Licencing	Licensed and expensive	Free (i.e., Unlicensed)
Signal confinement	Can penetrate the walls	Cannot penetrate the walls (i.e., inherent security advantage)
Provided service	Communications	Illumination + communications
Noise source	Electrical and electronic components	Ambient light and Sun light
Mobility	Good	Limited
Radiation pattern control	Difficult to restrict on antenna size	High ability of control when using lenses and diffractive elements

Typical LEDs based on blue emitters with yellowish wavelength-conversion phosphors known as white phosphor LEDs (WPLEDs) are the most popular type of transmitters adopted in VLC systems due to their ease of use and commercial availability. Another popular method to generate white light is by combining three LEDs, red, green and blue (RGB LEDs). However, this method suffers from the difficulty of maintaining the colour balance between the three different chips as the colour of each may change overtime. From the data communications point of view, the second method (i.e., RGB) provides higher modulation bandwidth B_{mod} in the range of tens of MHz. However, it requires an extra signal-processing element to be added in order to maintain the colour balancing. On the other hand, the commercially available WPLEDs provide a limited B_{mod} in the range of low MHz (typically < 5 MHz) due to the slow transit response of the phosphor [28, 29]. In general, VLC-based systems are considered as one of the most promising

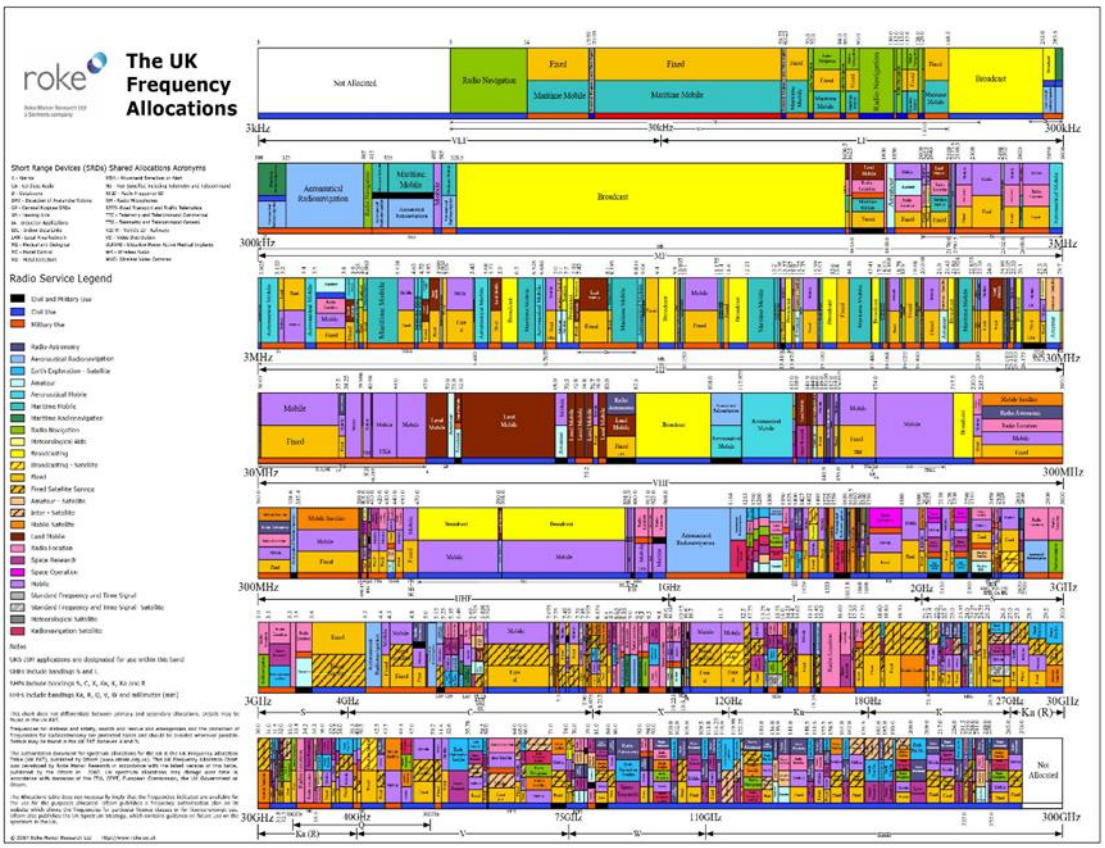

Figure 1.2. The current UK RF spectrum demonstrating significant congesting [21]

technologies for satisfying the exponentially growing demand for higher data transmission capacity [30].

However, VLC systems face a number of challenges including (*i*) the limited B_{mod} of LEDs (typically < 5 MHz, or higher for micro-LEDs (B_{mod} > 20 MHz [31])); (*ii*) LED non-linearity; (*iii*) multipath induced inter-symbol interference (ISI); (*iv*) diming; (*v*) blocking and shadowing; and (*vi*) limited mobility, which restricts the maximum achievable data rate R_b within a typical indoor environment [14, 32, 33].

Numerous schemes have been proposed to overcome these limitations [28, 29, 34-37]. For instance, for B_{mod} and ISI limitations, the most widely adopted schemes include pre- and post-equalization, blue filtering (i.e., using a narrowband blue filter to pass the fast blue component and block the slow phosphor component at the Rx side), multiplexing and parallel transmission, spectrally efficient modulation and multi-carrier transmission [38-40]. By using the blue filtering technique, B_{mod} has been significantly improved from 3 up to 20 MHz [41]. However, the use of a blue filter results in the rejection of up to 50% of the signal power [42], causing a substantial degradation in the signal-to-noise ratio (SNR). In literature it has been shown that, a higher transmission speed can be achieved when equalizing the white component in the high SNR environment than when using a blue filter [35]. Implementing different equalization techniques at the Tx and the Rx is an another popular solution to overcome the B_{mod} limitations [35, 43]. The problem with using equalization techniques such as the one based on the artificial neural network reported in [35] is that they are highly computationally complex.

One of the most popular solutions to overcome the B_{mod} limitation is to adopt an advanced modulation technique such as orthogonal frequency division multiplexing (OFDM) or carrier-less amplitude and phase (CAP) modulation [44, 45]. The use of OFDM offers improved spectral usage when compared with binary modulation schemes such as on-off

keying (OOK). Transmission speeds higher than 5.6 Gb/s have been reported using OFDM with wavelength division multiplexing (WDM) and making use of the bit and power loading techniques [46, 47]. Despite the numerous advantages that OFDM offers, there are a number of drawbacks including (*i*) limited dynamic range, (*ii*) relatively high peak-to-average power ratio (PAPR) due to the LED nonlinearity [44, 46, 48]; (*iii*) sensitivity to the carrier offset and drift, and phase noise; which results in lower overall spectral efficiency [49-51].

Another alternative to OFDM is the CAP modulation scheme, which has been reported to outperform OFDM when operating over the same physical link [47]. Transmission speeds of 1.32 Gb/s and 1.08 Gb/s at a bit error rate (BER) of 10^{-3} have been achieved with CAP and OFDM, respectively, when utilising the blue LED indicating an improvement of ~20% [47].

Throughout this research, the main focus will be dedicated towards the improvement of the limited B_{mod} associated with LEDs, which is the main bottleneck in achieving a high data rate transmission infrastructure utilising VLC. This will be achieved by the means of introducing and analysing a new version of CAP known as multi-band CAP (*m*-CAP). The *m*-CAP scheme is implemented by simply dividing the conventional CAP signal into non-orthogonal frequency-division multiplexed sub-carriers. The *m*-CAP format proposes that the frequency attenuation over small sub-bands will be less than that over the entire Bandwidth and hence a lower error rate can be achieved.

1.3 Research Objectives

This research aims to conduct a theoretical and experimental investigation into the performance of the proposed *m*-CAP scheme, with the vision of providing an insight into its benefits and limitations. Moreover, the research also aims to investigate the potential improvement in data throughput that can be achieved by utilising the new *m*-CAP scheme in VLC systems. In order to achieve this, a list of research objectives are outlined as follows:

- Review the fundamentals concept of VLC systems, and understand the technical challenges facing it.
- Review the basics of the proposed *m*-CAP scheme and realise its potential ability in improving VLC systems' performance.
- Evaluate the performance of the *m*-CAP scheme in conjunction with the most efficient equalisation technique.
- Investigate numerically and experimentally the proposed system by assessing the impact of parameters such as the roll-off factor and the pulse shaping filter length, on the bit error rate performance, data throughput, and spectral efficiency of VLC systems.
- Investigate the performance of the *m*-CAP scheme when non-equal sharing of the available signal bandwidth over the number of sub-carriers is implemented.
- Investigate the potential improvement in VLC systems' performance when introducing multiplexing in both the frequency and space domains.

1.4 Thesis Organisation

This thesis is arranged into seven chapters. Chapter One highlights the challenges facing VLC systems, as well as the research motivations and objectives. Following Chapter One, Chapter Two outlines the fundamental principles of VLC systems, including the Tx and Rx structures and the channel model. The methods of generating white light utilising LEDs are also discussed. Moreover, the sources of noise affecting VLC links are defined. The concept of the limited modulation bandwidth imposed by LEDs is also discussed, as well as the parameters that influence the LED bandwidth. Finally, the chapter concludes by providing a review of the most famous single-carrier and multi-carrier modulation schemes used in VLC systems.

Chapter Three covers the fundamentals of the proposed *m*-CAP scheme and provides a detailed explanation of the *m*-CAP signals generation. Furthermore, as a proof of a concept, a practical investigation of the performance of the *m*-CAP scheme is presented for the first time in the context of VLC systems. Finally, the impact of increasing the number of sub-carriers on the achieved data throughput and spectral efficiency is investigated. Chapter Four explores the impact of implementing the proposed *m*-CAP scheme in conjunction with the most efficient equalisation technique. The impact of different pulse shaping filters parameters, such as the roll-off factor and the filter length, on the bit error rate, data transmission, and spectral efficiency of the *m*-CAP scheme is theoretically and experimentally investigated.

The development of the proposed novel *m*-CAP concept based on un-equally sharing the signal bandwidth over the number of sub-carriers are presented in Chapter Five. Also provided is a comparison, conducted by means of MATLAB simulations, between the new and the conventional *m*-CAP schemes, in terms of computational complexity and the bit error rate (BER) performance. Furthermore, the impact of variably distributing the

signal bandwidth over the number of sub-carriers is discussed. Chapter Six provides a detailed description of an experiment implementing a 4 × 4 imaging multiple-input multiple-output (MIMO) VLC system (i.e., space multiplexing) utilising *m*-CAP modulation (i.e., frequency multiplexing). Moreover, a practical investigation into the impact of varying a range of parameters, such as number of sub-carriers, transmission distance, and signal bandwidth, on the performance of *m*-CAP is presented. In the experiment, an imaging lens is utilised in order to focus each light beam on its corresponding PD.

Finally, in Chapter Seven, all key findings are summarised and recommendations for future work are provided.

1.5 Original Contributions

As outcomes of the conducted research, the following original contributions to the research field have been made:

1. Demonstrating an experimental implementation of the *m*-CAP VLC system over a transmission distance of 1 m, see Chapter Three.
2. Demonstrating, through numerical simulations, the significance of combining the *m*-CAP scheme with the most efficient equalision technique. Furthermore, numerical and experimental investigations of the impact of utilising different *m*-CAP scheme parameters on the performance of VLC links in terms of the BER, data transmission speed, and spectral efficiency, see Chapter Four.
3. Proposed a novel *m*-CAP scheme based on unequally distributing the available signal bandwidth, such that the first sub-carrier bandwidth is made to be the same as the LED's bandwidth, and the remaining signal bandwidth is shared equally between the remaining sub-carriers, see Chapter Five.

4. Experimentally investigate the performance of the *m*-CAP imaging MIMO-VLC system as function of a number of parameters, such as the number of sub-carriers, transmission span, and signal bandwidth, see Chapter Six.

The aforementioned original contributions are further summarised in Figure 1.3 and have led to the following publications:

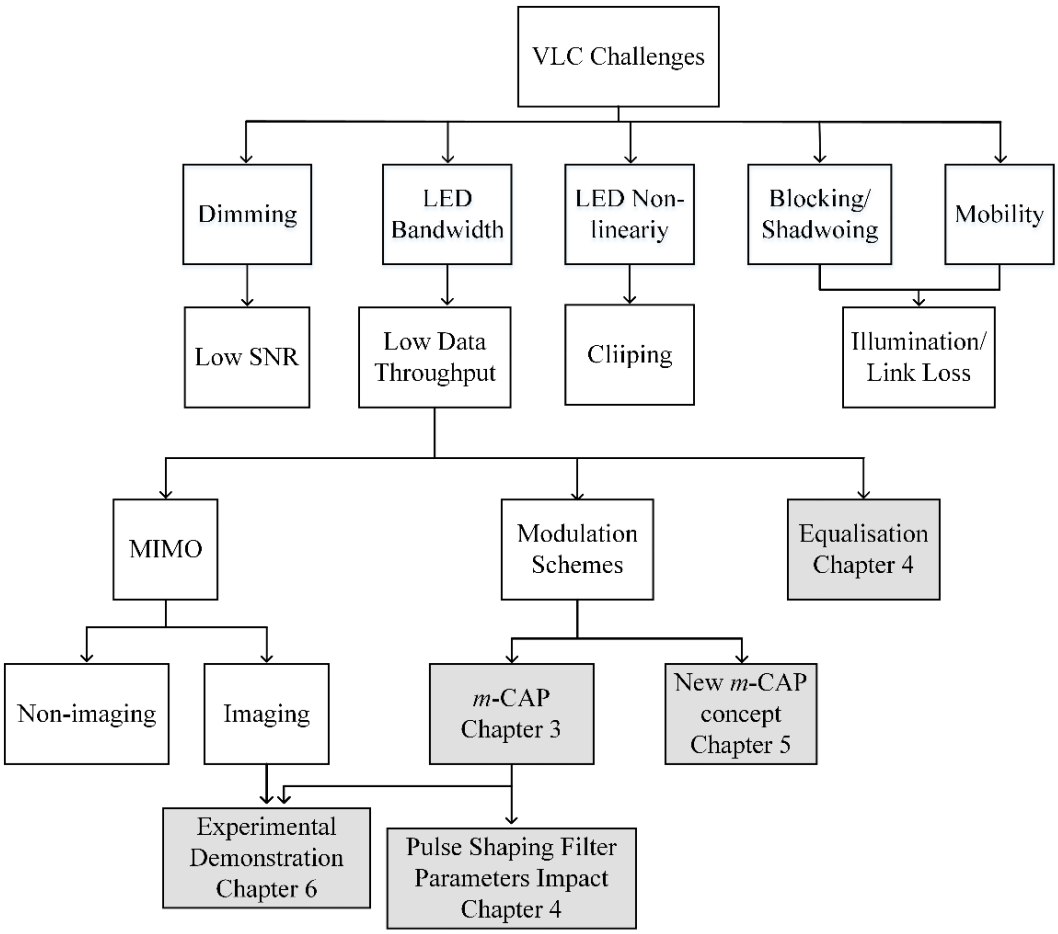

Figure 1.3. VLC challenges and thesis contributions

1.6 List of Publications

1.6.1 Peer Reviewed Journal Papers

1. **K. Werfli**, P. Chvojka, Z. Ghassemlooy, N. B. Hassan, S. Zvanovec, A. Burton, P. A. Haigh, and M. R. Bhatnagar, “Experimental demonstration of high-speed 4 × 4 imaging multi-CAP MIMO visible light communications”, *IEEE-Journal of Lightwave Technology*, vol.36. no 10, PP. 1944-1951, 2018**.** DOI: 10.1109/JLT.2018.2796503
2. P. Chvojka, **K. Werfli**, S. Zvanovec, P. A. Haigh, V. H. Vacek, P. Dvorak, P. Pesek, Z. Ghassemlooy, "On the *m*-CAP performance with different pulse shaping filters parameters for visible light communications," *IEEE-Journal of Photonics Journal*, vol. 9, no. 5, pp. 1-12, 2017. DOI: 10.1109/JPHOT.2017.2749203
3. P. A. Haigh, A. Burton, **K. Werfli**, H. Le Minh, E. Bentley, P. Chvojka, W. O. Popoola, I. Papakonstantinou, and S. Zvanovec, "A multi-CAP visible light communications system with 4.85 b/s/Hz spectral efficiency," *IEEE-Journal of Selected Areas in Communications*, vol. 33, no. 99, pp. 1771-1779, 2015. DOI: 10.1109/JSAC.2015.2433053

1.6.2 Peer Reviewed Conference Papers

1. P. Chvojka, **K. Werfli**, P.A. Haigh, S. Zvanovec, Z. Ghassemlooy, and M. R. Bhatnagar, "Multi-band carrier-less amplitude and phase modulation for VLC: An overview", in *1st South American Colloquim on Visible Light Communications (SACVLC)*, 2017. DOI: 10.1109/SACVLC.2017.8267607

2. P. Chvojka, S. Zvanovec, **K. Werfli**, P. A. Haigh, and Z. Ghassemlooy, "Variable *m*-CAP for bandlimited visible light communications," in *Communications Workshops (ICC Workshops), 2017 IEEE International Conference on*, 2017, pp. 1-5. DOI: 10.1109/ICCW.2017.7962624
3. **K. Werfli**, P. A. Haigh, Z. Ghassemlooy, N. B. Hassan, and S. Zvanovec, "A new concept of multi-band carrier-less amplitude and phase modulation for bandlimited visible light communications," in *2016 10th International Symposium on Communication Systems, Networks and Digital Signal Processing (CSNDSP)*, 2016, pp. 1-5. DOI: 10.1109/CSNDSP.2016.7573916
4. **K. Werfli**, P. A. Haigh, Z. Ghassemlooy, P. Chvojka, S. Zvanovec, S. Rajbhandari, and S. long, "Multi-band carrier-less amplitude and phase modulation with decision feedback equalization for bandlimited VLC systems," in *Optical Wireless Communications (IWOW), 2015 4th International Workshop*, 2015, pp. 6-10. DOI:10.1109/IWOW.2015.7342255
5. P. A. Haigh, A. Aguado, Z. Ghassemlooy, P. Chvojka**, K. Werfli**, S. Zvanovec, E. Ertunç, and T. Kanesan, "Multi-band carrier-less amplitude and phase modulation for highly bandlimited visible light communications; **Invited paper**," in *Wireless Communications & Signal Processing (WCSP), 2015 International Conference*, 2015, pp. 1-5.DOI:10.1109/WCSP.2015.7341338

Chapter 2 PRINCIPALS OF VLC

2.1 Introduction

Wireless access technologies have continuously evolved in response to the ever-increasing capacity demands resulting from the wide spread use of smart and mobile devices. Current fourth generation wireless systems with a limited frequency spectrum will not be able to allocate sufficient bandwidth to cope with the exponentially growing traffic. Consequently, highly spectrally efficient communication techniques are one of the key considerations in the research towards fifth generation networks [52]. Within this context, VLC systems can be utilised as a complementary wireless technology [53] to RF-based schemes mostly in applications where high bandwidth and low latencies are the main requirements. Cisco projections show that the overall mobile data traffic will increase by almost sixfold between 2015-2019, exceeding 24 EB/month with a compound annual growth rate of 55% [53]. As mentioned in the previous chapter, in contrast to traditional RF-based wireless communications, VLC systems have significant advantages including a very high unregulated bandwidth of ~400 THz, high power efficiency, inherent data security, no RF interference and low-cost. VLC technology has the potential for contributing towards unlocking the spectrum congestion and therefore allowing the RF bandwidth to be used more efficiently and effectively, as the existing RF technology is struggling to deal with the ever-growing data traffic. Moreover, VLC technology offers

multiple functionalities including illumination, data communication, indoor localisation and sensing, and it will be part of future 5G wireless communications to offer cellular systems [54, 55].

The first appearance of a VLC system was at Keio University, Japan in 2000 [56]. It was demonstrated that it is feasible to combine illumination with data communication simultaneously. Since then, through the recent two decades, VLC has received growing research interest; benefiting significantly from the widespread use of LEDs in solid-state lighting systems [14]. VLC can be considered as a complementary technology to RF-based links rather than a replacement. Whereas RF-based links enjoy a great mobility, VLC links excel at high-speed data transmission for short-haul links and allow positioning in indoor environments.

The first step towards publicising the standardisation of VLC was initiated in 2003 as the VLC consortium (VLCC) was established by major Japanese companies [57]. It did not take long for Europe to catch up with the VLC revolution, as the OMEGA project was launched in 2008, which was funded by the EU Frame Program 7 (FP7) demonstrating a VLC link with a high data rate R_b (i.e., Gb/s) for a home access network [57]. As a result of the ever-growing interest in VLC, the last decade has witnessed the adoption of VLC technology in a multitude of different communication applications, such as in hospitals [13], vehicle to infrastructure [58], vehicle to vehicle, intra-vehicle [59, 60], and aircraft cabins in commercial airplanes [61]. In Jun 2011, the IEEE 802.15.7 standard was defined for local and metropolitan area networks: short-range optical wireless communications utilising VLC to define the medium access control and physical layers for VLC systems [62]. This chapter examines the fundamentals of VLC systems. In section 2.2, an illustration of the main structure of VLC systems is provided, the model of a VLC channel is described, and the main source of noise in VLC is defined. In section 2.3, the B_{mod} is defined and discussed. In addition, section 2.4 and it is subsections outline the modulation

schemes for VLC, including baseband pulse shaping modulation, single-carrier modulation, and multi-carrier modulation. Finally, a summary of the chapter is given at the end.

2.2 VLC System Model

As in any typical communications system, a VLC link consists of a transmitter, a propagation channel (i.e., air) and a receiver. Figure 2.1 shows the main elements of a basic VLC link. At the Tx side, the generated bits are first modulated by the "Modulator" prior to the conversion from digital to analogue (D/A). Unlike RF-based communication links, in optical wireless systems such as VLC, the continuous optical signal has to be non-negative. Thus, in the VLC links, the continuous generated data is fed to a driving circuit, which superimposes a direct current (DC) to the continuous signal to ensure that the optical power emitted from the LED is always positive, which is to say that:

$$x(t) \geq 0, \tag{2.1}$$

where $x(t)$ is the continuous optical signal. With the existence of such a constraint, the average transmit power of the continuous optical signal is given as [63]:

$$P_t \geq \lim_{T\to\infty} \frac{1}{2T} \int_{-T}^{T} x(t)\, dt. \tag{2.2}$$

The non-negative continuous optical signal is then used to intensity-modulate an LED.

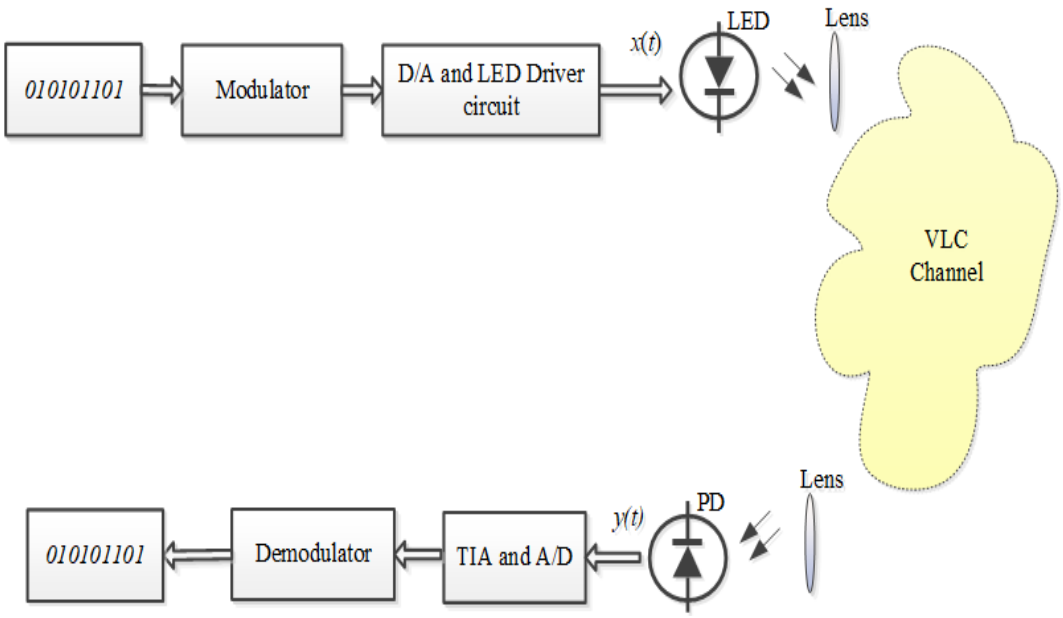

Figure 2.1. Block diagram of a typical basic VLC system

There are two main methods of generating white light using LEDs. The first uses GaN blue emitters with the yellowish cerium-doped yttrium aluminium garnet (Ce:YAG) wavelength-conversion phosphors (commonly known as white phosphor-based LED (WPLED)) [64-67]. However, due to the slow response of phosphor this method offers limited B_{mod} in the range of few MHz (< 5MHz) [35]. The second method relies on mixing three different LEDs (i.e., RGB LEDs) wavelengths [68].

Moreover, each colour of the three LEDs can be modulated separately, and by deploying the three colours, a higher link throughput can be achieved (i.e., the WDM technique). The optical spectra distribution of the RGB LEDs is illustrated in Figure 2.2(a), where the RGB LEDs have peaks at 470 nm (B), 525 nm (G) and ~625 nm (R) [1]. A VLC system with an independently modulated RGB LEDs has been experimentally demonstrated with simultaneous transmission using the WDM scheme [69]. In [70], the reduction of interference among adjacent cells employing RGB LEDs was investigated. It should be noted that, the first method is dominant in the market since it is low cost with no colour balancing requirements. While RGB LEDs can offer circuits to generate white

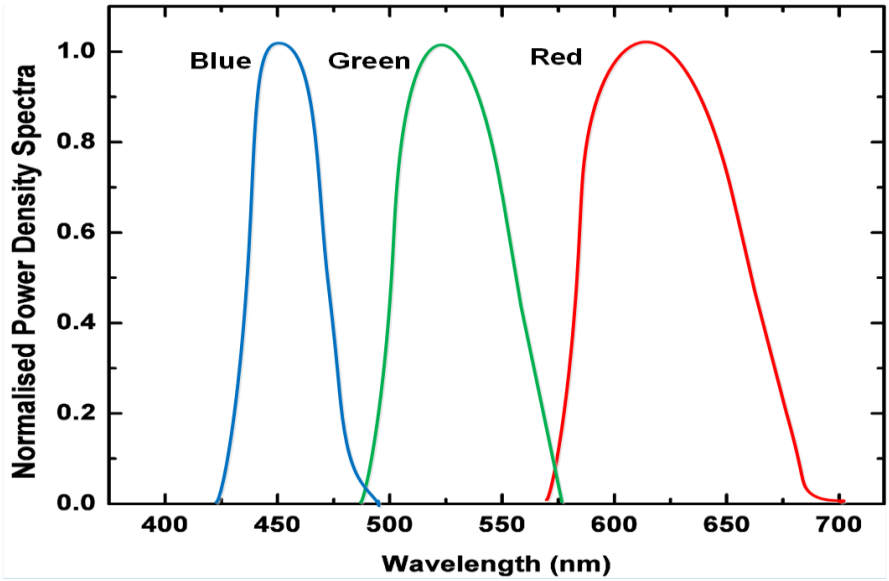

(a)

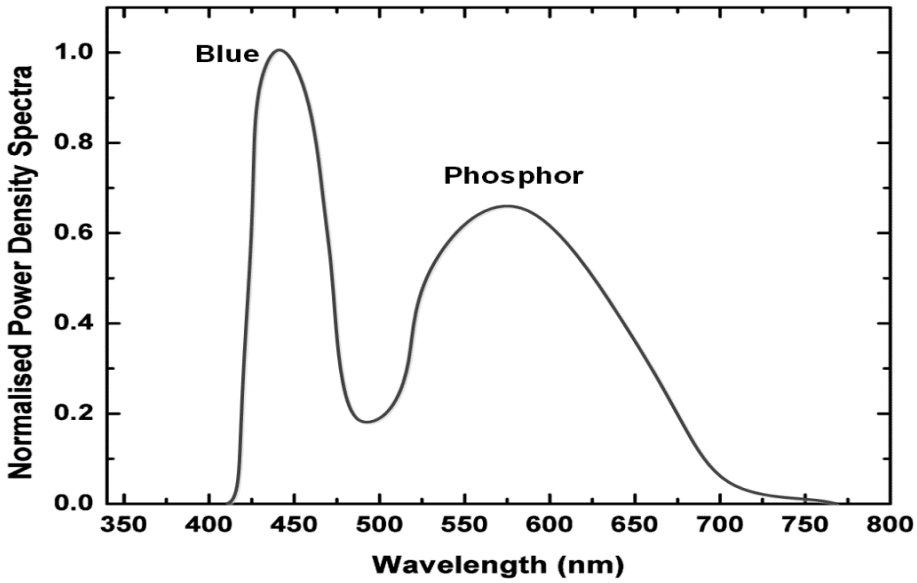

(b)

Figure 2.2. The measured emitted spectra for (a) RGB LEDs (adopted from [71]), and (b) WPLEDs (from [1])

light. In addition, the method also suffers from the difficulty of maintaining colour balancing [1, 12, 72]. The optical spectra emitted by WPLEDs is shown in Figure 2.2(b). WPLEDs have a peak at 445 nm (B), while the phosphor has a wider range of spectral emission peaking at ~555 nm. The output intensity of the optical signal is then focused

using an optical cover lens before it propagates through the VLC channel towards the receiver.

The optical wireless communications channel can be classified into three categories; line-of-sight (LOS), non-directed LOS and diffuse. The LOS links, also known as direct LOS, are typically links in which light emission from an LED directly strikes the PD, i.e., point-to-point. The non-directed LOS links are those in which the emitted light reaches from a wide illumination angle, as the utilised PD has a wide field of view (FOV) and as such, the constraint of point-to-point can be to some extent dismissed. The diffuse path simply characterised links in which the emitted light intensity strikes an object prior to being detected by the PD [1, 16, 73, 74].

At the Rx, an optical lens can be utilised to focus the received light signal onto the PD. The most commonly used PD is the p-i-n diode, which as the name implies, is made of a p-n semiconductor diode with an additional layer of intrinsic semiconductor stuffed between the p-n layers. p-i-n diodes provide improved linearity performance compared to the avalanche photodetector (APD). In addition, p-i-n diodes do not encounter the drawback of the multiplication noise related to the avalanche process in APD [1]. As in the traditional RF-based links, the transmitted signal encounters some types of corruption by deterministic and random distortion as a result of the propagation environment. As an example, wired RF-based links usually encounter distortion by the random thermal noise as well as the shot noise, which are usually frequency selective. These distortions, which are caused by various unwanted factors, are referred to as the response of the communication channel between the Tx and the Rx. The communication channel is usually represented by a mathematical model, which approximates the physical channel. The optical wireless (in this case VLC) channel can be modelled as follows [75-77]:

$$y(t) = \mathcal{R}\, x(t) \otimes h(t) + n(t), \tag{2.3}$$

where $y(t)$ is the received signal, $\otimes$ denotes convolution, $\mathcal{R}$ (A/W) represents the PD's responsivity, $h(t)$ is the channel impulse response, and $n(t)$ is the noise signal, which is modelled as an additive white Gaussian noise (AWGN).

An important figure of merit of a communication system is the signal to noise ratio (SNR), which is expressed as [1, 77]:

$$\text{SNR} = \frac{(\mathcal{R}P_r)^2}{N_o}, \tag{2.4}$$

where P_r (Watt) represents the average received signal power and is given by [77]:

$$P_r = \sum_{d=0}^{\infty} P_{rd}, \tag{2.5}$$

where d is the number of reflections. N_o in Equ. (2.4) represents the total noise variance, which can be expressed as:

$$N_o = \sigma_{shot}^2 + \sigma_{thermal}^2. \tag{2.6}$$

As can be observed from Equ. (2.6), the total noise variance is the sum of the contributions from shot noise σ_{shot}^2 (the ambient induced), which is generated due to the random fluctuations of the generated photons and can be modelled as a signal independent zero mean AWGN [75], and the thermal noise $\sigma_{thermal}^2$, which is generated by the electronic components in the Rx circuit that can also be modelled as a signal independent zero mean AWGN [78].

σ_{shot}^2 is defined in terms of variance as given by [1, 75, 77]:

$$\sigma_{shot}^2 = 2q\mathcal{R}P_r B_{Rx} + 2qI_{bg}B_{Rx}, \tag{2.7}$$

where q is the electronic charge, B_{Rx} is the receiver bandwidth noise, and I_{bg} is the background light induced current. It is worth mentioning that, the major source of the background light induced current is the natural source (i.e., the Sun), as sunlight produces the highest levels of background light induced current and is considered as the main source of shot noise at the Rx (i.e., PD). On the other hand, the background light induced current produced from artificial sources of illumination has a small contribution to the overall background light induced current, as it is typically only few tens of μA, far below that produced by sunlight, which could be as high as 5 mA [1].

$\sigma_{thermal}^2$ is defined in terms of variance as [1, 75, 77]:

$$\sigma_{thermal}^2 = \frac{8\pi k T_k}{G} C_{pu} A I_2 B_{Rx}^2 + \frac{16\pi^2 k T_k \Upsilon}{g_m} C_{pu}^2 A^2 I_3 B_{Rx}^2, \quad (2.8)$$

where k is the Boltzmann's constant, T_k is the absolute temperature, G is the open-loop voltage gain, C_{pu} is the fixed capacitance of PD per unit area, Υ is the field-effect transistor (FET) channel noise factor, g_m is the FET transconductance, and $I_2 = 0.562$, and $I_3 = 0.0868$ are the noise bandwidth factors. A typical value for the thermal noise $\sigma_{thermal}^2$ is 17.5348×10^{-16} A^2 [79]. For a typical indoor environment, the standard illumination level is between 300 - 500 lx at 0.8 m height from the floor level, which is equivalent to a power requirement of > 2.25×10^{-4} W. This represents a shot noise variance of at least ~2×10^{-16} A^2, which is the same as $\sigma_{thermal}^2$ [79].

Following the detection by the PD, where the simplest and easiest way of detection in VLC is the DD scheme, the resulting photo-current signal is then passed through a transimpedance amplifier (TIA), and the regenerated electrical signal is then sampled using an analogue to digital (A/D) converter prior to the final stage where the demodulation process takes place depending on the modulation scheme used. Finally, the original transmitted bits are estimated and recovered.

2.3 LED Modulation Bandwidth

As discussed in the previous chapter, the key impediment towards achieving high capacity VLC-based links is the limited B_{mod} caused by the LED. Moreover, as stated in the previous section, the simplest and most commercially available method to generate white light from an LED is to use WPLED, which has a raw B_{mod} limited to a few MHz (typically < 5 MHz), and thus, in effect, behaves as a first-order low-pass filter (LPF) with a 20 dB/decade. In contrast, the RGB LEDs offer a higher B_{mod} in the range of tens of MHz. However, their use implies an additional complexity for the system in order to maintain the portions of white colour balanced. On the other hand, micro-LEDs offer a higher B_{mod} (B_{mod} > 20 MHz [31]). However, they are not suitable for illumination applications. Thus, it is crucial to know the cause of such a phenomenon (i.e., limited B_{mod}) before investigating any solutions. The bandwidth of a channel is an important figure of merit. In VLC, the bandwidth of the channel is huge ~400 THz. However, the issue lies in the limited B_{mod} introduced by the LED. There are a few definitions of

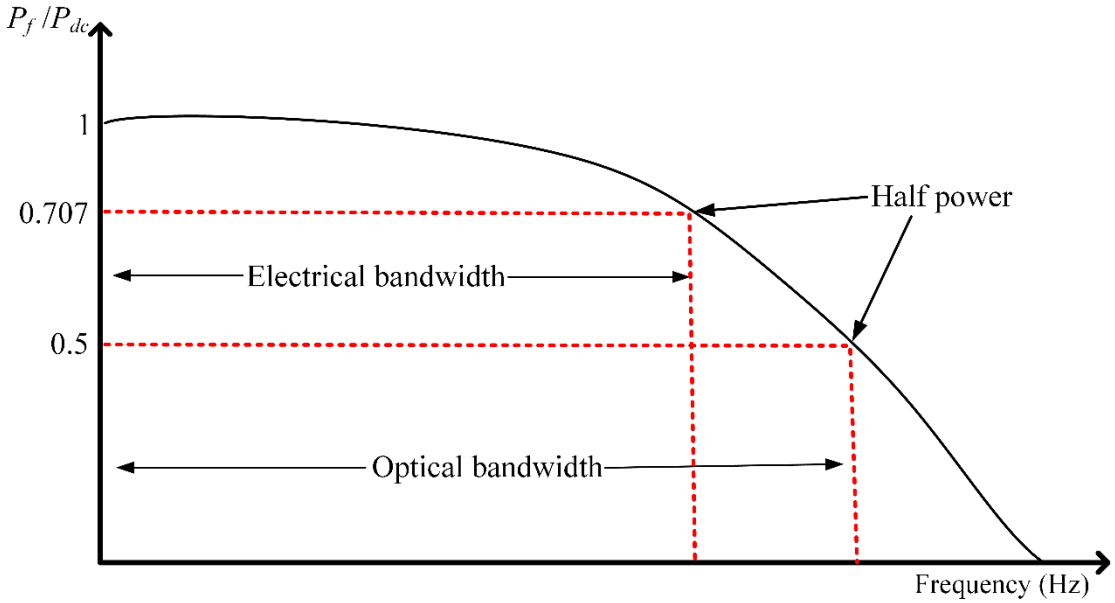

Figure 2.3. Electrical and optical B_{mod}. It should be noted that the half power point occurs at 70.7% and 50% of the original input signal peak value for the electrical domain and optical domain, respectively, from [1].

bandwidth, the most obvious one is the amount of difference in frequency (Hz) between two signal frequency components, i.e., the highest and the lowest. Another definition, which is going to be adopted in this thesis is the absolute bandwidth, which is the range of frequencies where the signal has a non-zero power spectral density (PSD). In VLC systems, the most common definition of the bandwidth, which will be adopted in this thesis to refer to LED B_{mod} (first order LPF), is the half power bandwidth (see Figure 2.3), commonly known as -3 dB bandwidth. It is defined as the frequency where the input signal is attenuated by 70.7% of its original peak value in the electrical domain, and by 50% of its original peak value in the optical domain [1, 80]. This is attributed to the fact that in the electrical domain, the signal power is proportional to the square of the current ($P = I_c^2 R$), where I_c represents the current and R is the resistor. On the other hand, in the optical domain, the signal power is proportional to the photo current I_p (i.e., $P \alpha I_p$). Thus, the signal power is represented in the logarithmic base (dB) for both electrical and optical cases, respectively as:

$$\text{Half power} = 20\, Log_{10}\,(I_c). \tag{2.9}$$

$$\text{Half power} = 10\, Log_{10}\,(I_p). \tag{2.10}$$

There are three main parameters that affect B_{mod} and the frequency response of an LED. These three parameters are (*i*) the parasitic capacitance; (*ii*) the junction capacitance; and (*iii*) the amount of the injected current for an LED, as the LED is essentially a diode operating in forward bias, which produces an optical intensity approximately linearly related to the amount of the pumped drive current. In [1], it was stated that the capacitance values are almost fixed. However, the LED frequency response can be increased by increasing the amount of the pumped current. This can be achieved by superimposing an appropriate constant DC bias to the continuous signal. However, this process is constrained by the fact that the swing of the transmitted signal must be kept within the

linear region of the LED (dynamic range) in order to avoid signal clipping. Thus, the injected current must be chosen appropriately to avoid the aforementioned issue. The relative optical power produced by doing so can be expressed as [1]:

$$\frac{P_f}{P_{dc}} = \frac{1}{\sqrt{1 + (f\zeta)^2}}, \tag{2.11}$$

where P_f is the power of the continues signal at a given frequency f, P_{dc} is the DC power, and ζ is the minority carrier lifetime, which is given as [1]:

$$\frac{1}{\zeta} = \frac{1}{\zeta_R} + \frac{1}{\zeta_{NR}}, \tag{2.12}$$

where ζ_R and ζ_{NR} are the radiative and non-radiative components of ζ. The -3 dB value is achieved when Equ. (2.11) is set to 0.707 for the electrical domain and to 0.5 for the optical domain, see Figure 2.3. As it can be observed from (2.11), increasing the raw B_{mod} of an LED can be achieved by reducing ζ by as much as ζ_R can be reduced. This is realised by increasing the doping levels. However, very high doping levels, lead to a reduction of ζ_{NR}, which severely diminish the quantum efficiency of an LED [1].

2.4 **Modulation Schemes**

As previously explained in section 2.2, VLC links employ the IM/DD technique, i.e., the intensity level varies according to the input modulating signal, and the PD directly detects the difference in the light intensity level. Moreover, unlike RF-based links, in VLC links the transmitted signal cannot be encoded by the amplitude or phase of the LED light. Instead, the intensity of the LED light is varied, which implies that the transmitted signal has to be non-negative, which is a constraint of optical wireless communications. In addition, one can refer to the VLC links' IM/DD procedure as having two modulation stages. The first modulation stage is implemented by varying the carrier signal's

characteristics in order to modulate the data signal (e.g., the quadrature amplitude modulation (QAM) scheme). In a wide sense, the digital modulation scheme is referred to as line-code modulation schemes, which reflects that the data signal is pre-coded in order to spectrally shape it prior to the transmission. The second modulation stage in VLC links is, as mentioned earlier in this section, implemented by varying the intensity of LED light according to the modulated signal.

A modulation scheme is judged by main three factors of (*i*) the bandwidth efficiency η_s, which is defined as the ratio between the achievable R_b over bandwidth B; i.e. $\frac{R_b}{B}$ bits/second/Hz (b/s/Hz): (*ii*) the power efficiency, i.e., the average electrical power required at the receiver Rx in order to satisfy a specific BER; and (*iii*) reliability, which includes the ability to mitigate ISI, offering a demodulation at the Rx with an acceptable BER performance, low complexity and cost of implementation [63].

In this section, the focus will be on introducing the most common modulation schemes used in VLC links in order to increase the transmission speed and overcome the issue of ISI. Moreover, a brief explanation of single-carrier modulation schemes will be provided including the most commonly used modulation scheme, known as OOK, pulse position modulation (PPM), multi-level modulation schemes such as pulse amplitude modulation (PAM), QAM, and CAP. Finally, multi-carrier modulation schemes will be discussed, focusing on the most famous multi-carrier scheme, which is OFDM.

2.4.1 **Single-carrier modulation**

2.4.1.1 **On-off keying (OOK)**

OOK is considered as one of the pulse shaping modulation schemes where data is sent by a series of pulses that display a change of the pulse characteristics, which could be either level of amplitude, position or width. The principle of OOK scheme is very simple as it is achieved by simply changing the level of intensity of a pulse (i.e., symbol duration T_b) from high to low or from low to high, where at the high intensity level, the bit '1' is transmitted and at the low intensity level, the bit '0' is transmitted. Therefore, the OOK scheme is referred to as a binary modulation scheme. It should be noted that, the LED is not completely off when sending the bit '0', it is only the level of light intensity that diminishes [81].

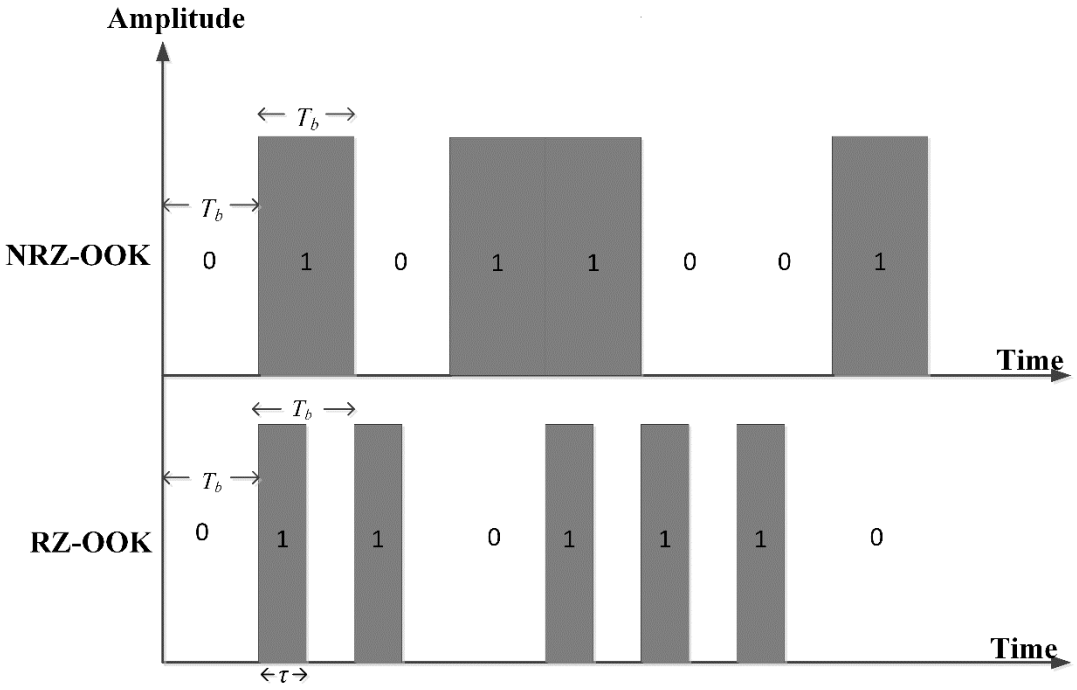

Figure 2.4. An example signal for NRZ-OOK and RZ-OOK. It should be noted that the duty cycle τ of the RZ-OOK is 0.5 and T_b is the symbol duration

There are two types of OOK scheme, (*i*) non-return to zero OOK (OOK-NRZ); and (*ii*) return to zero OOK (OOK-RZ), as shown in Figure 2.4. The main difference is that OOK-RZ has a shorter T_b (i.e., duty cycle) than OOK-NRZ when representing the bit '1' (see Figure 2.4). Thus, OOK-RZ is more power efficient than OOK-NRZ. However, OOK-NRZ has a better bandwidth efficiency, which is a key figure of merit in any modulation scheme. The OOK-NRZ signal bandwidth is $1/T_b$, whereas, in OOK-RZ, the signal bandwidth is $1/\tau T_b$, where τ represents the duty cycle. OOK has huge popularity in VLC links due to its ease of use and simplicity of implementation. In [82], implementing OOK-NRZ R_b of 40 Mb/s was achieved in conjunction with the blue filtering technique. The downside of the OOK scheme is that it has a relatively low R_b and low spectral efficiency (η_s) in contrast with the other more sophisticated modulation schemes such as OFDM.

2.4.1.2 **Pulse position modulation (PPM)**

PPM is another pulse shaping modulation scheme that is based on the position of the pulse. More specifically, T_b is divided into many equal chips (as shown in Figure 2.5 for 4-PPM), and the pulse is transmitted by setting one of the chips to a high-intensity level, while the other chips remain at low level. PPM has improved power efficiency compared

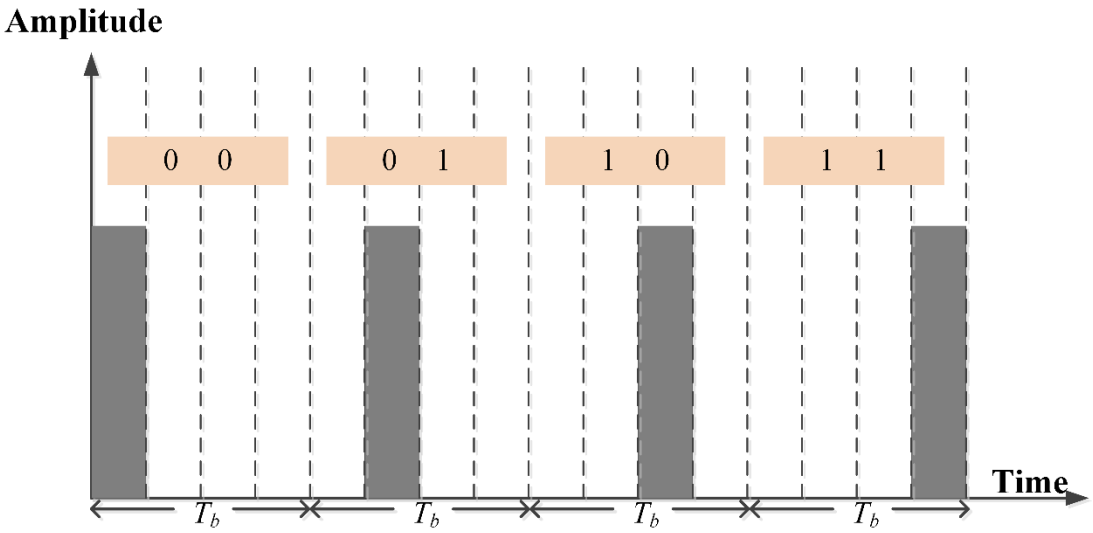

Figure 2.5. 4-PPM waveform

to OOK. However, the price to pay here is scarifying the bandwidth efficiency. For instance, 4-PPM has η_s of $\frac{1}{M}\log_2 M$ b/s/Hz, where M represents the PPM cardinality. As it can be observed from Figure 2.5, 4-PPM requires three times less power than NRZ-OOK. However, this implies less η_s. This is why M-PPM is used in such applications where the power budget is crucial and the bandwidth efficiency is not a critical concern [81]. Another version of the PPM scheme, known as overlapping PPM (OPPM), was proposed in [83]. As the name implies, the difference between OPPM and PPM is that in OPPM the next transmitted chip is sent straight after the first transmitted chip by deleting the low intensity of the other chips, resulting in overlapping transmitted patterns.

2.4.1.3 **Pulse amplitude modulation (PAM)**

Due to the drawback of OOK and PPM and its variants, which is represented in having low η_s (e.g., only one chip is sent per T_b in PPM), other modulation schemes have been proposed over time, including PAM, which is a multi-level modulation scheme that transmits the signal in a multi-level (M-ary) unipolar M-PAM by varying the intensity

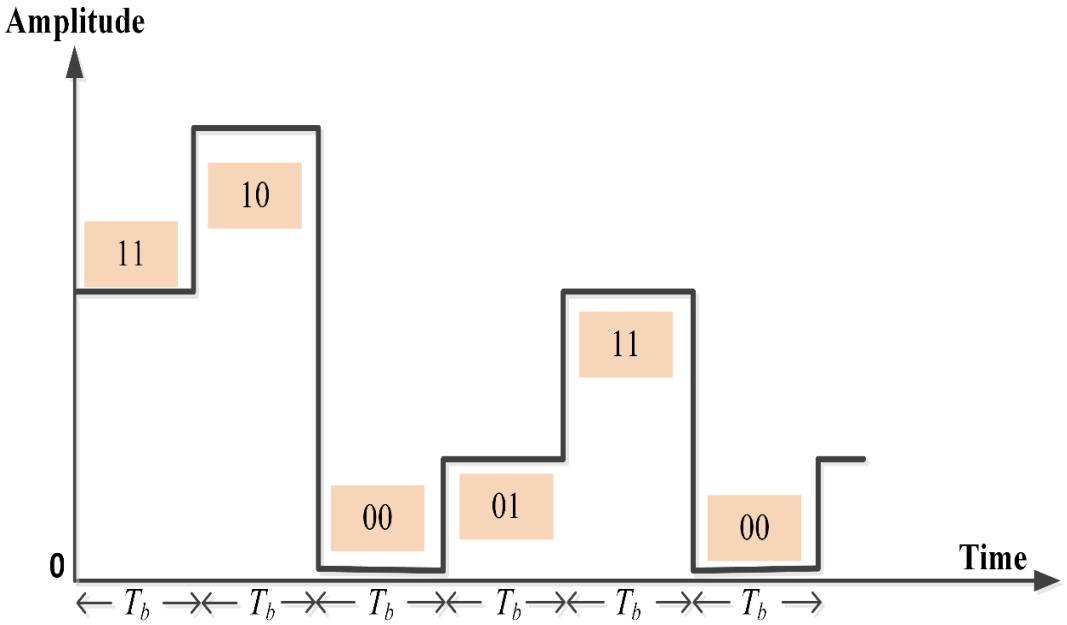

Figure 2.6. An example of a 4-PAM waveform

levels, as shown in Figure 2.6 (4-PAM). In contrast to OOK and PPM, PAM offers higher η_s that is proportional to $\log_2(M)$ b/s/Hz. However, this is achieved at the cost of less power efficiency [1]. Due to its relatively high η_s compared with the aforementioned schemes, PAM has been investigated in VLC-based systems in order to increase the achieved R_b [84, 85].

2.4.1.4 **Pulse width modulation (PWM)**

PWM is a popular and an efficient modulation scheme among the applications that require achieving dimming and data transmissions simultaneously. As the name implies, in PWM, the width of the pulse is varied according to the required dimming level, and at the same time, the modulated information bit is sent during the pulse duration when the PWM frequency is high enough. PWM with different dimming levels of 25%, 50%, and 75% is illustrated in Figure 2.7. Different dimming control levels starting from 0% to 100% can be achieved by implementing high-frequency PWM [81]. The downside of PWM is that it offers a very low R_b, e.g., 4.8 kb/s in [86]. In order to achieve good data transmission while maintaining the ability of dimming, many proposals have been suggested to

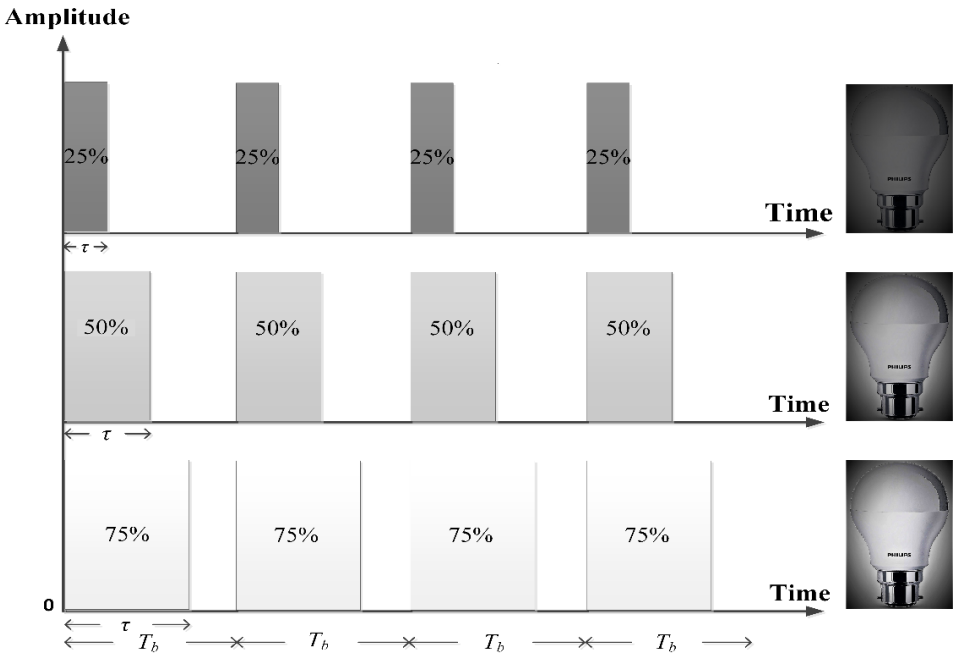

Figure 2.7. An example of a PWM signal for different dimming levels of 25%, 50% and 75%

overcome such an issue [87-89], including superimposing NRZ-OOK on the PWM, implementing discrete multi-tone (DMT) and/or hybrid PWM with PPM. However, synchronisation is a major concern in the aforementioned schemes.

2.4.1.5 **Quadrature amplitude modulation (QAM)**

QAM is an *M*-ary modulation scheme that consists of a combination of two independent schemes. The first is the amplitude shift keying (ASK) scheme, which is implemented by varying the sinusoidal carrier wave to level +1 to represent the bit '1' and to level -1 to represent the bit '0'. The second scheme is the phase shift keying (PSK) scheme, where the phase of the sinusoidal carrier wave is varied according to the information bits. In other words, the sinusoidal carrier uses one phase to represent the bit '1' and a different phase to represent the bit '0'. Moreover, in QAM the information bits are modulated in amplitude by two orthogonal independent sinusoidal carrier waves, i.e., they are 90° out of phase (cosine (in-phase *I*) and sine (imaginary *Q*)) with the same carrier frequency, which results in a higher data throughput. Figure 2.9(a) shows the basic block diagram of a QAM modulation scheme where x_1 and x_2 are the real and imaginary parts of the

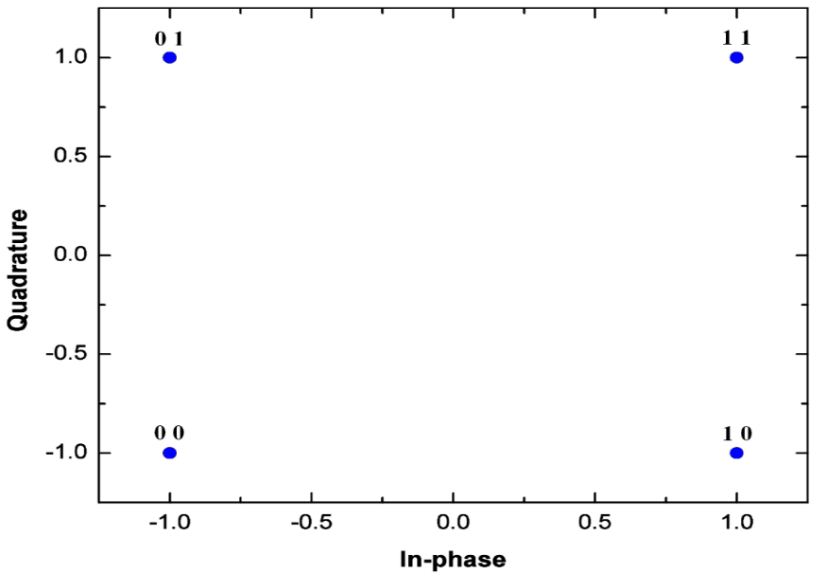

Figure 2.8. 4-QAM signal constellation. The bits are mapped using the Gray mapping coding technique and x-axis is normalised.

baseband signal respectively, and $q(t)$ is the low pass filter impulse response and $x(t)$ is the ready-for-transmission signal. The combination of the two schemes provides a signal space where various constellation points (information) represent special signal values, i.e., a constellation diagram [90]. As an example, the constellation diagram of 4-QAM and the distribution of the bits using the Gray mapping code is shown in Figure 2.8. The number of bits per symbol $b = \log_2 M$, where M is the QAM cardinality. For instance, for $b = 4$, the QAM order $M = 16$ (i.e., 16-QAM).

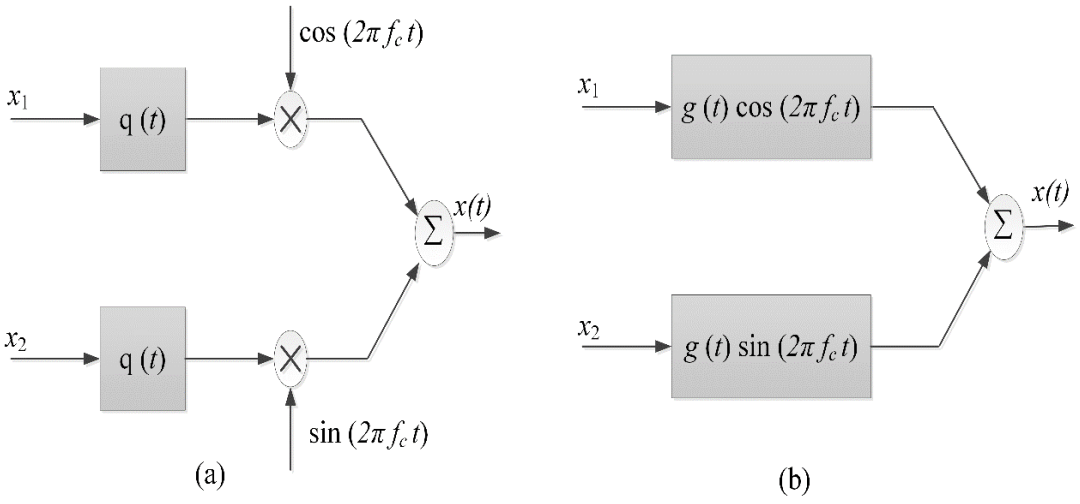

Figure 2.9. Block diagram of the: (a) QAM, and (b) CAP schemes

2.4.1.6 **Carrier-less amplitude and phase (CAP) modulation**

CAP modulation is a single-carrier multi-level modulation scheme, which was first implemented in the mid-1970s by Falconer *et. al.* at Bell Labs [91]. In addition, CAP is a signal space diversity (SSD) and a multi-dimensional modulation scheme [92]. The CAP scheme has similarity to QAM, in that the data is transmitted in the form of two orthogonal components (i.e., Hilbert transform, *I* and *Q* differ by 90° in phase), which is sometimes known as channel interleaving. However, in contrast to QAM, CAP does not rely on using sinusoidal carriers (i.e., oscillators). Instead, it relies on adopting finite impulse response (FIR) filters with orthogonal waveforms. Thus, the name "carrier-less"

is adopted as it indicates that there is no need to implement any oscillator to create the signals at the Tx or to reconstruct the signals at the Rx [92, 93]. In contrast to OFDM and single-carrier modulation schemes such as QAM, CAP modulation has several advantages, as it does not require complex signal processing such as an inverse fast Fourier transform (IFFT) and fast Fourier transform (FFT), and it only utilises two pulse shaping FIR filters (*I* and *Q*) by means of time domain convolution to create the signal for transmission. Following the same concept, two additional *I* and *Q* pulse shaping FIR filters are used at the Rx in order to reconstruct the transmitted signal, thus avoiding the use of a highly sensitive and coherent local oscillator at the Tx or the Rx. Figure 2.9(b) illustrates the basic block diagram of a CAP modulation scheme. x_1 and x_2 represent the real and imaginary parts of the baseband signal respectively, $g(t)$ is the impulse response of the pulse shaping FIR filters, and $x(t)$ represents the ready-for-transmission signal. A full explanation of the generation of the CAP signal will be provided in Chapter 3.

CAP modulation has gained significant attention within the optical communication research community in recent years (e.g., [45, 92, 94-96]). Furthermore, the CAP modulation scheme was shown to outperform OFDM in terms of R_b over the same physical transmission link, as CAP achieved a higher R_b of 3.22 Gb/s in contrast to OFDM which achieved 2.93 Gb/s, where RGB LEDs were utilised and a BER below 10^{-3} was maintained over a transmission distance of 25 cm [47]. Moreover, a CAP-VLC system employing RGB LEDs and a hybrid post-equalizer was reported in [69] with an achieved R_b of 3.22 Gb/s and for a link distance of over 25 cm. Overall, CAP systems based on IM/DD have been shown to be less complex with improved performance, which allows relatively higher R_b values using optical and electrical components with limited bandwidths [92, 94].

2.4.2 **Multi-carrier modulation**

2.4.2.1 **Orthogonal frequency division multiplexing (OFDM)**

As discussed in the previous subsections, single-carrier modulation schemes suffer from not being able to achieve a high η_s, in addition to the presence of ISI introduced from the frequency selective process in the dispersive wireless optical communications channel. As a result, the attention of the research community has been recently drawn to multi-carrier modulation schemes, which offer better η_s and are more robust to multi-path induced ISI, but are less power efficient. OFDM is a special class of frequency division multiplexing (FDM) in that the sub-carriers are allowed to overlap in frequency as they are orthogonal to each other (i.e., have a harmonic relationship). Moreover, OFDM is the most commonly implemented multi-carrier modulation scheme in VLC links [44] that sends parallel streams of data utilising orthogonal sub-carriers (i.e., spectrally spaced). Unlike single-carrier modulation schemes, in OFDM the number of bits per symbol in each sub-carrier can be boosted in accordance with its channel dispersion by implementing the bit and power loading techniques [48]. Furthermore, the phenomena of inter-carrier interference (ICI) and ISI can be eliminated by inserting a guard interval known as a cyclic prefix (CP) [44].

The OFDM signal is realised by utilising IFFT, followed by D/A converter at the Tx. At the Rx, an FFT is utilised after the A/D converter allowing the simplest equalisation (i.e., zero forcing (ZF) [44]) to be implemented at the Rx. By its nature, the transmitted time domain OFDM signal after the IFFT is complex and bipolar (negative) and in order to implement it in an IM/DD system such as VLC, the constraint of having a real-positive signal in order to intensity-modulate the LED must be met [44]. There are three main schemes to realise real-positive optical OFDM (O-OFDM) signal. The first scheme is known as a direct current optical OFDM (DCO-OFDM), which is implemented by

superimposing the OFDM signal over a positive DC bias in order to achieve a unipolar OFDM signal (satisfying the constraint of IM). Figure 2.10 demonstrates a basic schematic block diagram of the DCO-OFDM. At first, the transmitted bits "Data" are mapped into a QAM format X_{QAM} "QAM-Mapper" followed by a serial to parallel conversion (S/P) in order to arrange the bits into blocks. The blocks of data X_k are then passed through IFFT to form the time domain OFDM signal X_n, which is mapped in a Hermitian symmetric manner. X_n blocks are then converted from parallel to serial (P/S) before a guard band is added to each X'_n block by inserting a copy of the end of each block to the beginning of it (which is commonly known as CP [44]), before it is passed through a D/A convertor. The DC bias is then added to $X(t)$ to make it unipolar and the output of the dynamic range signal amplitude is clipped prior to intensity-modulating the LED.

At the Rx, the light is captured using a PD, which converts the optical signal to an electrical signal. The received signal $Y(t)$ is then passed to an analogue to digital A/D converter and the added CP is removed. S/P conversion is then utilised prior to passing the signal X'_r into the FFT block in order to implement the frequency domain equalisation on the X_r signal by the means of a zero forcing "one-tap" equaliser. P/S conversion is then applied to the X_r signal and finally the data is de-mapped X'_{QAM} (QAM "de-mapper") and the estimated version of the transmitted data is recovered (Data').

The drawback of DCO-OFM is that it suffers from a low power efficiency as the electrical power consumption increases [97]. A more power efficient method known as asymmetrically clipped optical OFDM (ACO-OFDM) is the second common method to achieve an O-OFDM signal. In this type, the Hermitian symmetry is enforced to all sub-carriers and the information is loaded only to the odd sub-carriers while the even sub-carriers are left empty, or in other words, clipped, which implies that the η_s is halved (low

η_s) [98]. The third type of O-OFDM is the pulse amplitude modulated discrete multi-tone (PAM-DMT), which is similar to ACO-OFDM as in this scheme the real part of the signal is clipped to zero. However, because the real part is symmetric to the imaginary, all the sub-carriers are used to send information and the data at the Rx can be recovered. Moreover, all sub-carriers are used to send information, which allows a full use of the bit and power loading techniques [99].

In general, the use of O-OFDM offers improved spectral usage when compared with the single-carrier modulation schemes. Transmission speeds > 5.6 Gb/s have been reported using O-OFDM with WDM, which also made use of the bit and power loading techniques [46, 47]. One disadvantage of OFDM is the high PAPR, as the LEDs employed in VLC often exhibit non-linear electro-optic conversion (I-L) characteristics beyond a certain drive current level [20]. This leads to clipping of the modulating signal, thus resulting in degradation in the BER performance. As a solution, many techniques were propsed in the literature to overcome the high PAPR including implementing trellis coding, adding pilot symbols and most recently a single-carrier frequency domain equalisation (SC-FDE) scheme was proposed in [100], where the main difference from O-OFDM is that the IFFT is moved from the Tx to the Rx, thus resulting in the generation of simpler waveforms with lower PAPR [100].

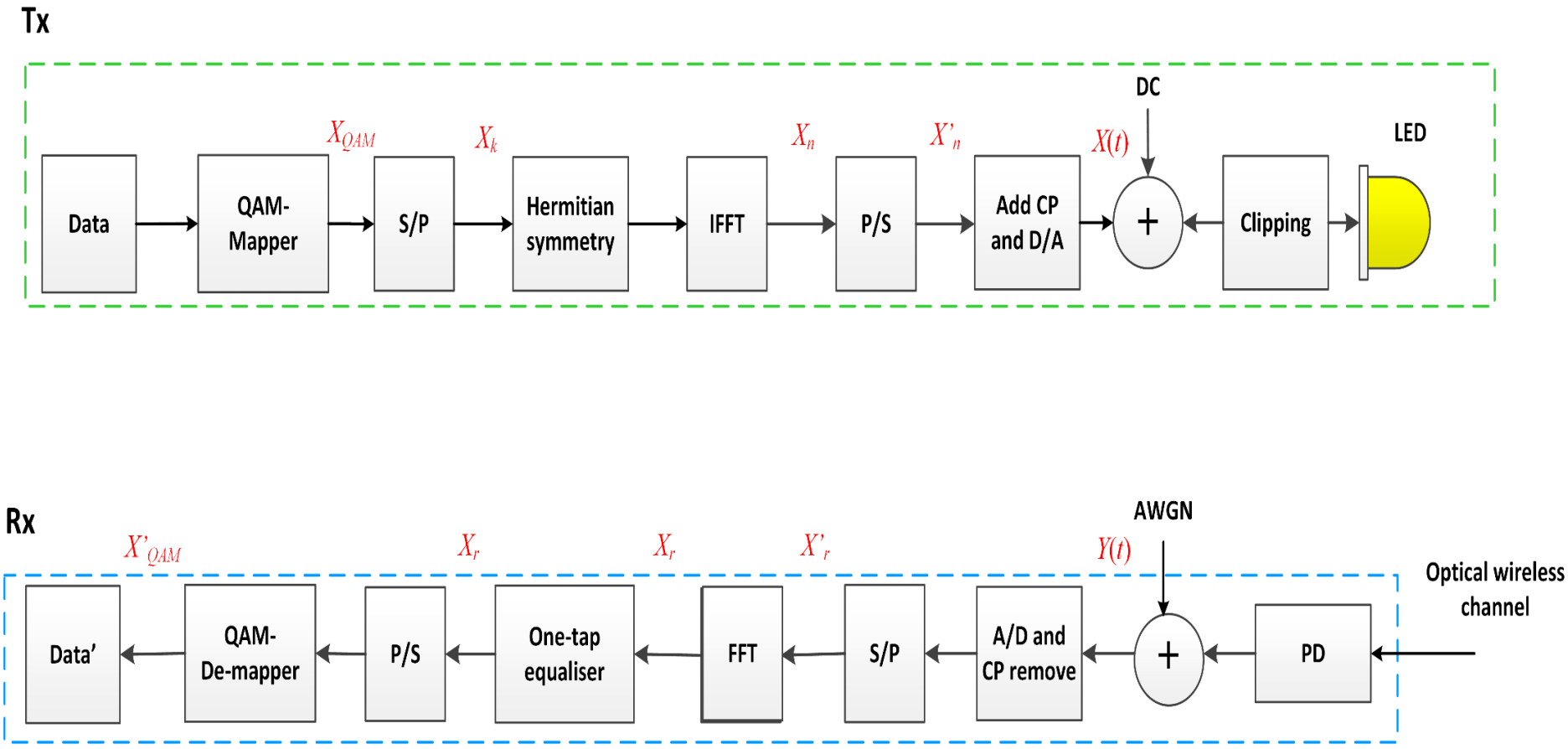

Figure 2.10. Schematic block diagram of DCO-OFDM

2.5 **Summary**

In this chapter, the fundamentals of a VLC system in terms of the Tx structure, the categories of the channel model (which are LOS, non-directed LOS, and diffuse LOS) and the Rx structure have been outlined. Moreover, the main source of noise in a VLC link has been introduced. It was shown that there are two main methods in order to generate white light out of an LED. These two methods are WPLEDs and RGB LEDs. Implementing the commercially available WPLEDs offer limited B_{mod}. In contrast, implementing the RGB LEDs offers more B_{mod}, at the expense of adding complexity to the VLC system. The definition of and the possible solutions to the B_{mod} limitation was also discussed. In addition, the most famous pulse shaping, single-carrier, and multi-carrier modulation schemes used in VLC links such as OOK, PPM, PAM, PWM, QAM, CAP, and OFDM, which were implemented in order to increase the transmission speed and overcome ISI, were briefly discussed in this chapter.

Chapter 3 MULTI-BAND CAP FOR BAND-LIMITED VLC

3.1 Introduction

This chapter aims to discuss and demonstrate the proof of concept of the new CAP scheme known as *m*-CAP. As discussed earlier in Section 1.2 of Chapter 1, the bottleneck problem in VLC systems is caused by the limited B_{mod} of up to a few MHz, which is mainly introduced by commercial LEDs. Thus, various solutions have been proposed in the research community such as using optical filters to filter out the slow yellowish components and pass the blue light, applying pre-equalisation and post-equalisation at the Tx or/and the Rx sides, respectively or combinations of multiple schemes and propositions [15, 35, 41, 43].

Recently, applying complex modulation schemes has emerged as an alternative solution for VLC systems aiming to achieve higher data transmission speeds with less added complexity relative to the existing solutions. OFDM is the most popular sub-carrier modulation format, which has attracted significant attention due to its efficiency of bandwidth use and the ability to support high order modulation schemes by utilising the bit and power loading techniques [44]. In this chapter, another multi-carrier modulation scheme is introduced, known as *m*-CAP. This scheme has several advantages such as relaxing the requirement of implementing a frequency selective channel, as having a flat

fading channel is a phenomenon that seldomely exists in any VLC system. In addition, the scheme also supports the capability of using the bit and power loading techniques [96]. The *m*-CAP scheme is introduced to a VLC system throughout this chapter, and it is practically demonstrated for the first time over a VLC link span of 1 m.

3.2 Principles and Motivations of *m*-CAP

As discussed earlier in Chapter 2, CAP is a single-carrier, multilevel and multidimensional modulation scheme. CAP is similar to QAM, in that the data is transmitted in the form of two orthogonal waveforms, which are referred to as *I* and *Q* components. However, CAP does not require the utilisation of oscillators, as it instead uses pulse shaping filters to generate the two signals and realise the time-domain orthogonality by designing the filters as a Hilbert pair. Moreover, unlike in QAM where the modulation of a baseband signal requires the use of the carrier waves (oscillators), in CAP, the impulse response of the FIR pulse shaping filters is made to form the Hilbert pairs by utilising orthogonal waveforms so that the carrier waveforms are part of the transmitted pulse. Thus, the phrase "carrier-less" was adopted. In order to reconstruct the transmitted signal, time reverse filters (matched filters) are utilised at the Rx, making it an easy scheme to implement. This made CAP a popular modulation scheme for digital subscriber lines (DSLs) in the 1990s [101]. However, CAP requires a high gain and high frequency response channel [45]; making it very sensitive to flat frequency channels, thus losing its position in a favor of DMT in 1999, which was adopted by the international telecommunications union (ITU) as its multi-carrier scheme due to its higher throughput gained by implementing the bit and power loading techniques [102].

Furthermore, the major impediment in the implementation of CAP for VLC systems is that it is very sensitive to high-frequency attenuation present in frequency selective

channels or a non-flat fading channels [45], which is prevalent in VLC systems due to the LED frequency response, which is modelled as a first order LPF. The concept of the frequency selective channel is shown in Figure 3.1(a), which is only valid for VLC systems where the signal frequency components experience different frequency responses as a result of the signal bandwidth B_{sig} being greater than the channel bandwidth B_{ch}. This phenomenon exists in VLC due to the LED bandwidth limitations, which causes an LPF behaviour with 20 dB/decade attenuation outside the -3 dB shoulder that degrades both R_b and the BER. In contrast, the concept of having a flat fading channel is illustrated in Figure 3.1(b). As it can be observed from Figure 3.1(b), the frequency signal components experience the same frequency response as B_{ch} is greater than B_{sig}.

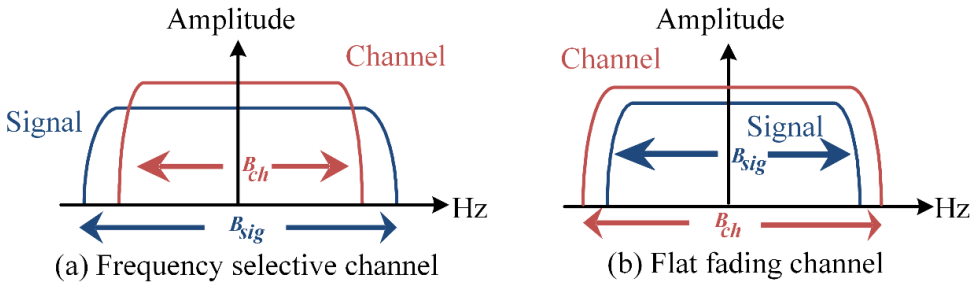

Figure 3.1. An illustration of (a) frequency selective channel, and (b) flat fading channel

CAP is also popular in the field of short-range optical interconnects [96, 103, 104]. Similar to VLCs, lasers used in the transmitter pose a bandwidth limitation, albeit in the order of GHz. In [96], it was found that the attenuation of the high frequencies by the laser frequency response caused a large perturbation to the signal, thus increasing the BER. Therefore, it was proposed to divide the CAP signal into non-orthogonal frequency-division multiplexed sub-carriers, or the so-called *m*-CAP. The *m*-CAP format proposes that the frequency attenuation over small sub-bands will be less than that over the entire bandwidth, and hence a lower error rate can be achieved. Figure 3.2 illustrates the concept of *m*-CAP when B_{sig} = 1 Hz. Moreover, the figure shows different *m*-CAP orders of *m* =

{1, 2, 4, 8, 10} when utilising β = 0.2, where β is the roll-off factor. It should be noted that a large β implies that there will be a (1+ β) greater bandwidth requirement, as given in [105].

Furthermore, the total signal bandwidth B_{tot} is given as $B_{tot} = B_{sig}(1 + \beta)$, which implies that increasing β means a (1 + β) larger bandwidth requirement. From Figure 3.2, it can be observed that by increasing *m*, the value of each sub-carrier bandwidth is decreased as B_{sig} is divided equally between the individual sub-carriers, thus contributing towards relaxing the flat fading channel requirement, which rarely exists in VLC systems because of the high-frequency attenuation caused by the LEDs' LPF behaviour. In other words, by reducing the sub-carriers bandwidth, less attenuation per sub-carrier is achieved in contrast to using high bandwidth sub-carriers, thus offering improvement in the BER performance as well as achieving higher SNR per-sub-carrier and allowing the use of the bit and power loading techniques due to the presence of *m* sub-carriers, which will in turn boost the data throughput.

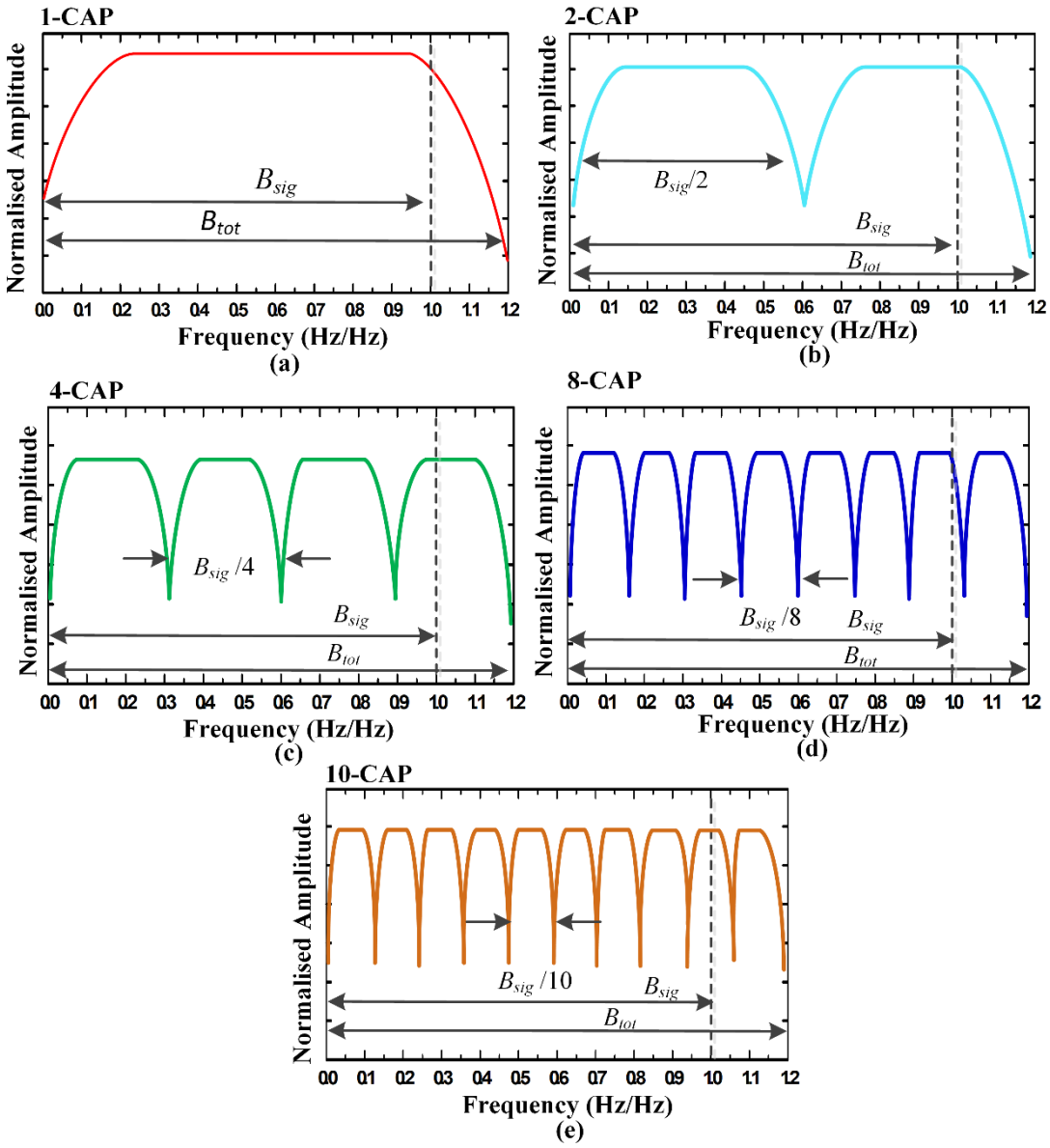

Figure 3.2. An illustration of the *m*-CAP concept in terms of the frequency response for different values of *m:* (a) $m = 1$, (b) $m = 2$, (c) $m = 4$, (d) $m = 8$, and (e) $m = 10$

3.3 *m*-CAP VLC System Model

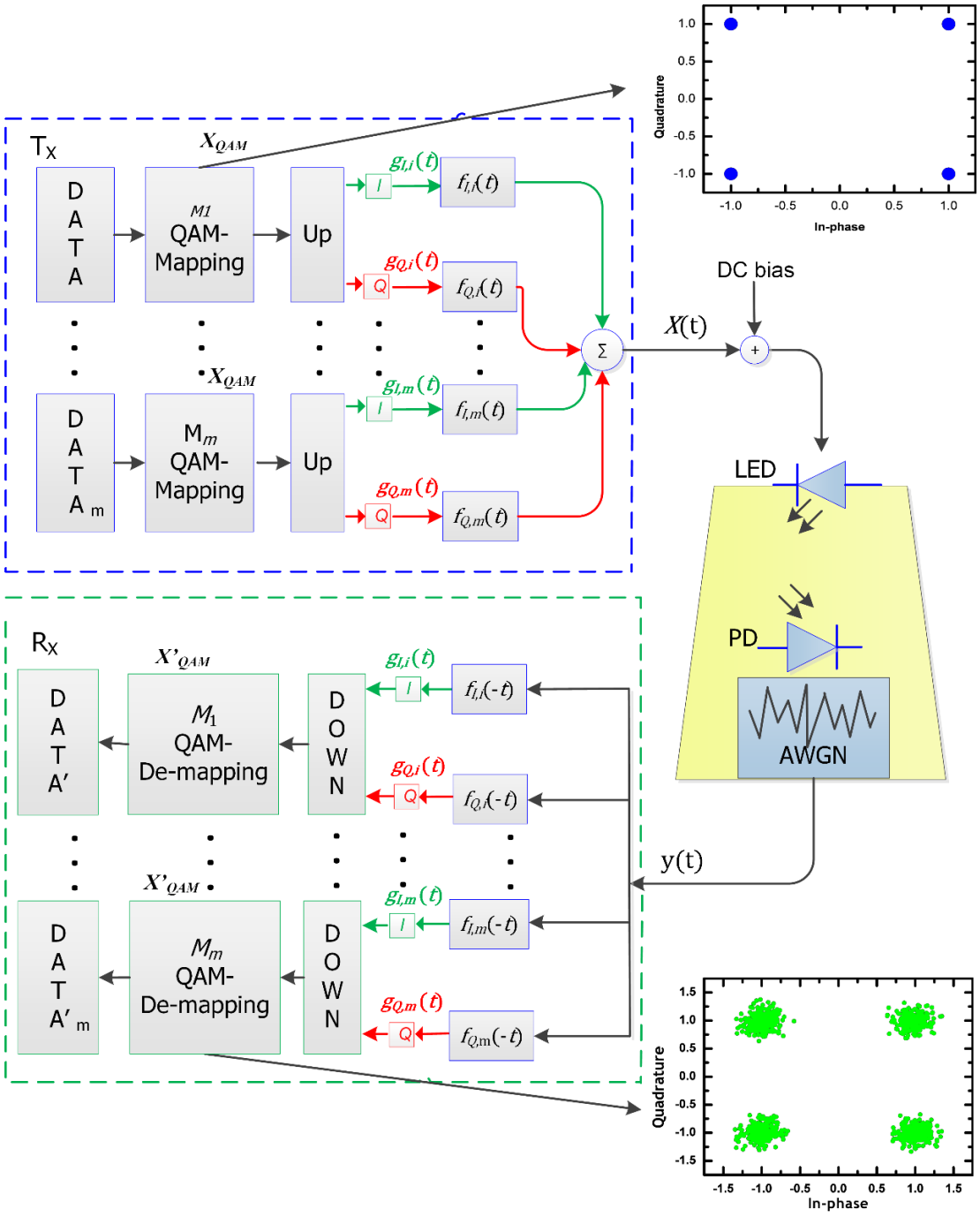

Figure 3.3. The schematic block diagram of an *m*-CAP VLC system. AWGN represents additive white Gaussian noise

In order to illustrate the *m*-CAP VLC structure, a schematic block diagram is shown in Figure 3.3. Firstly, at the Tx side, an *m* independent pseudo-random binary sequence (PRBS) "DATA" with a length of 2^x-1 is generated before being mapped into the *M*-

QAM constellation symbols $x_{QAM}(t)$ using the Gray mapping code, where the modulation order $M = 2^b$, and b is the number of bits/symbol. In order to match the sampling rate of the system (the transmitted bits and the FIR filters), $x_{QAM}(t)$ is then up-sampled (‘‘Up’’) by means of inserting zeros (zero padding) between consecutive symbols according to the number of samples/symbol (n_{samp}), which is given by [96]:

$$n_{samp} => 2m(1 + \beta), \tag{3.1}$$

where m represents the number of sub-carriers, and β is the roll-off factor of the square root raised cosine (SRRC) filter. β governs the excess bandwidth of the pulse in the frequency domain and also the rate at which the outside of the pulse tails decay in the time domain (samples) [106]. Furthermore, as shown in Figure 3.4(a) and (b) for β = {0 (green), 0.5 (orange), 1 (blue)}; having β = 0 offers the narrowest bandwidth. However, it also shows the slowest decay of the outside pulse intervals. On the other hand, having β = 1 offers the widest bandwidth, but the decay in the time domain is rapid.

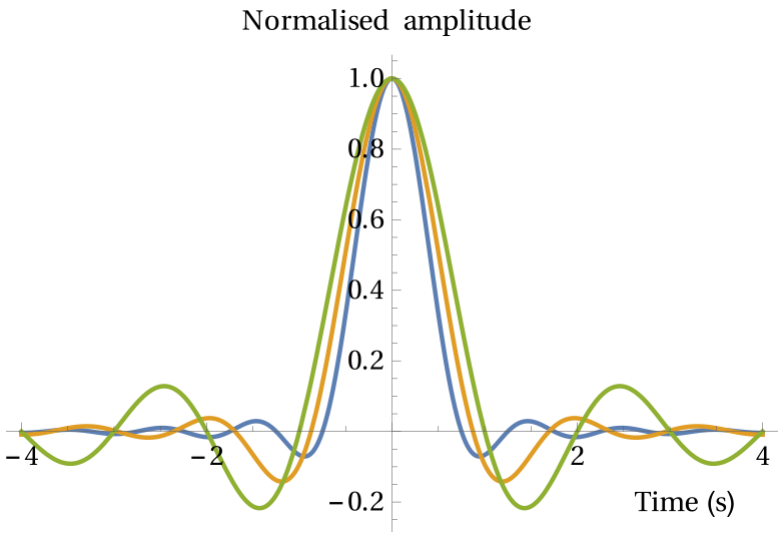

(a)

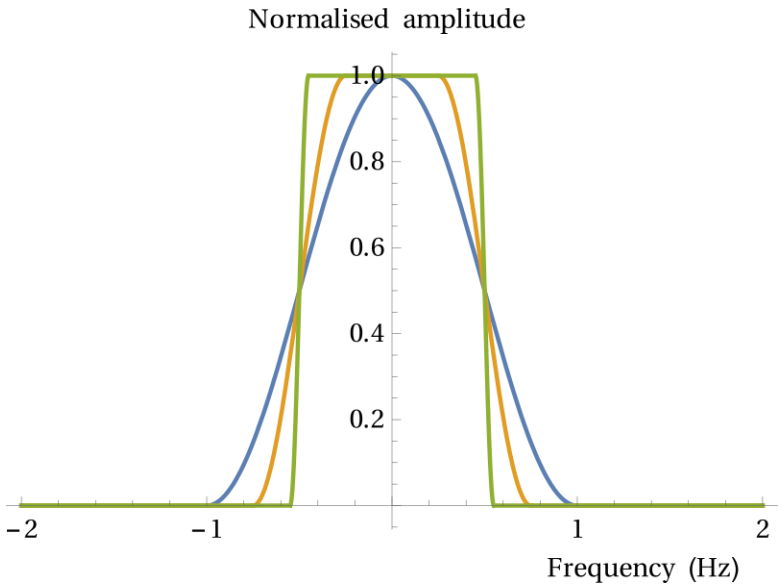

(b)

Figure 3.4. A baseband SRRC pulse in: (a) the time domain, and (b) the frequency domain for different values of β = {0 (green), 0.5 (orange), 1 (blue)}

The up-sampled $x_{QAM}(t)$ symbols are then split into the real $g_{I,i}(t)$ and imaginary $g_{Q,i}(t)$ symbols of the i^{th} sub-carriers prior to passing them through the in-phase $f_{I,i}(t)$ and quadrature $f_{Q,i}(t)$ SRRC transmit filters, whose impulse responses form a Hilbert pairs, orthogonal in time and separated by a 90° phase shift. In literature, there are many expressions for the SRRC filter impulse response. Throughout this research, the one given by [107] has been considered, which is given by:

$$p(t) = \begin{cases} 1 - \beta + \dfrac{4\beta}{\pi} & \text{if } t = 0 \\ \dfrac{\beta}{\sqrt{2}}\left[\left(1+\dfrac{2}{\pi}\right)\sin\left(\dfrac{\pi}{4\beta}\right) + \left(1-\dfrac{2}{\pi}\right)\cos\left(\dfrac{\pi}{4\beta}\right)\right] & \text{if } t = \pm\dfrac{T_s}{4\beta} \\ \dfrac{\sin\left(\dfrac{\pi t}{T_s}(1-\beta)\right) + 4\beta\dfrac{t}{T_s}\cos\left(\dfrac{\pi t}{T_s}(1+\beta)\right)}{\dfrac{\pi t}{T_s}\left(1-\left(4\beta\dfrac{t}{T_s}\right)^2\right)} & \text{elsewhere,} \end{cases} \tag{3.2}$$

where T_s is the symbol duration. In addition, attempting to increase the data rate in the band-limited VLC systems may result in the ISI phenomenon, which can be explained by the leakage of data (spread in the time domain) carried by the symbols to the adjacent

symbols. Thus, pulse shaping filters including SRRC are utilised to avoid or reduce the effect of ISI. When utilising pulse shaping filters, two criteria must be met in order to satisfy the ability to provide an ISI-free system: (*i*) the pulse shape must have a zero crossing at the sampling point for all pulse intervals; and (*ii*) the filters must have a pulse shape that ensures the outside of the pulse interval decays rapidly in terms of amplitude.

A *Sinc* pulse satisfies the first condition. However, it has an infinite length i.e., does not decay in the time domain, making it an unfeasible choice for digital implementation. A more practical choice is to use the raised cosine filter or its variant the SRRC filter, as they are a modified version of the Sinc pulse with an adjustable bandwidth of $\frac{(1-\beta)}{2T_s} \leq |f| \leq \frac{(1+\beta)}{2T_s}$ and a cosine correction applied to the *Sinc* (see Equ. (3.2)) in order to make it behave better by making the outside of the pulse intervals decay faster. In the frequency domain, the representation of $p(t)$ is given by [108]:

$$p(f) = \begin{cases} 1 & \text{for } |f| \leq \dfrac{(1-\beta)}{2T_s} \\ \left\{ cos\ \dfrac{\pi T_s}{2\beta}\ \left(|f| - \dfrac{(1-\beta)}{2T_s} \right) \right\} & \text{for } \dfrac{(1-\beta)}{2T_s} \leq |f| \leq \dfrac{(1+\beta)}{2T_s} \\ 0 & \text{for } |f| > \dfrac{(1+\beta)}{2T_s}. \end{cases} \tag{3.3}$$

It is worth mentioning that the SRRC filter has been dubbed so because of the fact that the frequency response of the SRRC filter (Equ. (3.3)) is nothing but the square root of the raised cosine filter's frequency response. Similarly, the raised cosine filter is referred to as such due to the presence of a cosine function in the frequency response.

The transmit impulse responses of the *I* and *Q* SRRC filters ($f_{I,i}(t)$ and $f_{Q,i}(t)$, respectively) are generated as shown in Figure 3.5. They are generated as the result of a

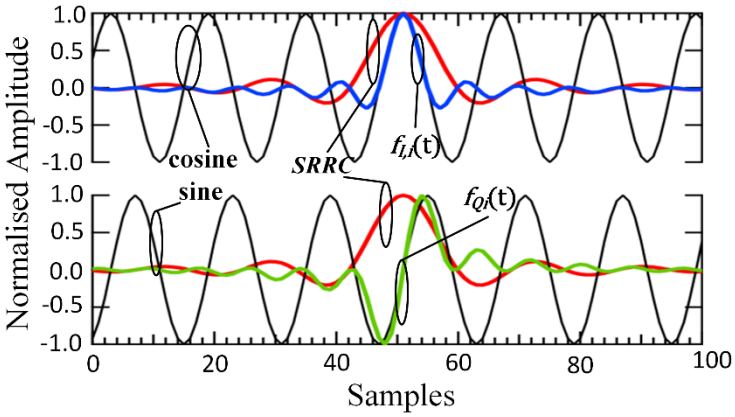

Figure 3.5. The impulse responses of the transmit *I* and *Q* SRRC filters $f_{I,i}(t)$ (top-blue) and $f_{Q,i}(t)$(bottom-green) respectively; adopted from [45]

cosine (*I*) or sine (*Q*) wave with the impulse response of the SRRC filter, and can be expressed as follows [92]:

$$f_{I,i}(t) = \cos\left(2\pi f_{c,i}t\right) \cdot \left[\frac{\sin\left(\frac{\pi t}{T_s}(1-\beta)\right) + 4\beta\frac{t}{T_s}\cos\left(\frac{\pi t}{T_s}(1+\beta)\right)}{\frac{\pi t}{T_s}\left(1-\left(4\beta\frac{t}{T_s}\right)^2\right)}\right]. \tag{3.4}$$

$$f_{Q,i}(t) = \sin\left(2\pi f_{c,i}t\right) \cdot \left[\frac{\sin\left(\frac{\pi t}{T_s}(1-\beta)\right) + 4\beta\frac{t}{T_s}\cos\left(\frac{\pi t}{T_s}(1+\beta)\right)}{\frac{\pi t}{T_s}\left(1-\left(4\beta\frac{t}{T_s}\right)^2\right)}\right]. \tag{3.5}$$

The carrier frequency for the i^{th} sub-carrier is given by [109]:

$$f_{c,i} = \frac{(2i-1)B_{\text{sig}}}{2m}, \tag{3.6}$$

where B_{sig} is the *m*-CAP signal bandwidth as given by:

$$B_{\text{sig}} = \frac{1}{T_s}(1+\beta)m. \tag{3.7}$$

It should be noted that carrier frequency of both (co)sine waves must be at least twice the highest frequency of the SRRC filter, and that β has a value of $0 \leq \beta \leq 1$. Moreover, as mentioned earlier in Section 3.2, selecting β appropriately is important because the minimum bandwidth requirement is proportional to $(1 + \beta)$. Moreover, larger β means a $(1 + \beta)$ greater bandwidth requirement and a β value closer to zero means perfect utilisation of the bandwidth, as shown in Figure 3.6 for 1-CAP [96].

The pre-transmission waveforms are generated by convoluting both up-sampled signals $g_{I,i}(t)$ and $g_{Q,i}(t)$ of the i^{th} sub-carrier with the transmit waveforms (i.e., the impulse responses of the SRRC filters ($f_{I,i}(t)$ and $f_{Q,i}(t)$), as follows:

$$X_{I,f,i}(t) = g_{I,i}(t) \otimes f_{I,i}(t), \tag{3.8}$$

$$X_{Q,f,i}(t) = g_{Q,i}(t) \otimes f_{Q,i}(t), \tag{3.9}$$

where $\otimes$ denotes time domain convolution.

The final waveform for transmission is implemented by subtracting the real and imaginary parts as given by:

$$X(t) = \sum_{i=1}^{m} X_{I,f,i}(t) - X_{Q,f,i}(t). \tag{3.10}$$

A DC bias is then added to $X(t)$ in order to make it unipolar. The DC biased $X(t)$ signal is then used to intensity modulate the LED.

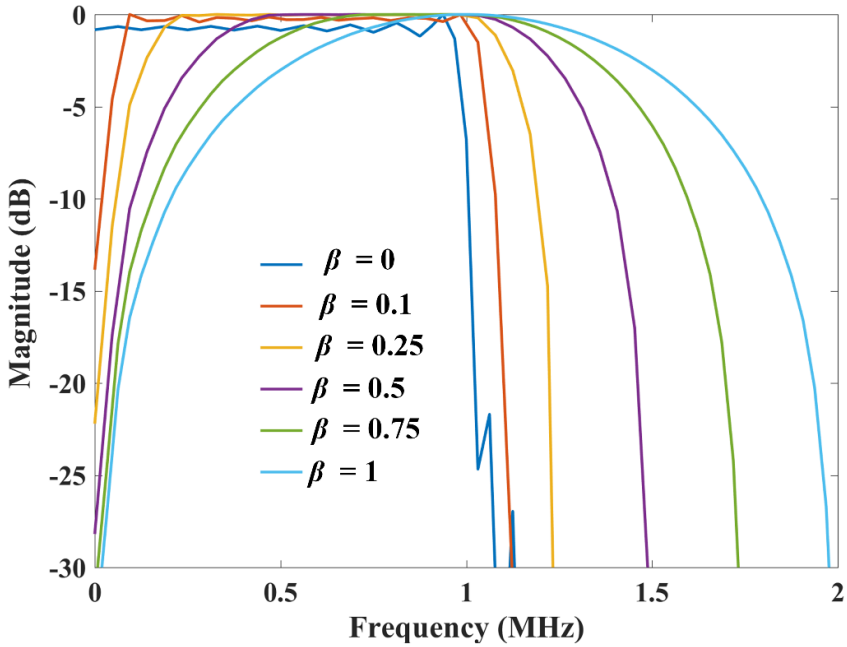

Figure 3.6. 1-CAP pulse shape in the frequency domain considering a range of β = {0, 0.1, 0.25, 0.5, 0.75, 1}

At the Rx, see Figure 3.3, the light is detected using an optical Rx composed of a PD and TIA. The received signal $y(t)$ is given by Equ. (2.3). Note that, the dominant noise sources are the ambient induced shots noise and the thermal noise, which were defined in terms of variance in Equs. (2.7), and (2.8), respectively. The signal $y(t)$ is then passed through the time-reversed in-phase $f_{I,i}(-t)$ and quadrature $f_{Q,i}(-t)$ filters, where the output *I* and *Q* components are then down-sampled; removing the n_{samp} added zeros (i.e., throwing away samples (‘‘Down’’)), followed by the QAM constellation de-mapping in order to recover the estimated version of the data (DATA’).

3.4 Experimental Test Setup

3.4.1 System Model

In this subsection, an experimental implementation of the proposed *m*-CAP VLC is outlined, for the first time. A schematic block diagram of the *m*-CAP system is shown in Figure 3.7. The first block generates a 2^{17}-1 PRBS NRZ signal format for each sub-carrier up to the required number of sub-carriers (''$Data_m$''), where *m* denotes the number of sub-carriers. The data is then mapped into the M_m-QAM cardinality $X_{\mathrm{QAM}m}$, where *M* is the modulation cardinality and *b* can be calculated as $b = \log_2 M$. For instance, for transmitting a binary phase shift keying (BPSK) signal format the value of *b* will be 1.

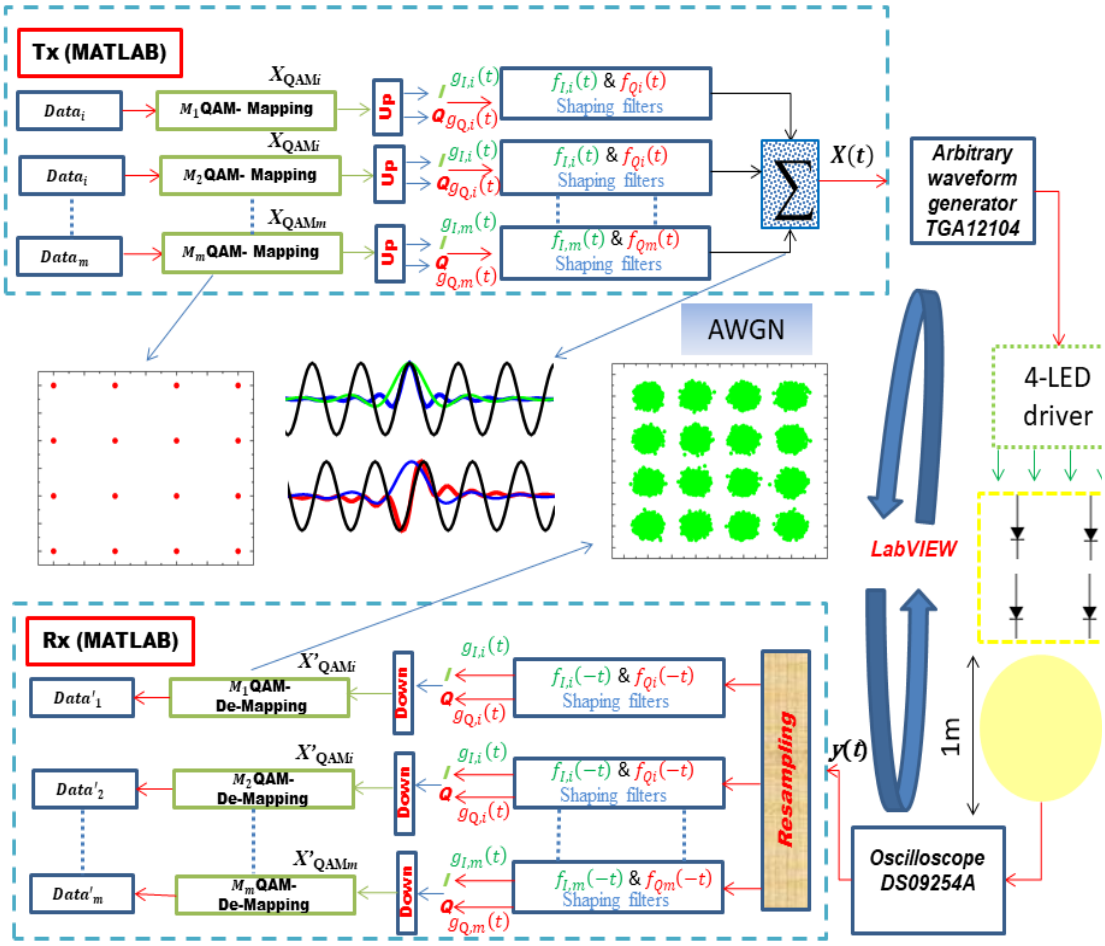

Figure 3.7. A schematic block diagram of the *m*-CAP system under test

The transmitted data is then up-sampled (‘‘Up’’) by n_{samp} as given in (3.1) in order to match the system sampling frequency before being split into two parts, namely $I\ g_{I,i}(t)$ and $Q\ g_{Q,i}(t)$ of the i^{th} sub-carriers. As mentioned earlier in this chapter (section 3.2), the two parts of the data (*I* & *Q)* are then passed through the *I* transmit and *Q* transmit FIR filters $f_{I,i}(t)$ and $f_{Qi}(t)$, respectively, whose impulse responses are generated as a result of multiplication between a cosine (*I*) or sine (*Q*) wave with the impulse response of the SRRC filter to form a Hilbert pair as given in Equs. (3.4) and (3.5), respectively.

The resulting transmit waveforms $f_{I,i}(t)$ and $f_{Qi}(t)$ are convoluted with the up-sampled baseband signals $g_{I,i}(t)$ and $g_{Q,i}(t)$ for the i^{th} sub-carriers to form the pre-transmission waveforms as given in Equs. (3.8) and (3.9).

The final waveform for transmission ($X(t)$) is implemented by subtracting the real and imaginary parts of the pre-transmission filters, $X_{I,f,i}(t)$ and $X_{Q\ f,i}(t)$, as in (3.10). The signal $X(t)$ is then used to intensity modulate the utilised LED (Ce:YAG/GaN), which had a B_{mod} of ~4.5 MHz. For the targeted set of sub-carriers (m = {1, 2, 4, 6, 8, 10}), the bandwidth of each sub-carrier is given as the ratio of the total signal bandwidth B_{tot} to the number of sub-carriers. Furthermore, in this experiment, B_{tot} was set to 6.5 MHz due to the sampling rate capability of the TTI TGA12104 arbitrary waveform generator utilised in the experiment. Thus, a high frequency attenuation was expected due to the 2 MHz present out of the -3dB shoulder imposed by the utilised LED, which had a B_{mod} of ~4.5 MHz. The distribution of the signal bandwidth for each sub-carrier is illustrated as in Figure 3.8.

As it can observed from Figure 3.8, B_{tot} was set to 6.5, 3.25, 1.625, 1.083, 0.8125 and 0.65 MHz for m = {1, 2, 4, 6, 8, 10}, respectively.

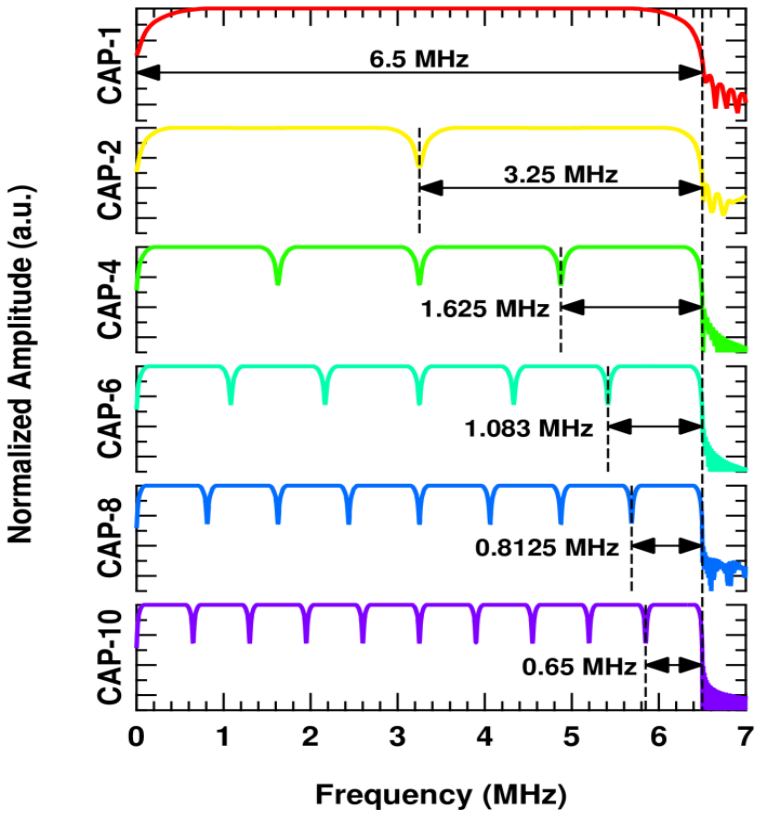

Figure 3.8. The ideal signal frequency response and bandwidth of each sub-carrier for a set of m = {1, 2, 4, 6, 8, 10} [45]

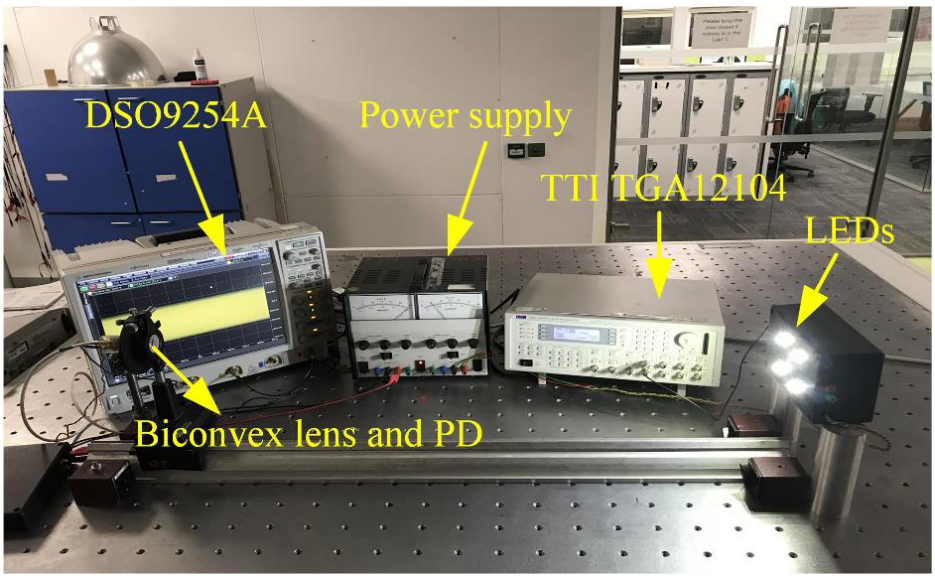

Figure 3.9. The experimental setup of the tested m-CAP systems

As shown in Figure 3.9, the output waveform of the shaping filters $X(t)$ was subsequently fed to the arbitrary waveform generator TTI TGA12104, which was controlled using a labVIEW program that in turn passed the transmitted signal to a custom transmission

driving circuit in the form of a current mirror with four arms that intensity modulated four individual LEDs with the same signal. The LEDs were biased at a DC current of 350 mA to ensure operation in the linear region (see Figure 3. 10 depicting the measured light-intensity-volt (L-I-V) curves).

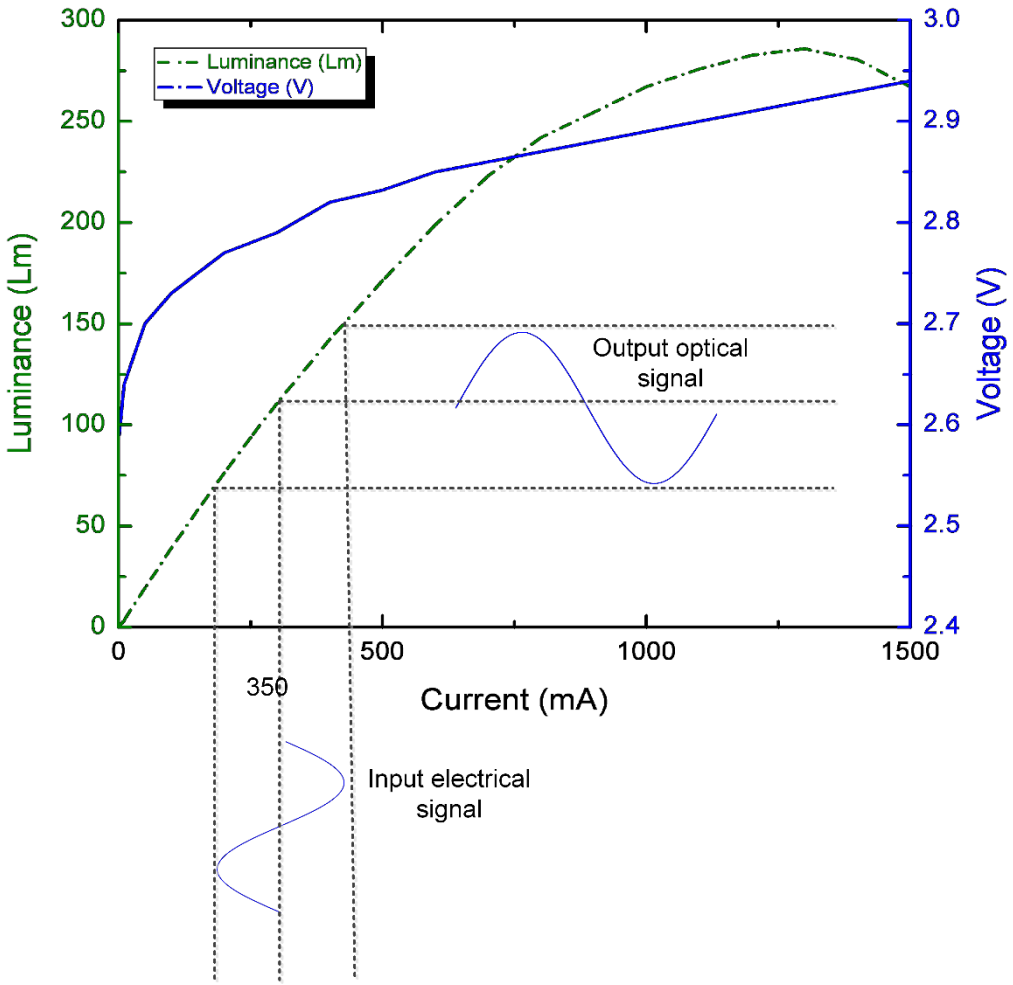

Figure 3. 10. The measured L-I-V curves of the utilised LEDs, also depicted the linear region with a DC bias point of 350 mA [45]

The key parameters of the experimental setup are given as in Table 3. 1. The intensity modulated signal was then propagated through a free space channel of 1 m length. At the Rx side, the optical signal was focused onto a PD (OSD15-5T) using a 25 mm biconvex lens with a focal distance of 25 mm. Following optoelectronic conversion and amplification using TIA, the regenerated signal was digitised using a digital storage oscilloscope (Agilent DSO9254A).

LabVIEW was then used to control the oscilloscope (DSO9254A) in order to capture the received signal $Y(t)$ and save it for further offline processing using MATLAB. $Y(t)$ was first passed using a 4th order butterworth LPF with a cut-off frequency set at the highest signal frequency of the system (i.e., 6.5 MHz) to filter out the high frequency noise components. Following low pass filtering, the filtered signal $Y(t)$, which is defined in (2.3) was resampled in order to match the sampling frequency of the reference version (i.e., transmitted signal). The resampled signal was then passed through the in-phase and quadrature time-reversed pulse shaping filters, $f_{I,i}(-t)$ and $f_{Q,i}(-t)$, respectively. The baseband split signals representing the in-phase $g_{I,i}(t)$ and quadrature $g_{Q,i}(t)$ components were then down-sampled by removing the n_{samp} added zeros (''Down''), and the symbols were subsequently de-mapped ($X'_{\mathrm{QAM}m}$). Finally, the estimated version of the data (Data'$_m$) was recovered.

Table 3. 1. Experimental work and PD parameters

Parameter	**Value**
Data-NRZ pseudorandom binary sequences length	2^{17}-1
LED - Cool white (5650K) LUXEON Rebel ES	
• LED bandwidth B_{mod}	4.5 MHz
• LED beam angle	120°
Total signal bandwidth	6.5 MHz
Transmission span L	1 m
PD - silicon OSD15-5T	
• Active area	15 mm^2
• Responsivity $\mathcal{R}$	0.21 A/W
• Bandwidth	29 MHz
PD's Convex lens	
• Focal length	25 mm
• Diameter	25 mm

3.4.2 **Results and Discussion**

In this section, the first ever experimental evaluation of a VLC link utilising the *m*-CAP scheme is outlined by investigating the impact of different orders (i.e., m = {1, 2, 4, 6, 8, 10}) on the link data throughput and the BER.

As the flowchart in Figure 3.11 illustrates, in order to maximise system performance, a bit-loading technique was adopted as follow. In the first instance, a BPSK pilot signal was transmitted on each sub-carrier in order to measure the error vector magnitude (EVM) from the received BPSK constellation, prior to SNR estimation of the i^{th} sub-carrier as adopted in [110, 111] and is given by:

$$\mathrm{SNR}_i \approx \frac{1}{\mathrm{EVM}_i^2}. \tag{3.11}$$

The EVM is one of the widely known figure of merits that used to evaluate the quality of the system. Moreover, EVM represents the effect of distortion induced in the system. EVM can be defined as the difference (error) between the received measured symbols and the ideal version (reference) of the transmitted symbols as illustrated in Figure 3.12. Furthermore, in order to measure EVM, the knowledge of the ideal transmitted constellation points (reference) of the system is required, which is expressed as [110-112]:

$$\mathrm{EVM} = \frac{\frac{1}{N_s}\sum_{n=1}^{N_s}|S_r(n_s) - S_t(n_s)|^2}{P_{max}}, \tag{3.12}$$

where $N_s$is the number of symbols for the *I* and *Q* components, $S_r(n_s)$ and $S_t(n_s)$ are the received and ideal transmitted symbols, respectively, and P_{max} is the maximum normalised ideal symbol power.

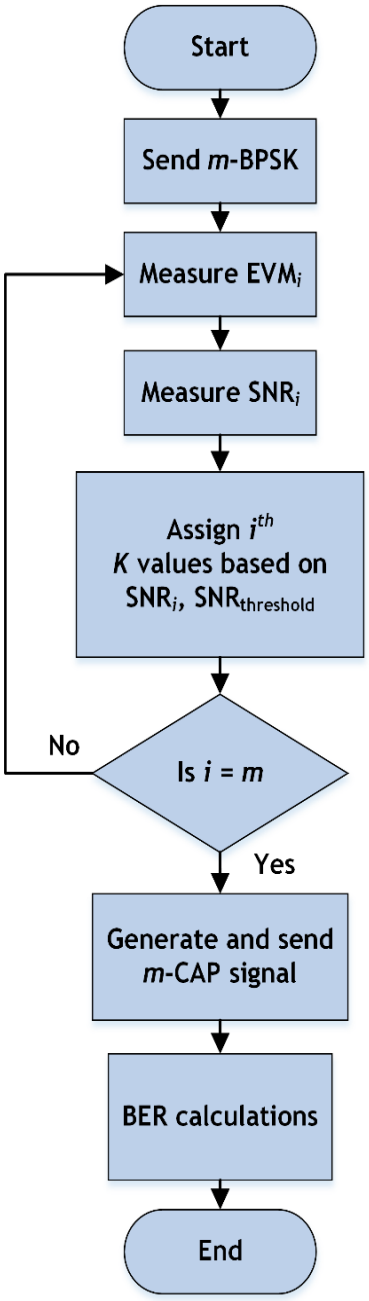

Figure 3.11. A flowchart illustrating the operation of the bit loading technique, the generation of the *m*-CAP signals and the BER calculations

Having measured EVM and based on the estimated SNR, which is compared with predicted SNRs ($SNR_{thresholds}$) determined based on the required BER target, each sub-carrier was assigned the appropriate number of bits/symbol *b*. The next step checks if $i = m$, where *i* is the sub-carrier number and *m* the number of sub-carriers. If $i \neq m$, then EVM and SNR were measured, otherwise the *m*-CAP signals were generated for transmission and finally the BER was determined.

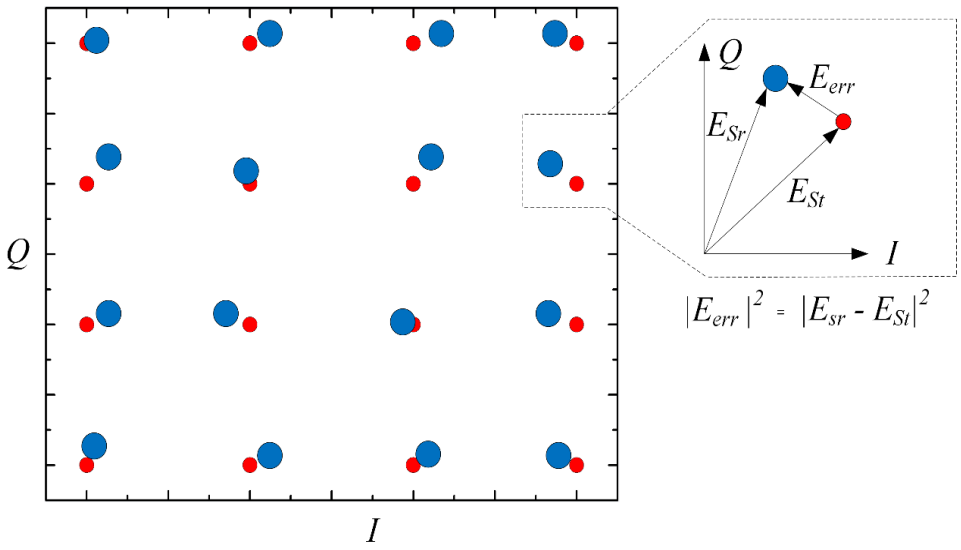

Figure 3.12. Constellation diagram of 16-QAM's ideal transmitted symbols (red) and received symbols (blue). Also, depicted on the top right is an illustration of the calculation process of the vectorial error difference between the received and the ideal transmitted symbols

Although the number of captured bits exceeded 10^5 bits, the BER target was set at 10^{-3} with a small error allowance for the forward error correction (FEC) of 7% and 20% for the BER limits of 3.8×10^{-3} and 2×10^{-2}, respectively [45]. As stated earlier, following transmission of the BPSK pilot signal, measuring EVM and estimating the SNRs per sub-carrier, the measured and predicted [113] SNRs were compared, where predicted $SNR_{thresholds}$ = {6.7, 9.5, 10.5, 13.5, 14.7, 18} dB for b = {2, 3, 4, 5, 6, 7} bits/symbol respectively at the target BER (i.e., 10^{-3}).

The measured SNR against the number of sub-carriers for m = {1, 2, 4, 6, 8, 10} for a range of M-QAM orders is illustrated in Figure 3.13. It can be clearly observed from Figure 3.13 that, the minimum measured SNR value of ~5 dB for the 1st sub-carrier is lower than the minimum $SNR_{thresholds}$ value for 4-QAM (6.7 dB). However, it is more beneficial to use 4-QAM instead of BPSK (b = 1) for this particular sub-carrier at the cost of a higher BER (i.e., ~10^{-2}), which is still below the 20% FEC limit. On the other hand, the maximum measured SNR is 23.22 dB for the 4th sub-carrier of highest m-CAP order utilised in this experimental work (i.e., 10-CAP).

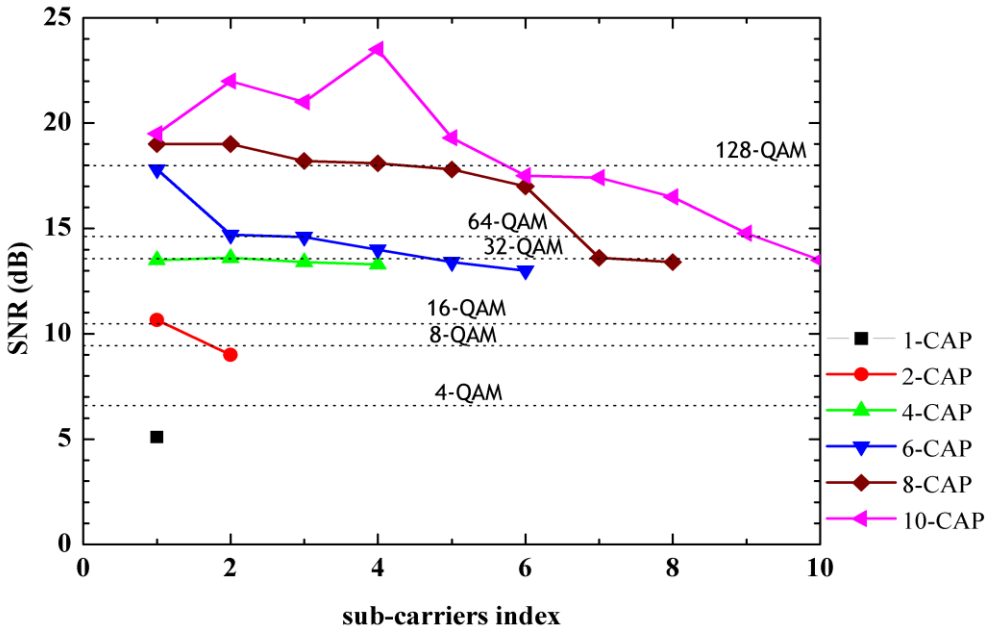

Figure 3.13. The measured SNR per sub-carrier from the BPSK pilots against the number of sub-carriers for a range of *m*-CAP orders. The theoretical SNR thresholds are also shown as dashed lines [45]

The adaptive bit-loading technique was implemented where each sub-carrier of the dedicated *m*-CAP orders was assigned the appropriate number of bits/symbol (*b*) in accordance to the achieved SNR obtained from the measured EVM, see Figure 3.14, and were subsequently loaded into the TTI TGA12104 waveform generator.

Following the procedure outlined above (see Figure 3.11), the *m*-CAP signals were generated and transmitted, and finally, the data rate and BER were determined. Overall, for $m > 1$ all the aggregate measured BER values were ~10^{-3}, which are shown with a linear fit in Figure 3.15, with the sole exception of the conventional 1-CAP as it achieved a BER of 10^{-2}, which is above the 7% FEC but still below the 20% FEC limit. Moreover, the 7% FEC limit was comfortably met for $m > 1$. However, for $m = 1$, the 20% FEC limit was adopted.

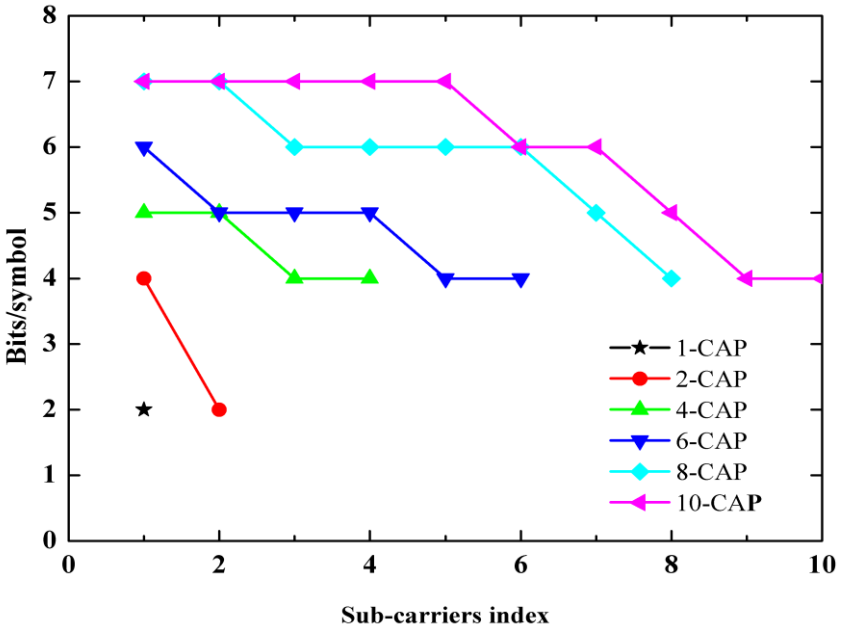

Figure 3.14. The assigned number of bits/symbol for each sub-carrier of different sets of m = {1, 2, 4, 6, 8, 10} [45]

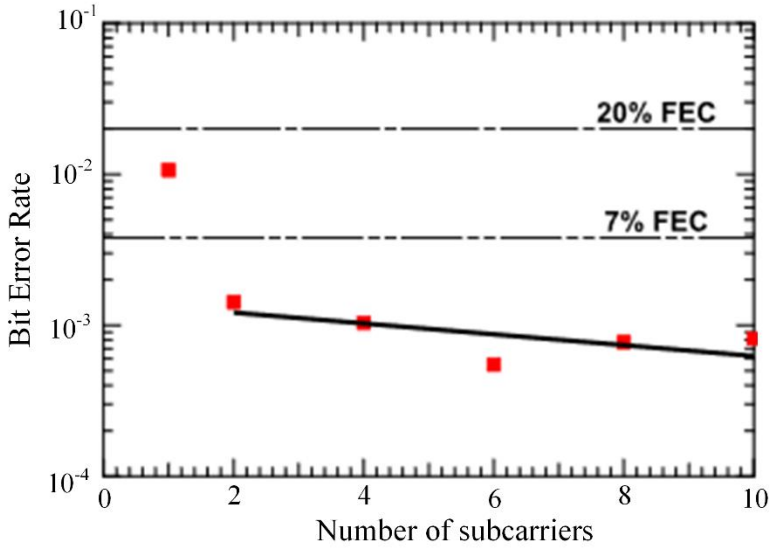

Figure 3.15. The aggregate measured BER for each order of the utilised m-CAP systems [45]

The performance of each m-CAP signal is discussed below in order from the conventional 1-CAP to the highest order (i.e., 10-CAP).

3.4.3 **1-CAP System**

By utilising the conventional 1-CAP system, a data rate of only 11.3 Mb/s could be achieved. Recall that, the achieved BER is 10^{-2}, for this particular 1-CAP system, therefore a higher bits/symbol and 4-QAM were used but at the cost of higher BER. Following the removal of the 20% FEC limit, the achieved overall data throughput and the spectral efficiency of the conventional 1-CAP system were reduced to 9.04 Mb/s and 1.4 b/s/Hz, respectively. The reason behind achieving a slow transmission speed for the conventional 1-CAP stems from the high sensitivity of the non-flat fading channel introduced by the LED bandwidth limitation. Furthermore, the transmitted signal encountered different channel frequency responses since a part of it (2.5 MHz) was outside of the -3 dB bandwidth, which severely affected the measured SNR, and therefore the link BER performance.

3.4.4 **2-CAP and 4-CAP Systems**

For the 2-CAP system, both the transmission speed and the spectral efficiency achieved were 15.78 Mb/s and 2.43 b/s/Hz, respectively following the removal of the 7% FEC limit. This is significant as it shows an improvement of 6.74 Mb/s by only dividing the signal bandwidth into two sub-carriers. For the 4-CAP system, the gross transmission speed achieved was 25.40 Mb/s. Considering the error margin allowance of 7% FEC, the data rate achieved was 23.62 Mb/s (3.63 b/s/Hz), which again shows an improvement of 7.87 Mb/s in contrast to the 2-CAP system and approximately double that value (14.58Mb/s) in comparison to the conventional 1-CAP system. The increase in system capacity can be attributed to a reduction in the sub-carriers bandwidth, as the sub-carrier bandwidth for the 4-CAP was 1.625 MHz, compared with 3.25 MHz and 6.5 MHz for the 2-CAP and the conventional 1-CAP systems, respectively. This reduction in the *m*-CAP

signals bandwidth resulted in increased SNRs in each sub-carrier so more bits-per-sub-carrier could be loaded by applying the previously mentioned adaptive bits load technique. As a result, one can notice that, by utilising up to $m = 4$, a gradual increase in the system data throughput and the spectral efficiency can be achieved.

3.4.5 **6-CAP System**

Further improvement in the transmission speed can be achieved by using higher order i.e., through a 6- and 8-CAP systems. For 6-CAP a speed of 25.4 Mb/s and a spectral efficiency of 3.9 b/s/Hz were achieved after removing the 7% FEC limit. This does not constitute a significant improvement in the system efficiency, as an increase of only 0.3 b/s/Hz was achieved in contrast to the 4-CAP system. This improvement appears especially minor when we bear in mind that adding two sub-carriers to the system (6-CAP) means four pulse shaping filters are needed (two for real data and two for imaginary data) at the transmitter and another four at the receiver side as well. Therefore, the system complexity can be reduced while maintaining nearly the same system efficiency by omitting the 5^{th} and 6^{th} sub-carrier at no significant reduction in system efficiency.

3.4.6 **8-CAP and 10-CAP Systems**

The achieved data rate (spectral efficiency) for the 8-CAP system after removal of the headers (7% FEC) was 30.88 Mb/s (4.75 b/s/Hz); an increase of 5.48 Mb/s in comparison to the 6-CAP system, and a substantial 21.84 Mb/s increase in the transmission speed in comparison to the conventional 1-CAP system. Figure 3.16 depicts the measured and normalised frequency spectra of the received 10-CAP signal for a total signal bandwidth of 6.5 MHz; while the insets show the corresponding constellation diagrams of the 1^{st} (red), 6^{th} (blue), and 10^{th} (green) sub-carriers.

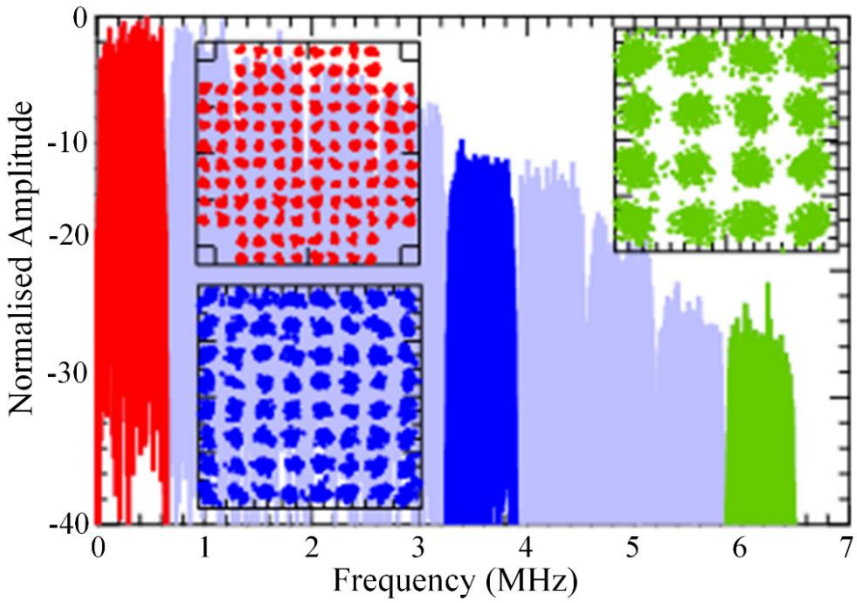

Figure 3.16. The measured electrical spectrum of the 10-CAP system. Insets: the constellations for the 1st (red), 6th (blue) and 10th (green) sub-carriers [45]

The EVM_{RMS} values for the three mentioned constellations diagrams are 4.17%, 7.73% and 15.66%, respectively. The best transmission speed and spectral efficiency achieved among the various *m*-CAP systems tested in this work was obtained for the 10-CAP system, with values of 31.53 Mb/s and 4.85 b/s/Hz achieved for the transmission speed and spectral efficiency respectively. However, the 10-CAP system showed only 0.65 Mb/s (0.1 b/s/Hz) enhancement in the transmission speed over the 8-CAP system performance. Therefore, once again, the two additional sub-carriers between the 10-CAP and 8-CAP systems can be omitted in favour of system complexity reduction, as they do not contribute towards a vital system capacity improvement. Figure 3.17 illustrates the data rate achieved by the different *m*-CAP systems.

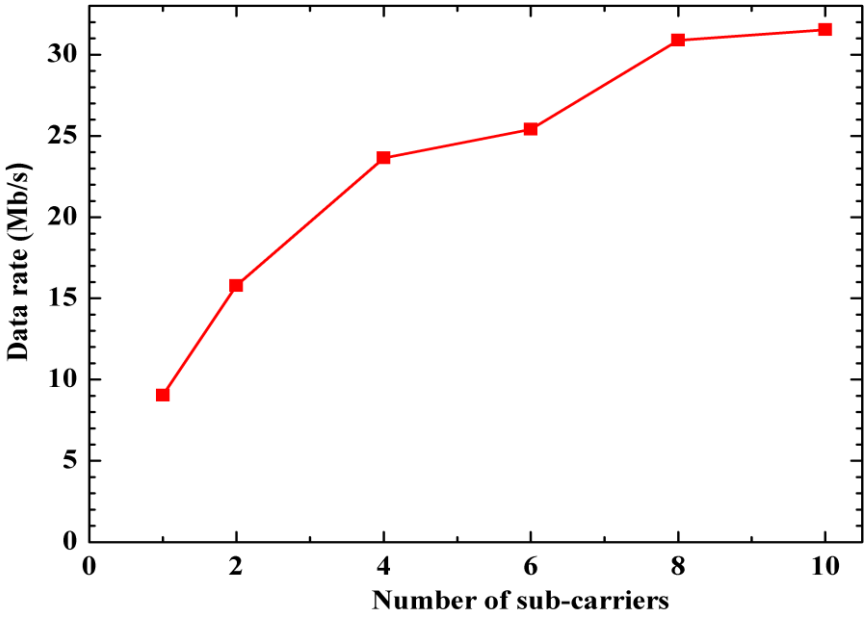

Figure 3.17. The achieved data rate (Mb/s) for each *m*-CAP system [45]

3.5 Summary

In this chapter, a detailed discussion of the fundamentals of the new proposed *m*-CAP scheme has been given as well as a full explanation of the process of generating the *m*-CAP signals. For the first time in VLC, an experimental work utilising an *m*-CAP system was demonstrated for a link span of 1 m. Moreover, the effect of increasing the number of sub-carriers (*m)* on the throughput/spectral efficiency has been studied, where the number of sub-carriers was varied according to $m = \{1, 2, 4, 6, 8, 10\}$ over a fixed total signal bandwidth of 6.5 MHz. Increasing *m* has led to an increase in the *m*-CAP systems' data rate and spectral efficiency, as it was shown that transmission speeds (spectral efficiencies) of 9.04 (1.4), 15.78 (2.43), 23.62 (3.63), 25.4 (3.9), 30.88 (4.75) and 31.53 (4.85) Mb/s (b/s/Hz) can be achieved for the aforementioned values of *m*, respectively.

Chapter 4 MULTI-BAND CAP WITH DFE FOR BAND-LIMITED VLC AND FIR PARAMETERS IMPACT

4.1 Introduction

In Chapter 3, the *m*-CAP technique is introduced, which results in relaxing the requirement of non-frequency selective channel response by dividing the desired signal bandwidth into *m*-sub-bands (or sub-carriers for consistency with OFDM nomenclature). This is due to the fact that CAP has been shown to be very sensitive to an uneven system response [45, 96], as in intensity modulation based VLC systems. Thus, by increasing *m*, the sub-carriers can be approximated by a flat band response with varying levels of attenuation. However, for large sub-carriers, uneven attenuation will still be experienced due to the fact that some sub-carriers will be out of the -3 dB shoulder imposed by the utilised LED, thus resulting in ISI. In literature, it has been shown that for bandlimited VLC systems, a higher transmission speed is attainable when employing different equalisation techniques to remove ISI [29, 35, 77, 114]. Equalisation can be employed either at the Tx prior to intensity modulation, and/or at the Rx. At the Rx post-detection, both linear and non-linear equalisations as well as artificial neural network (ANN) based classifiers have been used

[35]. Equalisation could also be readily adopted in *m*-CAP to increase the data rate; a technique that still requires further investigation. In this chapter, a numerical investigation of the *m*-CAP performance with digital equalisation (i.e., decision feedback equaliser (DFE)) in the context of a bandlimited VLC system is introduced for a range of sub-carriers (m = {1, 2, 5, 10}). DFE is adopted because of its ability in mitigating high ISI compared to linear equalisers, which are not capable of producing a non-linear relationship between the input and output [115].

The *m*-CAP technique is an emerging and promising modulation scheme for VLC systems, and as such, it is necessary to investigate the impact of the utilised parameters on such a scheme that affect the overall system performance. For instance, as in an *m*-CAP system the carrier frequencies are generated by FIR pulse shaping filters, parameters such as β and the filter length L_f (taps/filter) of the utilised FIR filters in both the Tx and the Rx have a significant effect on the overall system performance and complexity, and thus need to be investigated. If *m*-CAP is to be adopted in systems that have a limited integration density such as in field programmable gate arrays (FPGAs), it is then crucial to balance the system performance and the complexity. Thus, in this chapter, an investigation of the performance of an *m*-CAP system utilising different β = {0, 0.1, 0.2, 0.3, 0.4, 0.5, 0.6, 0.7, 0.8, 0.9, 1} and different L_f = {2, 4, 6, 8, 10, 12, 14, 16} symbols is provided through numerical simulations.

In addition, a further insight on the *m*-CAP-VLC system performance in terms of the achieved data rates and spectral efficiencies when considering different parameters of the FIR filter (i.e., L_f (taps/filter) and β) for different sets of m is provided. This is achieved through an experimental work conducted to gain a better physical understanding of the relationship between the system behaviour and the computational complexity.

4.2 Equalisation Theory and Types

In this section, the fundamentals of equalisers are briefly introduced. Equalisers are often used when the system is bandlimited, which often leads to the ISI phenomenon. ISI can be thought of as the leakage of the symbol energy (spread in the time domain) into the adjacent successive symbols [117]. Equalisers are utilised to mitigate the ISI caused by the data being transmitted outside B_{mod}, or in other words, to mitigate the undesirable impacts of the channel response on the system performance.

There are two types of equalisers; analogue and digital, which comprise different subtypes as shown in Figure 4.1.

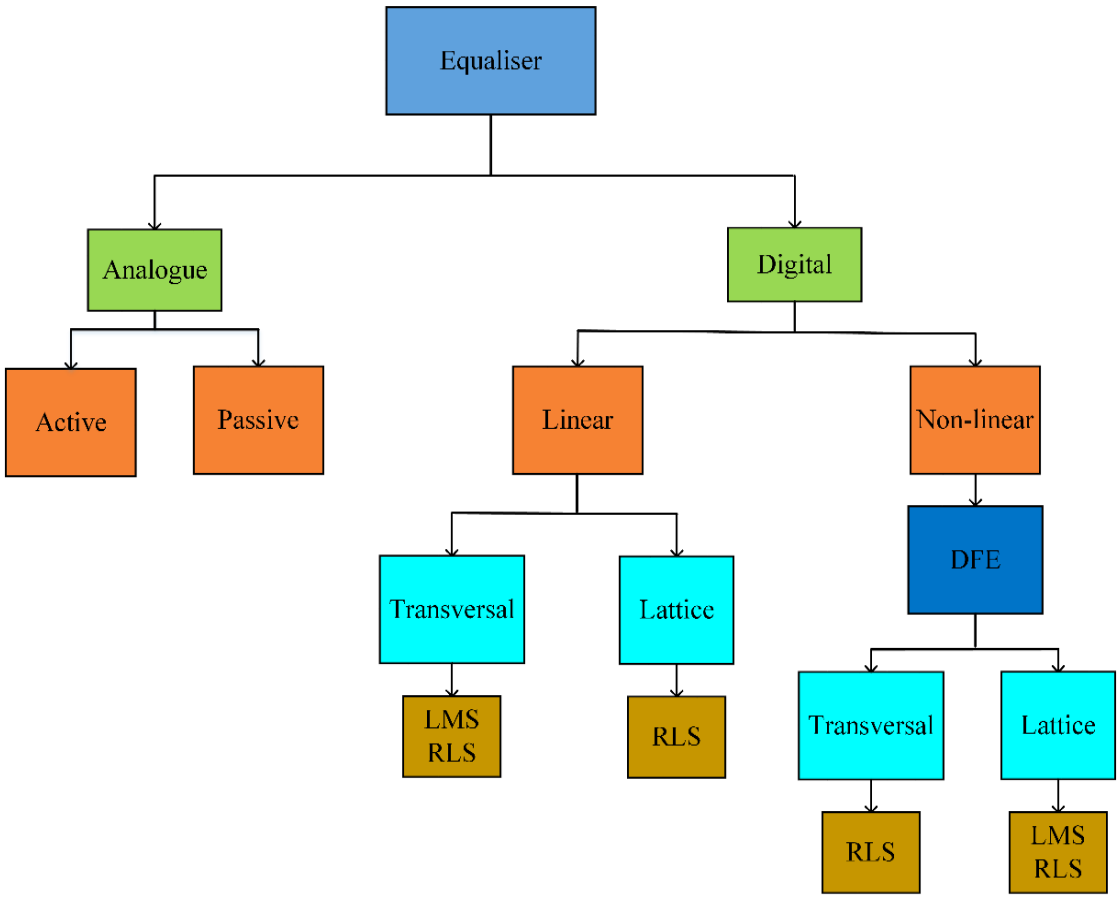

Figure 4.1. A list of the most popular equalisers, from [116]

Analogue equalisers consist of active components, which are dubbed as such because they add power into the system, such as power operational amplifiers; or passive components, such as resistors, capacitors and inductors. The most commonly utilised passive equaliser is the resistor and capacitor (RC) high pass filter equaliser circuit. The idea behind such an equaliser is to increase the B_{mod} of an LED when fitted prior to it [43]. It is worth mentioning that, passive equalisers are characterised by their relative simplicity. However, they offer a limited B_{mod} improvement due to the associated power penalty [118]. Depending on whether it is fitted at the Tx side or the Rx side, it is dubbed pre-equaliser or post-equaliser, respectively. The concept proposed by active equalisers is the same as that adopted in passive equalisers; with the only difference being the use of an active filter. Thus, additional power is introduced into the overall system frequency response. For instance, in [118], a data transmission speed of 300 Mb/s was achieved for a BER of 10^{-9}.

In the digital domain, digital equalisers are divided into two main types; linear and non-linear equalisers. Linear equalisers offer lower complexity than their non-linear counterparts. However, the price to pay here is having a reduced BER performance. Digital equalisers work on the principle of removing ISI by calculating the contribution of energy leaking on the current symbol from the previously transmitted symbol. These calculations are achieved by comparing a known set of data sequence that is stored in a memory with the received version of the same data sequence during the start of any transmission sequence. As such, this does not require a feedback path. This is known as "training", and the estimation is achieved by updating the equaliser's coefficients through implementing an iterative method.

The zero forcing equaliser (ZFE) is the most famous linear equaliser, and as the name suggests, it enforces a flat magnitude response by mitigating ISI [115]. This is achieved

by inversing the undesirable impact on the system performance, and the overall system frequency response (transfer function) is generally expressed as [29]:

$$H(f) = \frac{1}{Y(f)}, \tag{4.1}$$

where $Y(f)$ is the Fourier transform of the system response at the output. The drawback of ZFE is that it is very susceptible to noise [115].

Further improvements can be attained by utilising the adaptive linear equalisers, where the filter coefficients are adjusted in a periodic basis to match the channel characteristic by optimising a specified performance criterion. Several adaptive algorithms exist, with the most common being the least mean squares (LMS) and the recursive least squares (RLS). The RLS algorithm offers a much faster convergence speed to a lower error floor than the LMS algorithm at the cost of increased complexity [119].

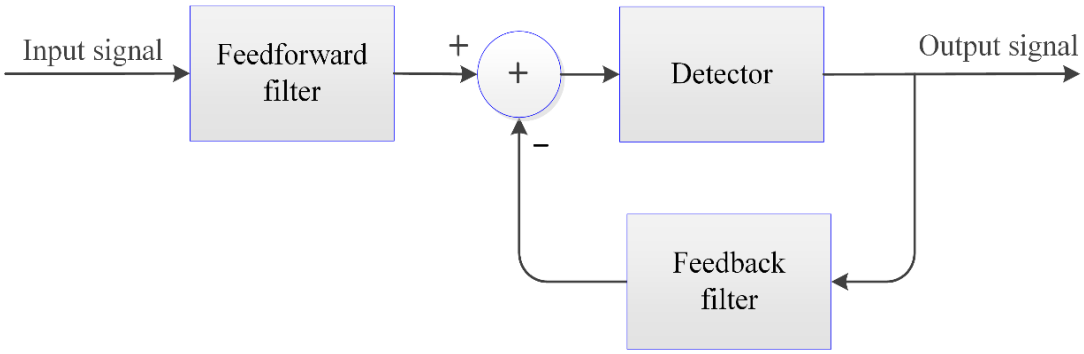

Figure 4.2. A block diagram of a basic DFE, adapted form [115]

The performance of an equaliser is directly linked to the severity of ISI experienced in the system. For severe ISI, linear equalisers fail due to being incapable of producing a non-linear relationship between the input and output [115]. Thus, it is necessary to adopt a non-linear DFE, which works on the principle of calculating the influence of ISI in the current symbol based upon the previously detected symbol. Moreover, the performance of DFEs is generally superior to linear transversal filters.

As shown in Figure 4.2, the DFE equaliser consists of two digital filters. The first filter is a feedforward filter, which whitens the noise and produces a response with post-cursor ISI only. The feedforward filter is generally a fractionally spaced FIR filter with adjustable tap coefficients and is identical to linear filters. The second filter is a feedback FIR filter with symbol-spaced taps of adjustable coefficients, which cancels the post-cursor ISI produced from the feedforward filters [115]. As shown in Figure 4.2, the input of the feedback filter is a set of the previously detected symbols, and its output is fed back to be subtracted from the output of the feedforward filter to form the input to the detector. Thus, the ISI introduced by previously detected symbols on the presently estimated symbols can be removed using the feedback filter.

4.3 *m*-CAP with and without DFE

The *m*-CAP format proposes that the signal attenuation per sub-carrier is less than that of a single sub-carrier over the entire allocated signal bandwidth. In this section, a numerical investigation of the *m*-CAP link performance employing a DFE for $m = \{1, 2, 5, 10\}$ is presented [120]. The system bandwidth (B_{sys}) is set to unity (1 Hz) without any loss of generality. In order to further illustrate the *m*-CAP structure utilising DFE, a schematic block diagram is illustrated in Figure 4.3.

Firstly, an *m* independent 10^5 length PRBS is generated before mapping into an *M*-quadrature QAM constellation using Gray mapping. The mapped data is up-sampled (‘‘Up’’) before being split into real *I* and imaginary *Q* components, which are then passed through the in-phase and quadrature transmit filters, whose impulse responses (IRs) form a Hilbert pair, orthogonal in time and separated by a 90° phase shift. The filter IRs are the result of a time domain convolution of a cosine (*I*) or sine (*Q*) wave with the IR of an SRRC filter. It should be noted that the carrier frequency of both (co)sine waves must be

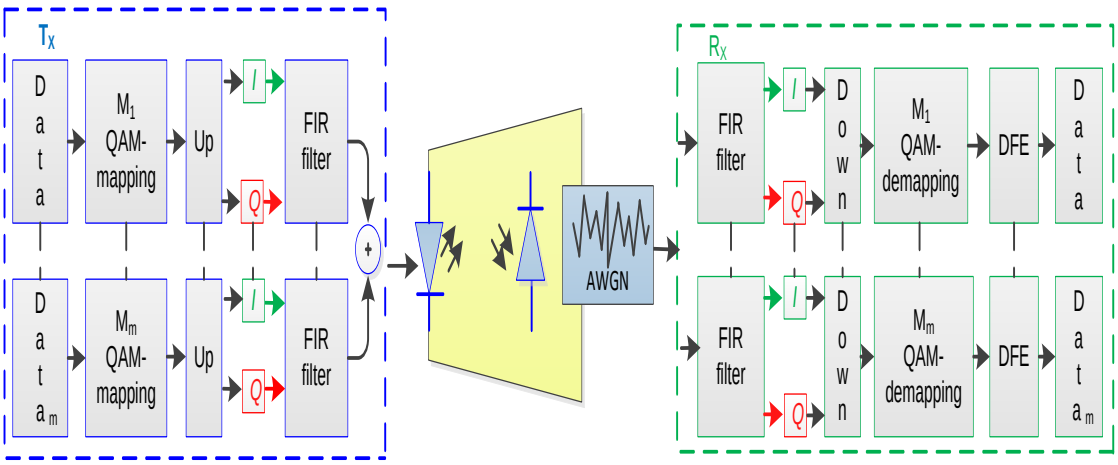

Figure 4.3. A block diagram of the *m*-CAP system [120]

at least twice the highest frequency of the SRRC filter, which in turn has a roll-off factor of β, where $0 \leq \beta \leq 1$. As stated earlier, selecting β appropriately is important because the minimum bandwidth requirement is proportional to $1 + \beta$. However, a larger β provides more protection against ISI. In this work, β is set to 0.15 for consistency with the literature (see Table 4.1) [96].

The transmit FIR in-phase IR ($f_{I,i}(t)$) of the i^{th} sub-carrier is created as a result of convoluting the i^{th} cosine carrier with the SRRC filter IR, as given in Equ. (3.4).

Following the same concept, the quadrature transmit FIR IR ($f_{Qi}(t)$) of the i^{th} sub-carrier is shaped by convoluting the i^{th} sine wave with the SRRC filter IR, as given in (3.5). The resulting transmit waveforms $f_{I,i}(t)$ and $f_{Qi}(t)$ are convoluted with the up-sampled baseband signals $g_{I,i}(t)$ and $g_{Q,i}(t)$ for the m^{th} sub-carriers to form the pre-transmission waveforms, as given in (3.8) and (3.9). The final waveform for transmission ($X(t)$) is found by subtracting the real and imaginary parts of the pre-transmission filters, $X_{I,f,i}(t)$ and $X_{Q\,f,i}(t)$, respectively as in (3.10).

The signal is then used to intensity modulate the LED, which is modelled as an ideal analogue LPF with a cut-off frequency f_{3dB} of 0.5 Hz/Hz, before AWGN is added, as is

consistent with [78]. At the Rx, the signal is split into *I* and *Q* components and passed through the time-reversed in-phase $f_{I,i}(-t)$ and quadrature $f_{Q,i}(-t)$ filters. The data is then down-sampled (‘‘Down’’) and the constellation is de-mapped. DFE is adopted in order to mitigate the effect of ISI, after which a BER measurement in a symbol-by-symbol manner can be done. The principle of DFE is that the ISI introduced by previously detected symbols on currently estimated symbols can be removed using the feedback filter. The output of a DFE can be expressed by [115]:

$$q_m = \sum_{n=0}^{N_1} c_n y_{m-n} - \sum_{n=1}^{N_2} b_n \hat{d}_{m-n}, \tag{4.2}$$

where c_n and b_n are the filter tap coefficients values of the feedforward and feedback filters, respectively. The current symbol is y_{m-n}, and $\hat{d}_{m-n}$ is the estimate of the previous symbol. N_1 and N_2 represent the length of the feedforward and feedback filters, respectively and depending on the performance and complexity trade-off, the optimum filter length can be chosen.

4.4 Results and Discussion

In this section, the performance of *m*-CAP with and without DFE is discussed. 16-QAM is adopted as the modulation format cardinality without any loss of generality, while *m* = {1, 2, 5, 10} as mentioned in the previous section. The occupied sub-carrier bandwidth (B_{sc}) for each value of *m* is B_{sc} = {1, 0.5, 0.2, 0.1} Hz/Hz, respectively. By adopting this scenario, the concept of relaxing the flat channel response by employing the *m*-CAP scheme could be analysed, and the enhancement provided by utilising DFE. In this work, the number of feed-forward and feedback taps of the feed-forward and feedback filters was chosen to be 15 and 10 as shown in Table 4.1, respectively. Depending on the

performance and complexity trade-off, the optimum filter length for each QAM order can be determined [121].

Table 4.1. Parameters of an *m*-CAP system enhanced by DFE

Parameter	Value
Data-NRZ pseudorandom binary sequences length	10^5
LED bandwidth B_{mod}	0.5 Hz/Hz
system bandwidth B_{sys}	1 Hz/Hz
Bit error rate target BER	10^{-4}
Roll-off factor β	0.15
Feed-forward taps	15
Feedback taps	10
Training sequence	1000

In [119], it was reported that the RLS algorithm offers faster convergence speed to a lower error floor compared to the LMS method at the cost of increased computational complexity. Therefore, in this work, the RLS algorithm is adapted in an attempt to show the best equaliser performance. Table 4.1 summarises the utilised system parameters. In this work, the target BER floor is set to be 10^{-4}, which is below the ITU's recommendation of 3.8×10^{-3} [105], and allows a margin for the 7% FEC overhead.

The performance of each *m*-CAP signal is discussed as follows in descending order of system complexity.

4.4.1 **BER Performance of 10-CAP with and without DFE**

Figure 4.4 illustrates the raw 10-CAP BER performance (solid lines). Clearly, a slight power penalty is predicated as a result of increasing the sub-carriers as expected, due to the increase in attenuation from the LPF with increasing frequency. It should be noted that for each increment of *m*-order, two more pulse shaping FIR filters are needed (one for real data and one for imaginary data) at the Tx, and following the same pattern, two

additional FIR filters at the Rx are required as well. As such, for m = 10, 20 FIR filters are needed each at the Tx and the Rx. Therefore, the improvement in the BER performance due to increasing the number of sub-carriers should be considered as a trade-off with system complexity. Deploying an adaptive DFE (dashed lines) does not show any improvement, as Figure 4.4 clearly shows (it should be noted that S denotes the sub-carrier). Furthermore, there is no clear difference when applying DFE due to the reduction in ISI as a result of reducing the individual sub-carrier's bandwidth when increasing the order of m (i.e., m = 10). This is reflected by the constellation diagrams of the 10th sub-carrier (purple plot for the 'with DFE (w/DFE)' case, and black plot for 'without DFE (w/o DFE)' case) at an energy per bit to noise spectral density ratio of E_b/N_0 = 20 dB. The results shown in Figure 4.4 point to an interesting fact that, there is no need to increase the number of sub-carriers beyond m = 10 when combining m-CAP with DFE, as doing so does not add any benefit to the system performance, but additional computational complexity. Moreover, by increasing the m-order the overall system computational complexity is increased, as for each increment in m, two additional pulse

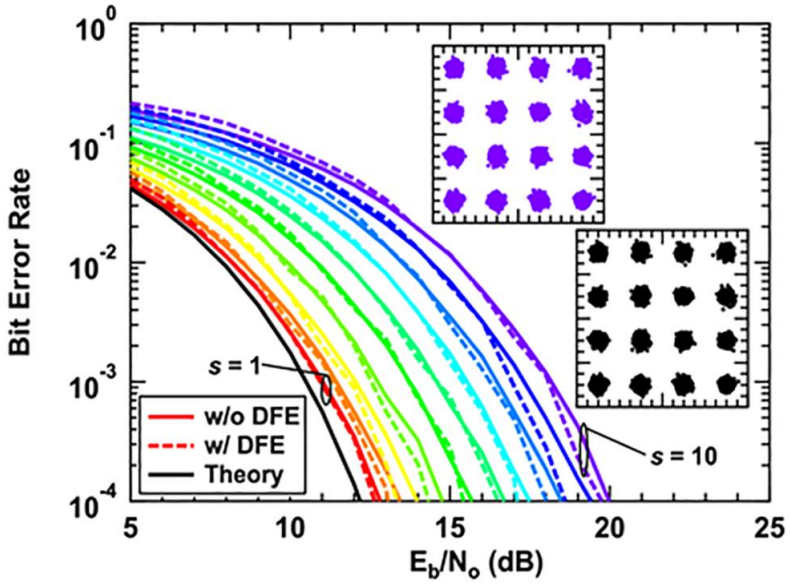

Figure 4.4. BER performance of 16-QAM (theory - black), 10-CAP w/o DFE (solid), and enhanced by DFE (w/ DFE dash) as a function of E_b/N_0. Insets depict the constellation diagrams of the 10th sub-carrier with DFE (w/DFE) (purple) and without DFE (w/o DFE) (black) [120]

shaping FIR filters (i.e., one each for *I* and *Q*) are required at both the Tx and the Rx. Thus, in this work, the maximum number of sub-carriers was set to $m = 10$.

4.4.2 **BER Performance of 5-CAP with and without DFE**

The same performance of 10-CAP can be achieved using the raw 5-CAP system (solid lines in Figure 4.5) in the 1st, 2nd and 3rd sub-carriers. The BER performance approaches the theoretical performance of 16-QAM with a ~4 dB penalty in the worst case (3rd sub-carrier), whereas the 4th and 5th sub-carriers do not converge to the error floor until E_b/N_0 = 19 dB. The 5-CAP system utilising DFE (dashed lines) follows the same pattern as 10-CAP with very little improvement (less than ~1 dB) for all the sub-carriers. This indicates that dividing B_{sys} into smaller sub-carriers reduces the ISI per channel, due to the smaller amount of attenuation per sub-carrier. Figure 4.5 also demonstrates that the use of DFE shows little improvement in the constellation diagrams. In the best case ($S = 4$), ~1 dB is gained when applying DFE.

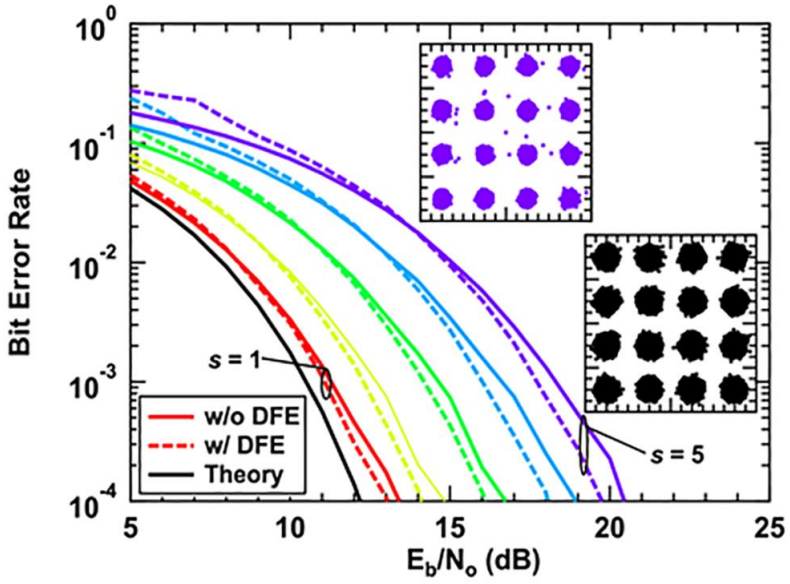

Figure 4.5. BER performance of 16-QAM (theory - black), 5-CAP w/o DFE (solid) and 5-CAP w/ DFE (dash) as a function of E_b/N_0. Insets depict the constellation diagrams of the 5th sub-carrier with DFE (w/DFE) (purple) and without DFE (w/o DFE) (black) [120]

4.4.3 **BER Performance for 2-CAP with and without DFE**

For a raw 2-CAP system (Figure 4.6), the 2nd sub-carrier fails to achieve the BER target, as can be clearly seen from the inset constellation diagram at E_b/N_0 = 20 dB. However, the 1st sub-carrier achieves the designated BER target at E_b/N_0 of ~17.5 dB. For the 2-CAP system with DFE, a noticeable improvement in the BER performance is predicted, where for the 1st sub-carrier, the target BER is attained for E_b/N_0 ~14.5 dB, which represents an additional E_b/N_0 penalty of ~2 dB when compared with the predicted performance of 16-QAM. The 2nd sub-carrier also shows significant improvement, with additional E_b/N_0 penalties of ~5.5 dB and ~7.5 dB compared to the 1st sub-carrier and the predicted theoretical plot, respectively. Furthermore, it can be observed that applying DFE helps the 2nd sub-carrier to reach the BER error floor (i.e., 10^{-4}) at E_b/N_0 = ~20 dB, as reflected in the purple inset constellation diagram (w/ DFE).

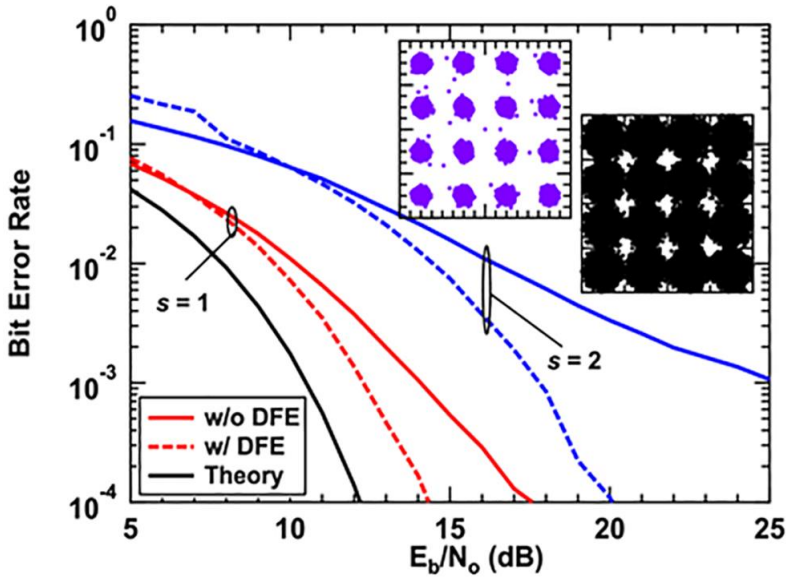

Figure 4.6. BER performance of 16-QAM (theory - black), 2-CAP w/o DFE (solid) and 2-CAP w/ DFE (dash) as a function of E_b/N_0. Insets depict the constellation diagrams of the 2nd sub-carrier with DFE (w/DFE) (purple) and without DFE (w/o DFE) (black) [120]

4.4.4 **BER Performance of 1-CAP with and without DFE**

Figure 4.7 clearly demonstrates that the conventional 1-CAP system experiences a severe ISI as a result of the uneven channel response imposed by the LPF. This is also clearly reflected by the depicted constellation diagram at E_b/N_0 = 20 dB. However, adopting DFE in the 1-CAP system improves the BER performance, meeting the target BER at E_b/N_0 of 19 dB, with a penalty of ~6.5 dB compared to the predicted result (i.e., 16-QAM, theory). Finally, a comparison of the constellation diagram w/o DFE (black) with that w/ DFE (purple) clearly shows a significant improvement when E_b/N_0 = 20 dB.

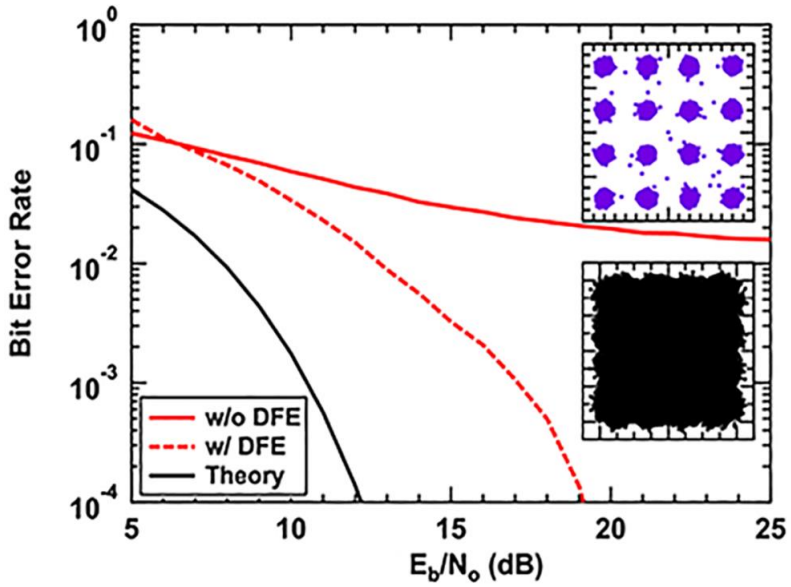

Figure 4.7. BER performance of 16-QAM (theory - black), 1-CAP w/o DFE (solid) and 1-CAP w/ DFE (dash) as a function of E_b/N_0. Insets depict the constellation diagrams of the 1-CAP with DFE (w/DFE) (purple) and without DFE (w/o DFE) (black) [120]

4.5 Evaluation of FIR Pulse Shaping Filter Parameters

FIR pulse shaping filters such as SRRC filters are utilised in *m*-CAP VLC systems to generate the signals for transmission, as explained in Chapter 3 (see section 3.3). FIR filters are considered to represent the most critical part in dictating the overall system performance and complexity, as each increment in the number of sub-carriers is scaled by 2*m* FIR filters (i.e., two FIR filters are needed at the Tx and another two at the Rx for each increment of *m*). Thus, it is worth investigating the trade-off between system performance and complexity if the *m*-CAP scheme is to be adopted in systems such as FPGAs, where there is a limited availability of hardware resources.

There are two key parameters in SRRC filters: *i*) β, and *ii*) L_f (taps/filter). β governs the excess bandwidth of the pulse in the frequency domain and the rate at which the pulse's tails decay (see Figure 3.4(a) and (b)). β has a value in the range of $0 \leq \beta \leq 1$, with $\beta = 0$ offering the narrowest bandwidth (i.e., best utilisation of the bandwidth). In contrast, having $\beta = 1$ results in a wider utilised bandwidth (i.e., a large bandwidth requirement).

The number of taps in a filter L_f is a crucial parameter for both performance and complexity. The lower L_f is the simpler the *m*-CAP system becomes. This parameter plays an especially major role when *m*-CAP is used in a limited hardware resources system (e.g., FPGA). Figure 4.8 illustrates an SRRC filter impulse response with $L_f = 12$ taps when $\beta = 0.1$ and $n_{samp} = 6$ to show the taps and the symbols. L_f (taps/filter) is calculated via $L_f = n_{samp} \times L_s$, where L_s is the number of truncated symbols ($L_s = 2$ symbols for this example).

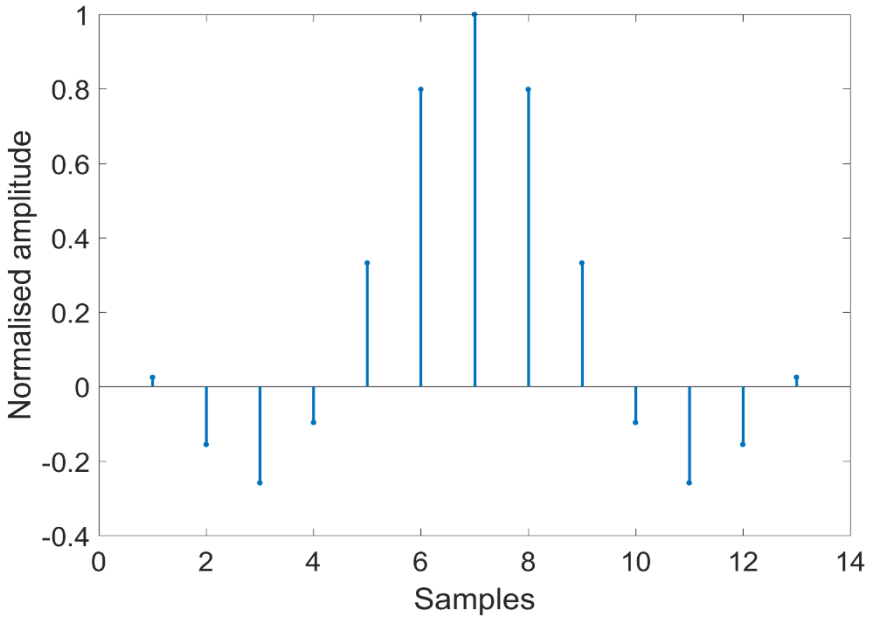

Figure 4.8. An example of an SRRC filter impulse response for L_f = 12 taps

4.5.1 **The Tested *m*-CAP System Model**

The generation of *m*-CAP signals in this numerical simulation is achieved as follows. An *m* independent 10^6 length PRBS was generated before mapping into a 16-QAM cardinality using Gray mapping. The mapped data was subsequently up-sampled by n_{samp} (as described in (3.1)), split into the real *I* and imaginary *Q* components, and then passed through the *I* and *Q* transmit filters ($f_{I,i}(t)$ and $f_{Qi}(t)$), as given in (3.4) and (3.5). The created transmit waveforms $f_{I,i}(t)$ and $f_{Qi}(t)$ were then convoluted with the up-sampled baseband signals *I* $g_{I,i}(t)$ and *Q* $g_{Q,i}(t)$ for all sub-carriers, in order to create the pre-transmission waveforms $X_{I,f,i}(t)$ and $X_{Q,f,i}(t)$, as given in (3.8) and (3.9). The ready for transmission waveform ($X(t)$) was then found by subtracting the real and imaginary parts of the pre-transmission filters, $X_{I,f,i}(t)$ and $X_{Q\,f,i}(t)$, respectively as in (3.10).

As in the previous work (see section 4.3), the output $X(t)$ was then passed through an ideal analogue LPF with a cut-off frequency of f_{3dB} = 0.5 Hz/Hz, and the B_{sig} was set to unity (1 Hz/Hz) without any loss of generality. AWGN was then added as is consistent with [78]. At the Rx, the signal was split into *I* and *Q* components and passed through the time-reversed *I* $f_{I,i}(-t)$ and *Q* $f_{Q,i}(-t)$ filters. The data was then down-sampled by n_{samp}, the constellation was de-mapped and BER calculations were made by comparing the estimated received bits with the transmitted ones.

4.5.2 **Results and Discussions**

In this subsection, an investigation of the *m*-CAP VLC system performance in terms of the measured BER under various FIR filter parameters (i.e., β and L_f (symbols)) is presented. As mentioned earlier, B_{sig} and the LED's B_{mod} were set to 1 Hz/Hz and 0.5 Hz/Hz, respectively. The target BER floor adopted in this work was set to 10^{-4}, as it is well below the ITU's recommendation (i.e., 3.8×10^{-3} for the 7% FEC overhead). The number of sub-carriers was set to m = {2, 5, 10}, and M = 16-QAM as mentioned earlier, without any loss in the generality. Furthermore, in order to investigate the impact of β and L_f (symbols) in these numerical simulations, two different approaches were adopted: *i*) Varying β in the range of β = {0, 0.1, 0.2, 0.3, 0.4, 0.5, 0.6, 0.7, 0.8, 0.9, 1} and fixing the L_f value at 10 symbols; and *ii*) Varying L_f = {2, 4, 6, 8, 10, 12, 14, 16} symbols and fixing the β value at 0.15, for consistency with [45, 96].

4.5.2.1 **The Impact of Varying the Filter Length *L***

Implementing m = 10 for instance, implies the use of 20 FIR filters at the Tx and further 20 FIR filters at the Rx side. Thus, the major source of complexity in the *m*-CAP system is introduced by the number of FIR filters utilised in the system. Therefore, investigating

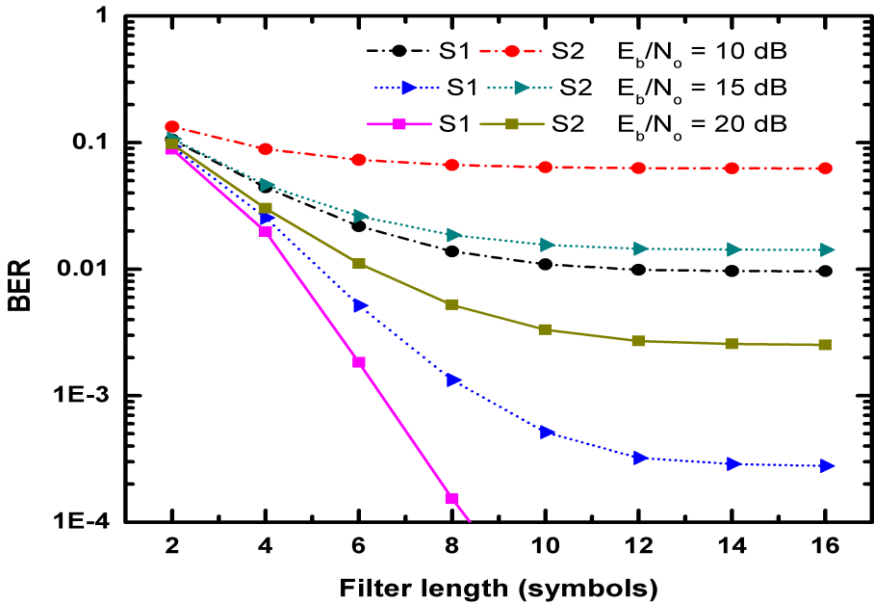

Figure 4.9. BER performance of the 2-CAP system for a range of L_f (symbols). E_b/N_0 = 10 dB (dashed line), E_b/N_0 = 15 dB (dot line) and E_b/N_0 = 20 dB (solid line) were considered

the impact of the number of taps (or L_f) of FIR filters on the BER performance of the *m*-CAP system is crucial. Figure 4.9, Figure 4.10 and Figure 4.11 illustrate the BER performance of the *m*-CAP systems for m = {2, 5, 10}, respectively for a range of L_f = {2, 4, 6, 8, 10, 12, 14, 16} symbols when considering E_b/N_0 = 10 dB (dashed line), E_b/N_0 = 15 dB (dot line), and E_b/N_0 = 20 dB (solid line), and a β value of 0.15.

The results show that increasing L_f for all tested *m*-CAP systems (m = {2, 5, 10}) for the lower value of E_b/N_0 = 10 dB, fails to introduce any significant improvement in the BER performance, as all the sub-carriers fail to achieve the BER target. This is due to the fact that all sub-carriers have low E_b/N_0 values (i.e., 10 dB). Note that, the BER performance is considerably reduced as a result of increasing L_f for the high order sub-carriers. This is caused by the high frequency attenuation affecting the high order sub-carriers as the second sub-carrier is outside the B_{mod} range (i.e., 0.5 Hz/Hz). Moreover, by increasing the E_b/N_0 value to 15 dB and m = 2, both the first and second sub-carriers fail to achieve the

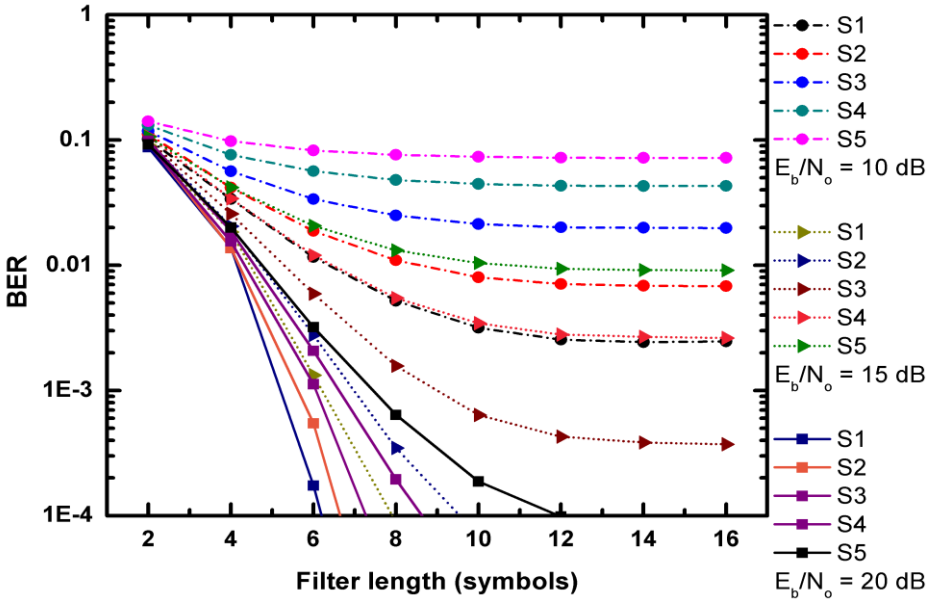

Figure 4.10. BER performance for a range of L_f (symbols) of the 5-CAP system. E_b/N_0 = 10 dB (dashed line), E_b/N_0 = 15 dB (dot line), and E_b/N_0 = 20 dB (solid line) were considered

BER target of 10^{-4}. This confirms that, a certain value of E_b/N_0 must be achieved in order to reach the BER target (10^{-4}) regardless of the filter length utilised.

Considering a higher order of m = 5 and E_b/N_0 = 10 dB, the results show that all sub-carriers fail to hit the BER floor at any given L_f. On the other hand, by increasing the number of sub-carriers to m = 5 and E_b/N_0 = 15 dB, only the first and second sub-carriers (S = 1, 2) convert to the designated BER floor at L_f = 8 and ~10, respectively (see Figure 4.10). This is due to the fact that they have smaller bandwidths that are well within the B_{mod} range.

In addition, by employing the higher E_b/N_0 value of 20 dB and m = 2, the BER target is only met by the first sub-carrier (S = 1) at L_f = ~8 symbols. However, increasing L_f fails to converge the second sub-carrier to the BER floor at any given value (see Figure 4.9). This is due to having a wider bandwidth that is outside the B_{mod} range. Considering the m = 5 (Figure 4.10) and m = 10 (Figure 4.11) systems for E_b/N_0 = 20 dB show that the BER target is met by all sub-carriers. It should be noted that the highest value of L_f to achieve

the BER target is L_f = 12 symbols. This is significant as it shows that for high *m*-CAP orders (i.e., $m \geq 5$), employing an FIR filter with an $L_f > 12$ symbols is impractical, as there will be no additional improvement in the BER performance, but rather an extra complexity added to the system.

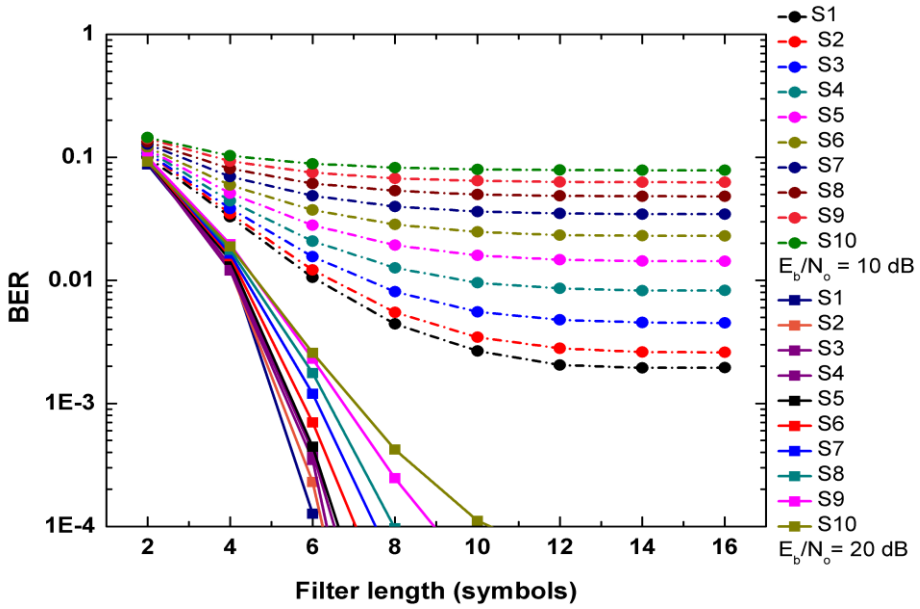

Figure 4.11. BER performance of the 10-CAP system for a range of L_f (symbols). E_b/N_0 = 10 dB (dashed line) and E_b/N_0 = 20 dB (solid line) were considered

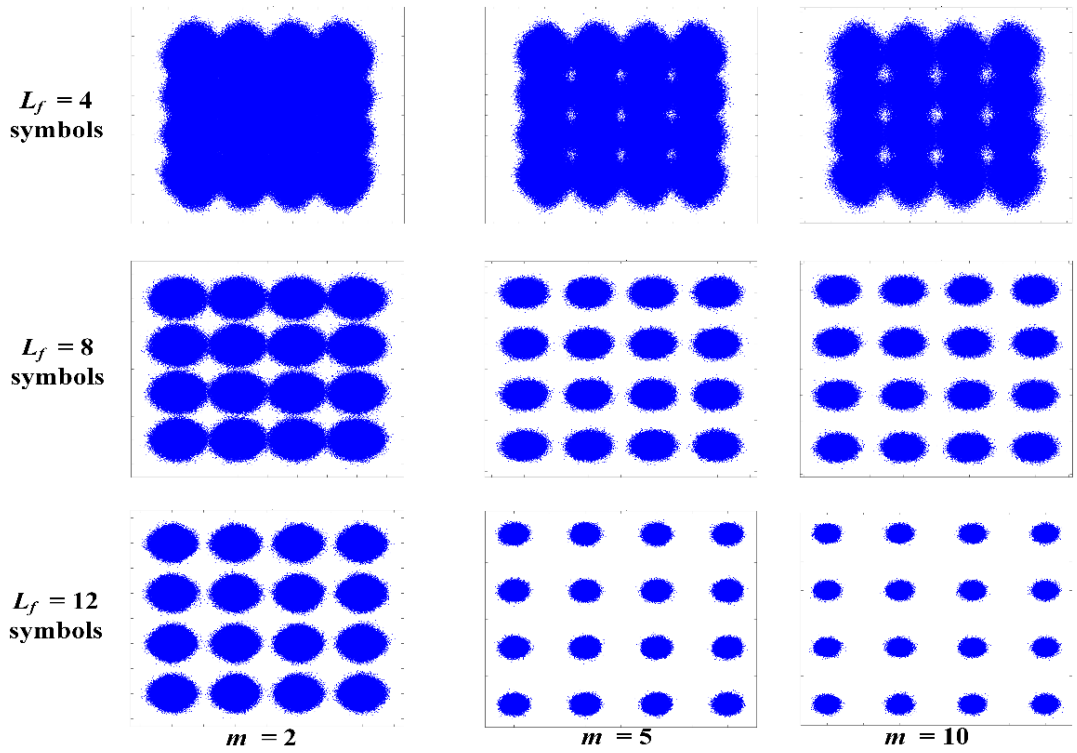

Figure 4.12. The received constellation diagrams of the first sub-carrier (S = 1) for a set of m = {2, 5, 10} and L_f = {4, 8, 12}symbols values at E_b/N_0 = 20 dB

Finally, it should be noted that the high order sub-carriers m = 5 (S = 4, 5) and m = 10 (S = 6, 7, 8, 9, 10) converge to the BER floor at the cost of higher $L_f \geq 7$ symbols, due to being outside the range of B_{mod}. The received constellation diagrams of the first sub-carrier of each m = {2, 5, 10} for L_f = {4, 8, 12} symbols are depicted in Figure 4.12, and further illustrates the impact of increasing L_f on the system performance.

4.5.2.2 Varying the Roll-off Factor β for a Fixed Filter Length L_f

As mentioned earlier (see section 4. 5), β plays a crucial role in governing the excess bandwidth of the FIR filter. The closer β approaches zero, the closer the pulse approximates to a rect (.) function in the frequency domain, which makes the utilisation of the bandwidth more efficient. Thus, utilising lower values of β implies a save in the bandwidth of the employed system. On the other hand, approaching the highest value of β (i.e., β = 1) leads to a wider utilised bandwidth, as B_{tot} implies a (1 + β) larger bandwidth requirement, and thus, an insufficient bandwidth utilisation.

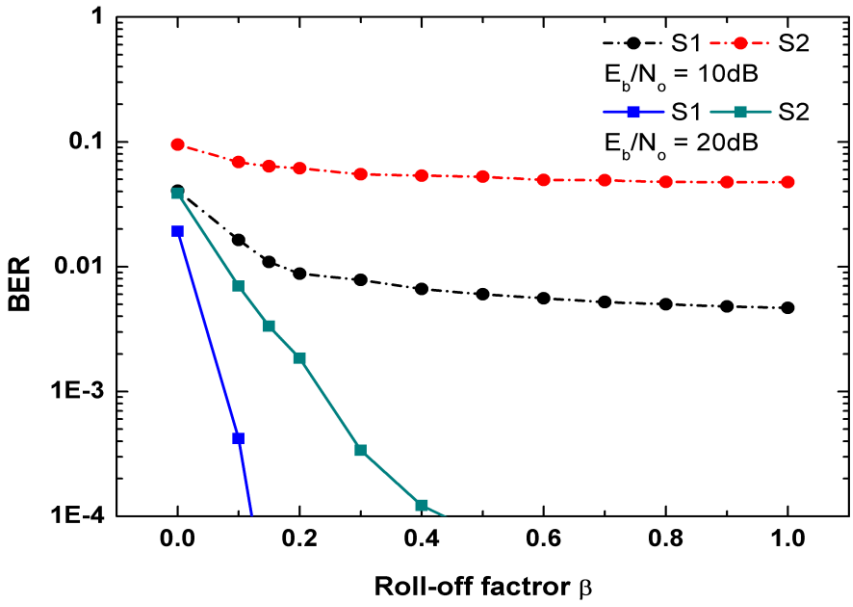

Figure 4.13. BER performance of the 2-CAP system for a range of β values and a fixed L_f value of 10 symbols. E_b/N_0 = 10 dB (dashed line) and E_b/N_0 = 20 dB (solid line) were considered

Figure 4.13, Figure 4.14 and Figure 4.15 show the BER performance for m = {2, 5, 10}, respectively for β = {0, 0.1, 0.2, 0.3, 0.4, 0.5, 0.6, 0.7, 0.8, 0.9, 1} when considering E_b/N_0 = 10 dB (solid line) and E_b/N_0 = 20 dB (dashed line) and L_f = 10 symbols. The results show that all tested m-CAP systems (i.e., m = {2, 5, 10}) fail to hit the BER floor target at any given value of β in the E_b/N_0 = 10 dB case. This indicates that at low SNRs, increasing β introduces negligible improvement in the BER performance.

Considering the higher SNR value (E_b/N_0 = 20 dB) and m = 2 (see Figure 4.13), the first sub-carrier (S = 1) manages to hit the BER floor at β > 0.1, while for S = 2, the BER floor is met at β > 0.4. This is a remarkable improvement especially for the S = 2 case, although the price to pay here is more excess bandwidth. For the 5-CAP and 10-CAP systems (Figure 4.14 and Figure 4.15, respectively), through only a slight increase in the value of β of ~0.2, all sub-carriers achieve the BER target at β < 0.2 when considering E_b/N_0 = 20 dB. This is a significant improvement when compared to the E_b/N_0 = 10 dB case, although it is achieved at the cost of extra excess bandwidth. This is further reflected by the received constellation diagrams of the first sub-carrier (S = 1) depicted in Figure 4.16 for

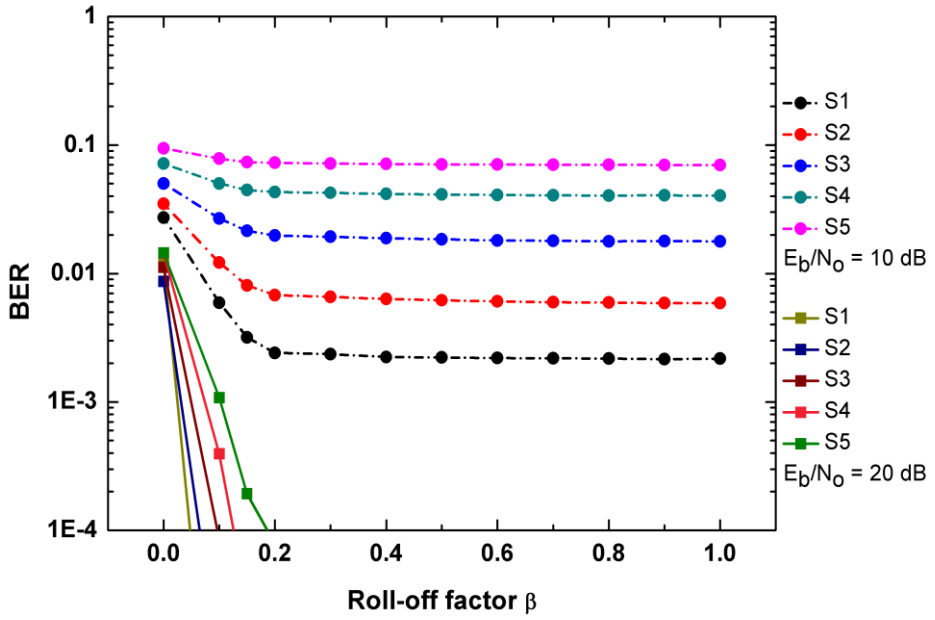

Figure 4.14. BER performance of the 5-CAP system for a range of β values and L_f = 10 symbols.E_b/N_0 = 10 dB (dashed line) and E_b/N_0 = 20 dB (solid line) were considered

each m = {2, 5, 10} and β = {0.1, 0.5, 1} value. The constellations show that increasing both β and the m-CAP order further improves the system performance.

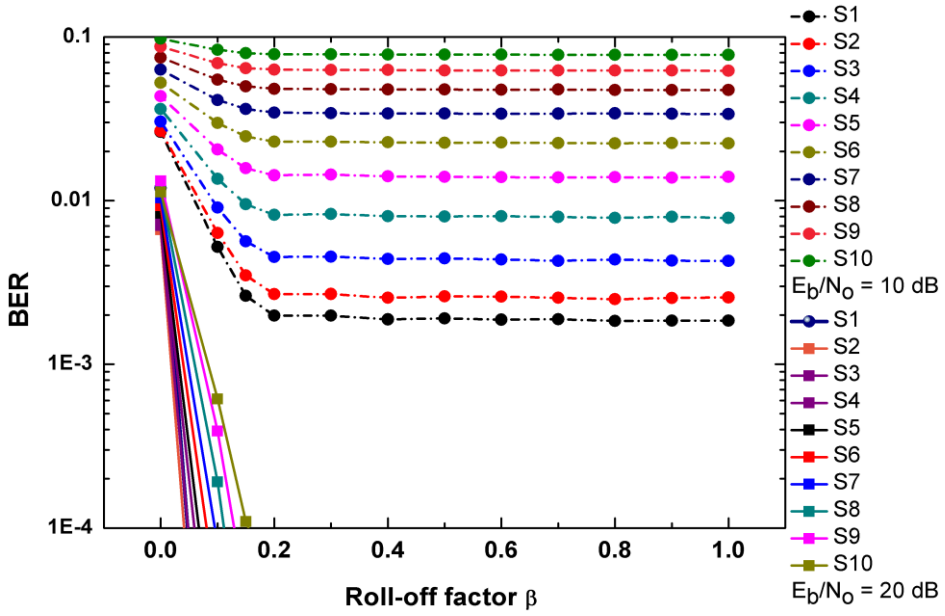

Figure 4.15. BER performance of the 10-CAP system for a range of β values and L_f = 10 symbols. E_b/N_0 = 10 dB (dashed line) and E_b/N_0 = 20 dB (solid line) were considered

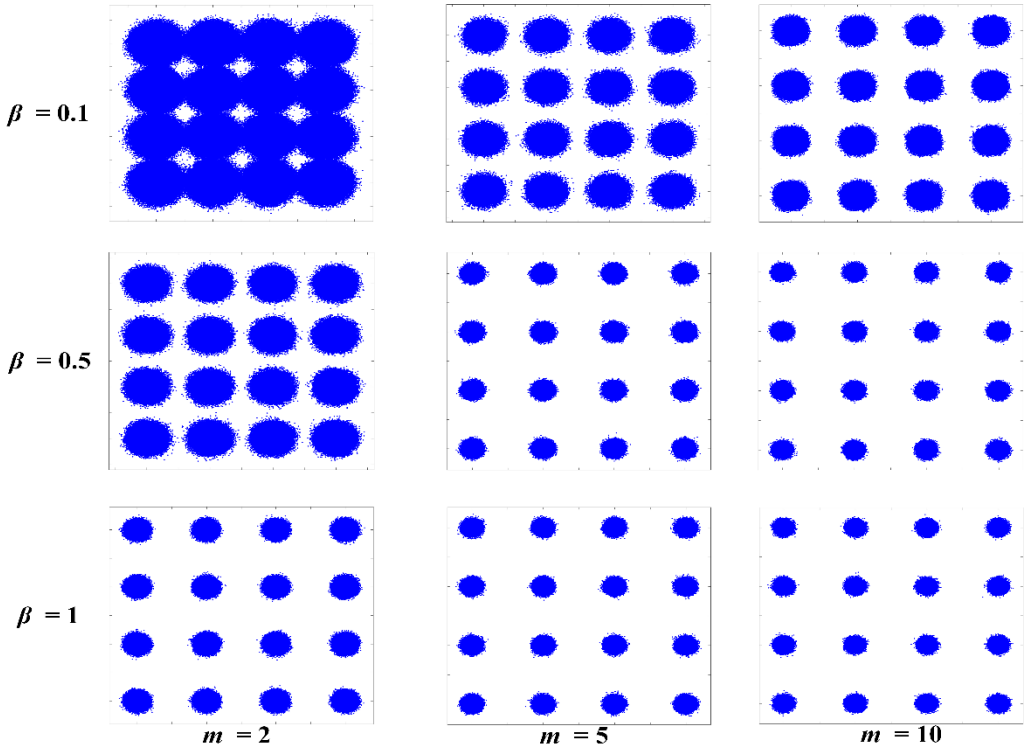

Figure 4.16. The received constellation diagrams of the first sub-carrier (S = 1) for a set of m = {2, 5, 10} and roll off factor β = {0.1, 0.5 ,1} values at E_b/N_0 = 20 dB

4.6 *m*-CAP VLC System Performance with Different Pulse Shaping Filters Parameters

In the previous section (section 4. 5), the impact of the pulse shaping filter parameters β and L_f on the BER performance of the *m*-CAP VLC system was discussed. Increasing both parameters is predicted to lead to a better BER performance at the cost of extra excess bandwidth and additional filter length (complexity). The latter is considered to be the major impediment facing the implementation of the *m*-CAP scheme in real time systems such as FPGAs, due to the limited hardware resources. In this section, a further look at the impact of the pulse shaping filter parameters L_f and β is provided. Furthermore, a better understanding of the physical performance of the *m*-CAP system is obtained by experimentally investigating the performance of the *m*-CAP VLC system utilising different ranges of β and L_f for a set of *m* values and showing the influence of such parameters on the measured data rates and spectral efficiencies.

4.6.1 Experimental System Model

Figure 4.17 depicts the block diagram of the proposed *m*-CAP VLC system under test, showing both the experimental setup (bottom) and the generation and recovery of the *m*-CAP signals in MATLAB (top). First, a PRBS ("D_m") with a length of 2^{15}-1 was generated for each sub-carrier before mapping into *M*-QAM constellation symbols ($x_{QAM}(t)$) using the Gray mapping code. The mapped data $x_{QAM}(t)$, was then up-sampled (''Up'') by means of inserting zeros (zero padding) between consecutive symbols according to the number of samples/symbol n_{samp}, as given by [45, 96]:

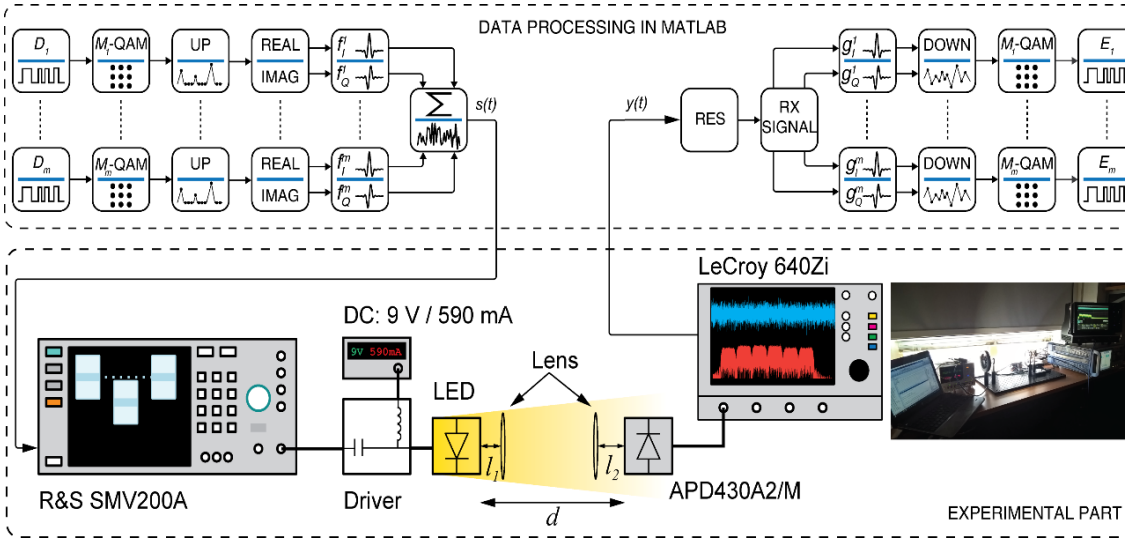

Figure 4.17. Block diagram of the *m*-CAP VLC system under test. Inset: a photograph of the setup [122]

$$n_{samp} = 2.\ \lceil 2m(1+\beta) \rceil, \tag{4.3}$$

where $\lceil \cdot \rceil$ denotes the ceiling function. The up-sampled $x_{QAM}(t)$ symbols were then split into *I* and *Q* symbols of the i^{th} sub-carrier prior to being passed through the in-phase $f_{I,i}(t)$ and quadrature $f_{Q,i}(t)$ SRRC transmit filters, whose impulse responses form a Hilbert pairs, as given in (3.4) and (3.5).

The output *m*-CAP signal ($s(t)$) was created by subtracting the real and imaginary parts of the pre-transmission filters, $X_{I,f,i}(t)$ and $X_{Q,f,i}(t)$, respectively as given in Equ. (3.10).

The pre-transmission waveforms $X_{I,f,i}(t)$ and $X_{Q\,f,i}(t)$ were generated by convoluting the *I* and *Q* up-sampled symbols of the i^{th} sub-carrier with the transmit waveforms $f_{I,i}(t)$ and $f_{Q,i}(t)$, as in (3.8) and (3.9). The output signal $s(t)$ was then loaded into a vector signal generator (Rohde & Schwarz SMV200A (max sampling rate 200 MS/s)), that in turn passed the transmitted signal to a custom-built driving circuit in order to intensity modulate the LED. The utilised LED in this work was the commercially available OSRAM Golden Dragon, which has a B_{mod} of 1.2 MHz and was biased at ~590 mA in order to ensure operating in the linear region. Figure 4.18 illustrates the frequency

response of the used LED, showing the LED's B_{mod} of 1.2 MHz. For this particular experimental setup, and due to the signal distortion caused in the very low frequency region (no-flat region), it was decided that it was more beneficial to shift the signal in the frequency domain by 0.2 MHz. Thus, a 0.2 MHz cut in frequency region was implemented (denoted by the red colour as "unused region"). B_{sig} was set in this work to 1 MHz and 2 MHz in order to ensure optimal system performance during measurements even for high values of β, as by varying β from 0 to 1 the signal bandwidth requirements vary in accordance with $B_{tot} = B_{sig} . (1+ \beta)$. Thus, the maximum B_{tot} was 4.2 MHz, which is ~4 times larger than the minimum B_{tot} of 1.2 MHz (see Figure 4.18).

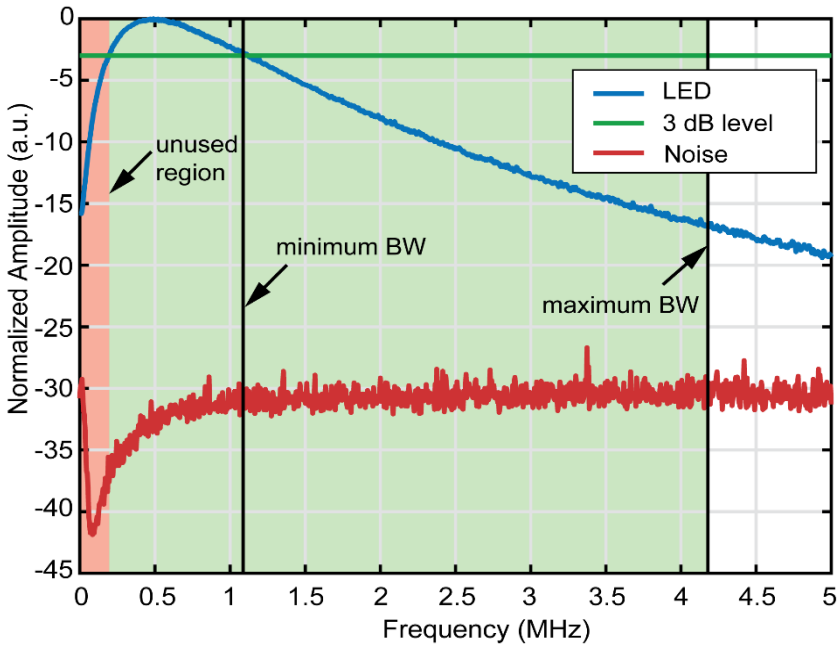

Figure 4.18. The frequency response of the LED under test. Also depicted are the unused low frequency region (red), the minimum and maximum total signal bandwidths and the noise floor [122]

Table 4.2 summarises the parameters of the experimental setup, the utilised LED and the silicon APD (Thorlabs APD430A2/M). The intensity modulated signal was then propagated through a transmission distance (d) of 1 m length. As shown in the experimental setup of Figure 4.17, two biconvex lenses with a diameter of 25.4 mm were utilised in order to collect and focus the light beam. The two lenses were placed at

distances of l_1 = 0.25 m and l_2 = 0.35 m from the LED and the APD, respectively. At the Rx side, the regenerated signal, which is defined in (2.3), $y(t)$ was digitised and saved using a digital storage oscilloscope (LeCroy WaveRunner Z640i) with a sampling rate of 2 GS/s for further off-line processing in MATLAB. The off-line process started by first resampling ("RES") the signal $y(t)$ in order to match the sampling rate of the reference version $s(t)$, and then passing it through the in-phase and quadrature time-reversed pulse shaping filters for the i^{th} sub-carriers, $g_I^i(t) = f_I^i(-t)$ and $g_Q^i(t) = f_Q^i(-t)$, respectively.

Table 4.2. Setup, LED and APD parameters

Parameter	**Value**
Pseudorandom binary sequences length	2^{15}-1
LED - OSRAM Golden Dragon	
• LED bandwidth B_{mod}	1.2 MHz
• LED beam angle	170°
LED's Biconvex lens	
• Diameter	25.4 mm
Total signal bandwidth B_{tot}	1.1 MHz & 4.2 MHz
Transmission span L	1 m
Silicon APD430A2/M	
• Active area diameter	0.2 mm
• Responsivity $\mathcal{R}$ max	25 A/W
• Bandwidth	400 MHz
• Transimpedance gain	5 kV/A
APD's Convex lens	
• Diameter	25.4 mm

The baseband split signals representing the *I* and Q components were then down-sampled by removing the n_{samp} added zeros (''Down''), and the *M*-QAM symbols were subsequently de-mapped. Finally, the estimated version of the data ("E_m") was recovered and the BER per sub-carrier was determined by comparing the estimated version of the received bits E_m, and the transmitted bits D_m, and the link BER was subsequently determined by aggregating the BER values of all sub-carriers. In order to maximise the system performance, a bit-loading technique was applied as follows. In the first instance,

a BPSK pilot signal was transmitted to measure the EVM for each individual sub-carrier, prior to estimating the SNR via $\mathrm{SNR} = 20 \cdot \log_{10}(\mathrm{EVM}_{RMS})$. Next, each sub-carrier was loaded with a specific value of b = {1, 2, 3, 4, 5, 6, 7, 8, 9} based on the estimated SNR, which was compared with the theoretical SNR threshold ($\mathrm{SNR}_{\mathrm{thresholds}}$) obtained from [113], where $\mathrm{SNR}_{\mathrm{thresholds}}$ = {6.8, 9.8, 14.4, 16.6, 20.6, 22.6, 26.5, 28.5, 32.3} dB for the afortmentioned values of b, respectively. The $\mathrm{SNR}_{\mathrm{thresholds}}$ were chosen according to the required BER target, which was set to 10^{-3} in this work to leave a margin for the ITU's 7% FEC limit and to be consistent with the previous work [45, 120]. Figure 4.19 illustrates an example of the measured SNR against the number of sub-carrier for m = {2, 4, 6, 8, 10}, L_s = 10 and β = 0.2 and for a range of M-QAM. Also depicted in the figure as dash lines are the $\mathrm{SNR}_{\mathrm{thresholds}}$ levels for different M-QAM orders.

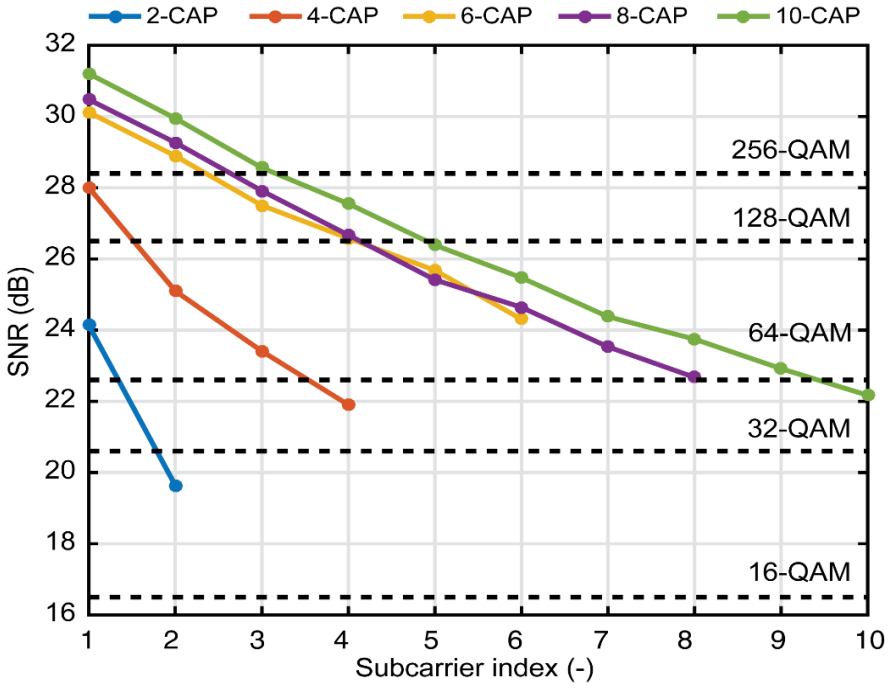

Figure 4.19. An example of the measured SNR per sub-carrier from the BPSK pilots against the number of sub-carriers for a range of m = {2, 4, 6, 8, 10}, L_s = 10 and β = 0.2. The theoretical $\mathrm{SNR}_{thresholds}$ (dash line) are also depicted in the figure

4.6.2 **Results and Discussion**

As previously mentioned, the aim of this work is to further demonstrate the influence of the pulse shaping filter parameters (i.e., L_f and β) on the *m*-CAP VLC system performance (in terms of the measured data throughputs and spectral efficiencies). The pulse shaping filter length (taps/filter) represents the major impediment towards implementing the *m*-CAP technique in real time systems (e.g., FPGA). In this work, L_f is governed by three parameters: (*i*) β = {0.1, 0.2, 0.3, 0.4, 0.5, 0.6, 0.7, 0.8, 0.9, 1}; (*ii*) L_s = {2, 4, 6, 8, 10}, and (*iii*) m = {2, 4, 6, 8, 10}. The highest value of L_s (i.e., L_s = 10) was chosen in this work because, as shown in the previous numerical simulations (see section 4.5), utilising $L_s > 12$ is impractical as it introduces extra complexity to the system with no improvement in the BER performance. Furthermore, it was shown that by utilising $L_s = 12$, only a slight improvement is predicted in contrast to utilising $L_s = 10$, while the complexity is markedly increased. Thus, L_s = 10 was chosen in this work as the maximum value. It should be noted that, in the described sets of results below, B_{sig} was set to 1 MHz unless otherwise stated, and the aggregate data rate was achieved as the sum of each individual sub-carrier's data rate R_b. The proposed system performance was then assessed by discussing the results of the measured R_b, the spectral efficiency η_s and the L_f (taps/filter) as a function of the aforementioned values of L_s, β and m.

The performance of each *m*-CAP-VLC link is discussed below in ascending order from 2-CAP to the highest order (i.e., 10-CAP). Note that, a discussion of the results for m = 4 will be omitted due to achieving similar results to the m = 6 case.

4.6.2.1 **2-CAP System**

Figure 4.20(a), (b) and (c) illustrate the achieved R_b, η_s and the appropriate L_f for a range of β = {0.1, 0.2, 0.3, 0.4, 0.5, 0.6, 0.7, 0.8, 0.9, 1}, respectively. As it can be observed from Figure 4.20(a), both L_s and β had the same effect on the achieved R_b, as the measured R_b was significantly increased from 1 Mb/s to 6.5 Mb/s (the highest R_b for 2-CAP link, denoted by a red dot) by increasing both L_s and β. However, Figure 4.20(b) shows that the impact of varying L_s and β was different on the achieved η_s, where the increase in η_s was low and remained almost fixed for lower values of L_s (i.e., L_s = 2 and L_s = 4) over the entire range of β. On the other hand, utilising L_s > 4 led to a much more significant impact of β, resulting in a rapid increase in η_s of up to 4.23 b/s/Hz (the highest η_s for 2-CAP link, denoted by a red point) at β = 0.3 and L_s = 10 (see Figure 4.20(b)). This is as a result of having a higher bandwidth per sub-carrier (higher than β = 0.1 and β = 0.2), without being significantly affected by the attenuation outside of the LED's B_{mod}. For β > 0.4 and for L_s values of 8 and 10, it can be observed that the measured η_s was degraded. This is attributed to the fact that the individual sub-carrier bandwidth increased by increasing β and became more prone to the attenuation outside the LED's B_{mod}.

Furthermore, as the bandwidth per sub-carrier increased, the approximation of each sub-carrier to flat band became less representative. It should be noted from Figure 4.20(a) and (b) that there is a trade-off between the achieved R_b and η_s when implementing a 2-CAP link, which is considered to be a substantial drawback when compared to high order *m*-CAP links.

Figure 4.20(c) shows the length of filters L_f (taps/filter) as a function of β = {0.1, 0.2, 0.3, 0.4, 0.5, 0.6, 0.7, 0.8, 0.9, 1} for a range of L_s = {2, 4, 6, 8, 10}. Furthermore, the insets depict the constellation diagrams of the S = 1 and S = 2 sub-carriers for the best bandwidth utilisation case of the 2-CAP link (β = 0.3, and L_s = 10) with L_f = 120 taps/filter. It can be

observed form Figure 4.20(c) that increasing β and L_s led to an increase in L_f, which in turn led to increasing the overall system complexity. Furthermore, a more rapid increase in L_f occurred as a result of the increase in L_s for a constant value of β, reaching up to ~5 times more taps for $\beta = 1$. On the other hand, a maximum increase in the complexity of L_f of ~ 60 taps occurred for $L_s = 10$ over the entire range of β. Note that, for all values of L_s, the individual curves remained constant over the range of $\beta = 0.3$ 0.4 and 0.5, which indicates that increasing β does not always lead to increasing the length of the filter. This fact is significant as it can be adopted to avoid the high computational complexity, which is desirable in the resources-limited real time systems.

Furthermore, this is an unexpected advantage of the 2-CAP system over high order *m*-CAP systems, as will be shown in the next subsections. In addition, the discussion to follow will also show that it is possible to optimise the high order *m*-CAP links ($m \geq 6$ in this work) to achieve both the highest R_b and η_s by utilising the same FIR pulse shaping filter parameters (i.e., the given values of β and L_s).

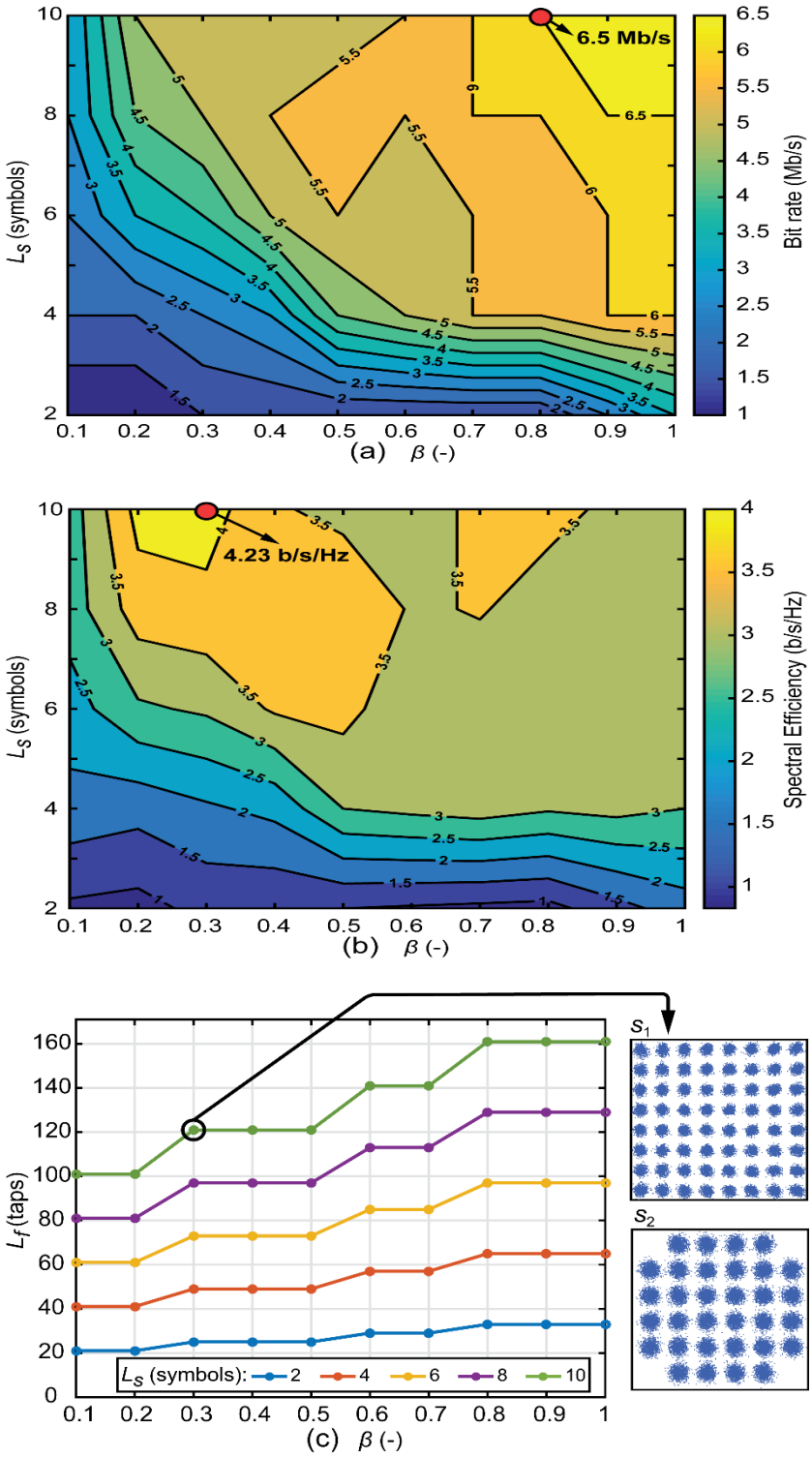

Figure 4.20. The 2-CAP system's (a) data rate as a function of L_s and β, (b) spectral efficiency as a function of L_s and β, and (c) filter length as a function of β. The insets show the constellation diagrams for the sub-carriers $S = 1$ and $S = 2$ for $\beta = 0.3$ and $L_s = 10$ [122]

4.6.2.2 **6-CAP System**

The measured R_b, η_s and the corresponding L_f as a function of β = {0.1, 0.2, 0.3, 0.4, 0.5, 0.6, 0.7, 0.8, 0.9, 1} for the 6-CAP system are illustrated in Figure 4.21 (a), (b) and (c), respectively. Unsurprisingly, as in the previous case (i.e., 2-CAP system), both L_s and β had the same effect on the achieved R_b. However, in order to achieve R_b > 6.5 Mb/s, values of $\beta \geq 0.6$ and $L_s \geq 4$ should be considered, thus allowing an additional degree of freedom in the system design in contrast to the 2-CAP link. As denoted by the red dot in Figure 4.21, the highest R_b of 7 Mb/s was achieved for β = 0.3 and L_s = 10. Increasing β did not introduce a significant improvement in the data throughput, as R_b remained within the range of 6.5 to 7 Mb/s. Note that the effect of β is noticeable for $L_s \geq 4$, as at first R_b rapidly increased to > 6.5 Mb/s for L_s = {4, 6, 8, 10} and the corresponding β = {0.6, 0.4, 0.3, 0.2} values. However, for $L_s \leq 4$, a slight decrease in R_b was observed for β > 0.6.

As expected, increasing both L_s and β had the same effect on the measured η_s as in the 2-CAP system. However, the effect of both parameters was more significant, as higher η_s values were achieved. The highest measured η_s of 5.83 b/s/Hz was achieved for β = 0.2 and L_s = 10 (denoted by a red point in Figure 4.21(b)). It should be noted that increasing both parameters above certain values (e.g., β > 0.5 and L_s > 6) resulted in a degradation in the η_s values. This is due to the higher bandwidth of the individual sub-carriers, which made them more prone to the attenuation outside the LED's B_{mod}. Figure 4.21(c) illustrates the corresponding L_f as a function of β = {0.1, 0.2, 0.3, 0.4, 0.5, 0.6, 0.7, 0.8, 0.9, 1} for a range of L_s = {2, 4, 6, 8, 10}. The insets of Figure 4.21(c) depict the constellation diagrams of the S = 1 and S = 3 sub-carriers for the most bandwidth efficient case of the 6-CAP link (i.e., β = 0.2, and L_s = 10) with the appropriate value of L_f of 300 taps/filter. It is clear from Figure 4.21(c) that L_f increased by increasing β and L_s. For example, when L_s was changed from 2 to 10 and for β = 1, L_f increased by more than 4

times. Note that, the 6-CAP link can be designed to achieve the highest R_b and η_s by considering a single system setup (i.e., β = 0.3 and L_s = 10).

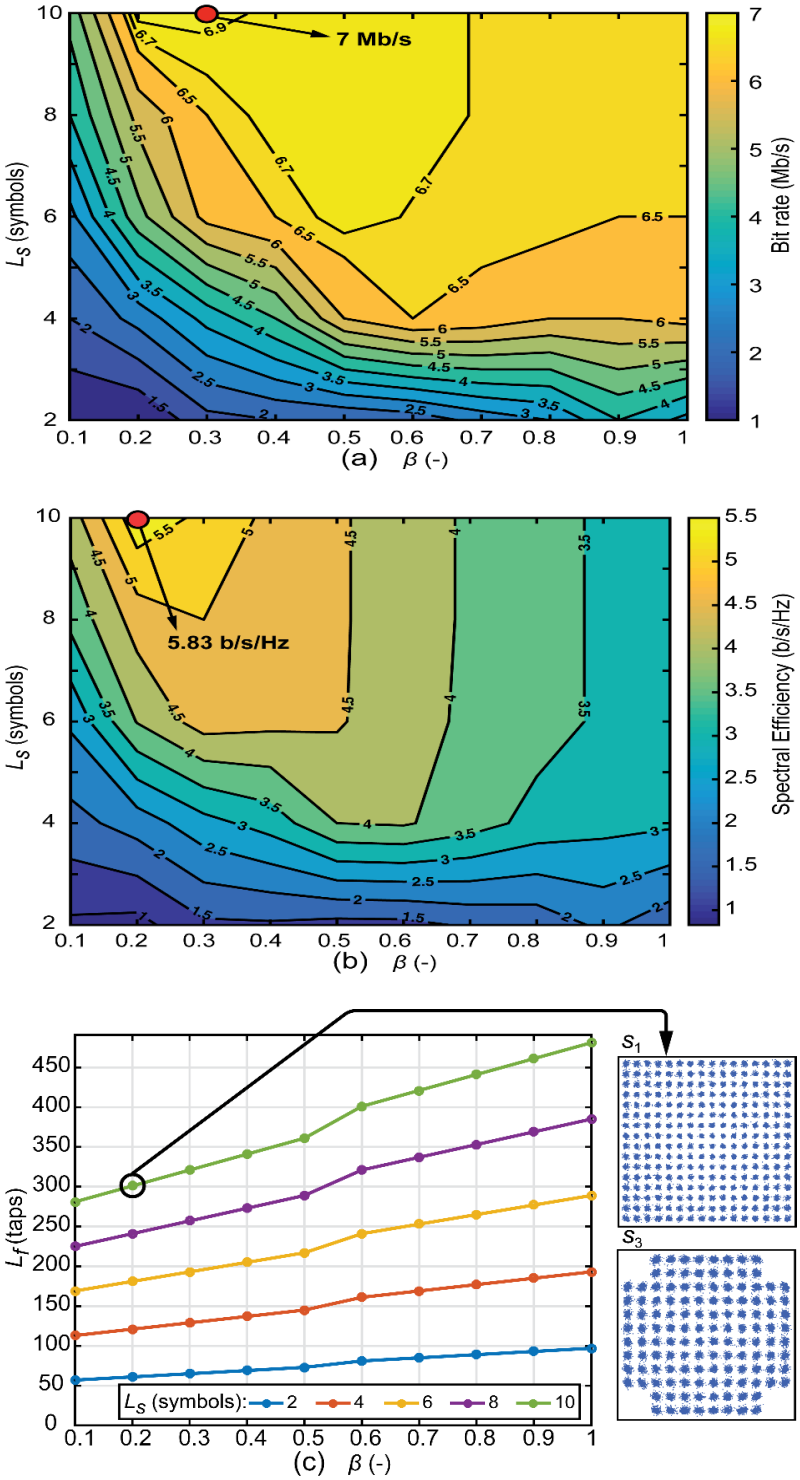

Figure 4.21. The 6-CAP system's (a) data rate as a function of L_s and β, (b) spectral efficiency as a function of L_s and β, and (c) filter length as a function of β. The insets show the constellation diagrams for the sub-carriers S = 1 and S = 3 for β = 0.2 and L_s = 10 [122]

For a further insight on the 6-CAP system performance, B_{sig} was changed to 2 MHz and the achieved R_b and η_s were measured and are illustrated in Figure 4.22(a) and (b), respectively. In contrast to the case where B_{sig} = 1 MHz, it is clear that a higher R_b and lower η_s were achieved for the β values of $0.3 < \beta < 0.6$ and $0.2 < \beta < 0.4$, respectively. Moreover, the highest R_b value of 11.33 Mb/s and η_s of 4.31b/s/Hz were obtained for the same L_s value of 10 but different values of β of 0.4 and 0.2, respectively. It should be noted that by changing B_{sig} to 2MHz, an improvement of ~62% in the highest value of R_b was achieved. However, a decrease of ~26% was attained in the achieved η_s, which is attributed to the higher bandwidth for each individual sub-carrier, making the out of LED's B_{mod} sub-carriers more prone to attenuation.

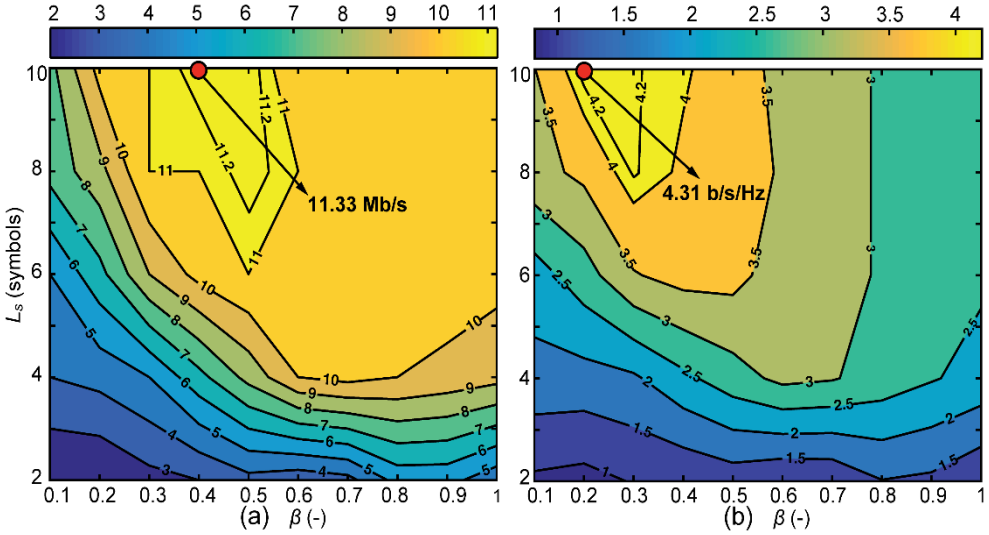

Figure 4.22. The 6-CAP system's (a) data rate as a function of L_s and β, and (b) spectral efficiency as a function of L_s and β for B_{sig} = 2 MHz [122]

4.6.2.3 **8-CAP System**

As depicted in Figure 4.23(a) and (b), the 8-CAP system performance was similar to that of the 6-CAP link, as the highest R_b and η_s values achieved were 7.14 Mb/s and 5.94 b/s/Hz (denoted as red points) for β = 0.2 and L_s = 10. It can be observed that a value of R_b > 6.5 Mb/s was achieved in two different regions. This is due to the optimal sub-carrier allocation within the LED's B_{mod}.

On the other hand, η_s was degraded for β = {0.7, 0.8, 0.9} compared to lower β values (refer to Figure 4.23(b)). Figure 4.23(c) plots L_f as function of L_s and β as well as the received constellation diagrams of the S = 1 and S = 4 sub-carriers for the best performing case of the 8-CAP link (i.e., β = 0.2, and L_s = 10) with a single filter requires taps/filter L_f = 401. Such a considerably high L_f value contributed to increasing the overall system complexity compared with the 6-CAP link achieving almost the same system performance (i.e., R_b and η_s).

Furthermore, for the same 8-CAP link, the computational complexity could be reduced by ~31%, by reducing L_f from 337 taps/filter for L_s = 8 and β = 0.3 to L_f = 233 taps/filter for L_s = 4 and β = 0.8 (see Figure 4.23(a) and (c)). This however also corresponds to a reduction in η_s by 30% from 5 b/s/Hz to 3.5 b/s/Hz (refer to Figure 4.23(b)).

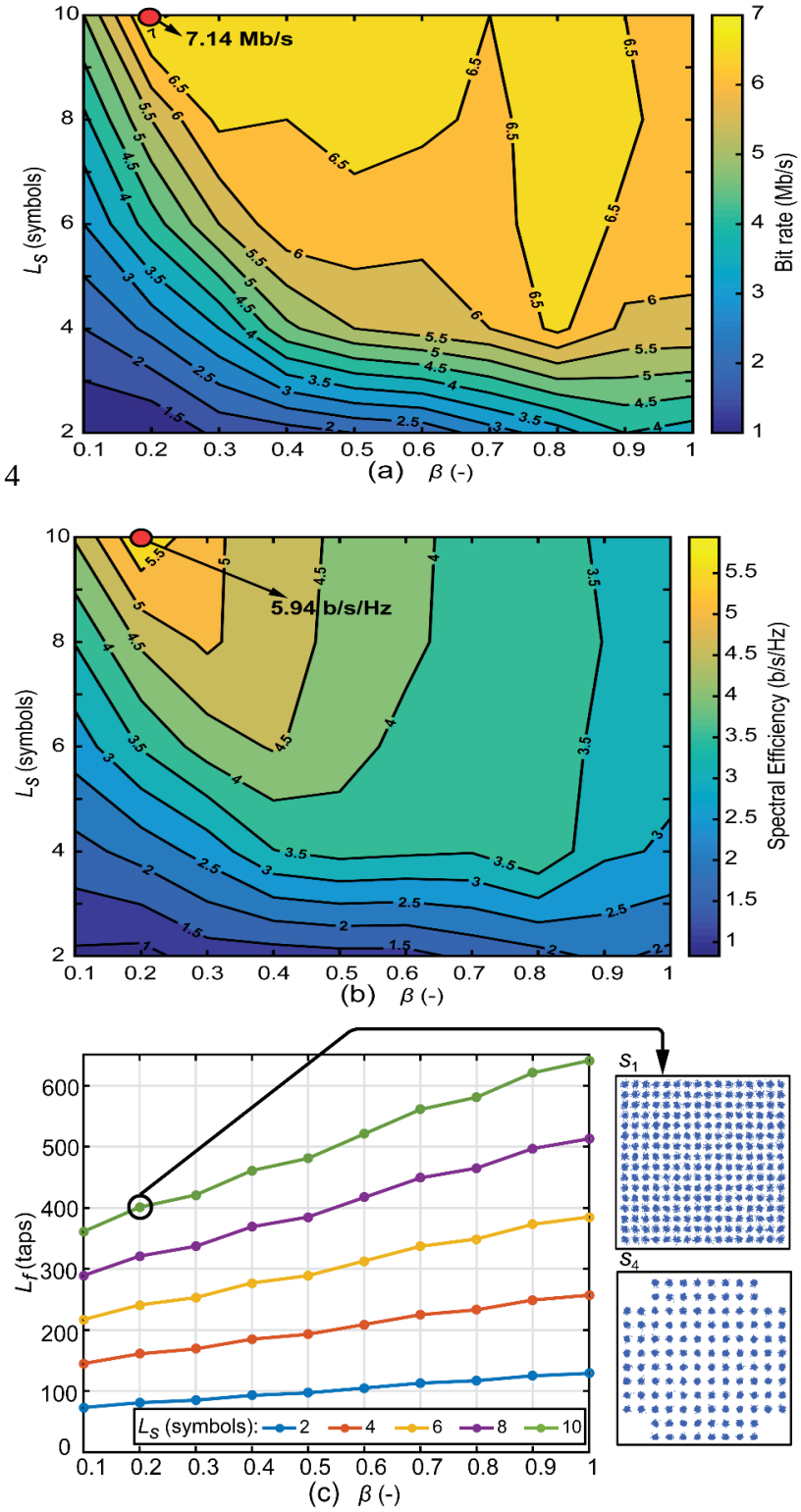

Figure 4.23. The 8-CAP system's (a) data rate as a function of L_s and β, (b) spectral efficiency as a function of L_s and β, and (c) filter length as a function of β. The insets show the received constellation diagrams for the sub-carriers $S = 1$ and $S = 4$ for $\beta = 0.2$ and $L_s = 10$ [122]

4.6.2.4 **10-CAP System**

The measured R_b and η_s of the 10-CAP system are depicted in Figure 4.24(a) and (b), respectively. It can be observed that R_b values > 6.5 Mb/s were achieved in two different regions (β = 0.2 and 0.6), which is attributed once again to the optimal sub-carrier allocation within the LED's B_{mod}. Note that the reduction in η_s is expected for β > 0.6 in contrast to β < 0.2. The highest R_b and η_s achieved were 7 Mb/s and 5.83 b/s/Hz, respectively for L_s = 10 and β = 0.2. These values are the same as the highest R_b and η_s achieved for the 6-CAP link but higher than the 2-CAP link. Thus, it is clear that no improvement was obtained by increasing the *m*-CAP order beyond *m* = 6, due to the low value of the utilised B_{sig}.

Furthermore, such a huge value of L_f = 481 taps/filter for L_s = 10 and β = 0.2 introduced no improvement in the system performance, but increased the complexity of the system. Figure 4.24(c) illustrates the corresponding filter taps for a range of β and L_s values, and the received constellation diagrams of the S = 1 and S = 5 sub-carriers for L_s = 10 and β = 0.2. It is clear from Figure 4.24(c) that the required filter taps substantially increased, raising the computational complexity compared to the 8-CAP, 6-CAP and 2-CAP links.

Finally, a summary of the highest R_b and η_s achieved and the corresponding L_s and L_f values for a range of *m* = {2, 4, 6, 8, 10} and for B_{sig} = 1 MHz and 2 MHz is provided in a tabular form in Table 4.3 and Table 4.4, respectively. It should be noted that the results of *m* = 4 are included in the tables but not discussed in the results section due to achieving similar performance to the other *m*-CAP links. It is clear from the summarised results that for B_{sig} = 1 MHz, a maximum improvement of ~9.69% in R_b was achieved, with R_b increasing from 6.50 Mb/s for the 2-CAP link to 7.14 Mb/s for the 8-CAP link. Also, it should be noted that the performance improvement in R_b was negligible for *m* > 4, due to the increase in the bandwidth per individual sub-carrier as a result of increasing *m*. Thus,

higher SNR values are unlikely to be achieved. Note that for B_{sig} = 1 MHz, the maximum improvement in η_s was 40.43%, with η_s increasing from 4.23 b/s/Hz for the 2-CAP link to 5.94 b/s/Hz for the 8-CAP link, which is considerably significant. However, it should be borne in mind that this improvement came at the cost of extra computational complexity (more taps/filter). Considering the B_{sig} = 2 MHz case, an improvement in R_b was achieved, whereas η_s was reduced (refer to Table 4.4).

Table 4.3. The highest achieved R_b and η_s for different m-CAP orders and B_{sig} = 1 MHz

m*-CAP order *m	**2**	**4**	**6**	**8**	**10**
Data rate R_b (Mb/s)	6.50	7	7	7.14	7
Truncated symbols L_s / roll-off factor β	10 / 0.8	10 / 0.8	10 / 0.2	10 / 0.2	10 / 0.2
Filter length L_f (taps/filter)	161	301	301	401	481
Spectral efficiency η_s (b/s/Hz)	4.23	5	5.83	5.94	5.83
Truncated symbols L_s / roll-off factor β	10 / 0.3	10 / 0.2	10 / 0.2	10 / 0.2	10 / 0.2
Filter length L_f (taps/filter)	121	201	301	401	481

Table 4.4. The highest achieved R_b and η_s for different m-CAP orders and B_{sig} = 2 MHz

m*-CAP order *m	**2**	**4**	**6**	**8**	**10**
Data rate R_b (Mb/s)	9.8	10.5	11.33	12.25	11.6
Truncated symbols L_s / roll-off factor β	10 / 0.8	10 / 0.8	10 / 0.4	10 / 0.2	10 / 0.2
Filter length L_f (taps)	161	301	341	401	481
Spectral efficiency η_s (b/s/Hz)	3.7	4	4.31	5.10	4.83
Truncated symbols L_s / roll-off factor β	10 / 0.3	10 / 0.2	10 / 0.2	10 / 0.2	10 / 0.2
Filter length L_f (taps)	121	201	301	401	481

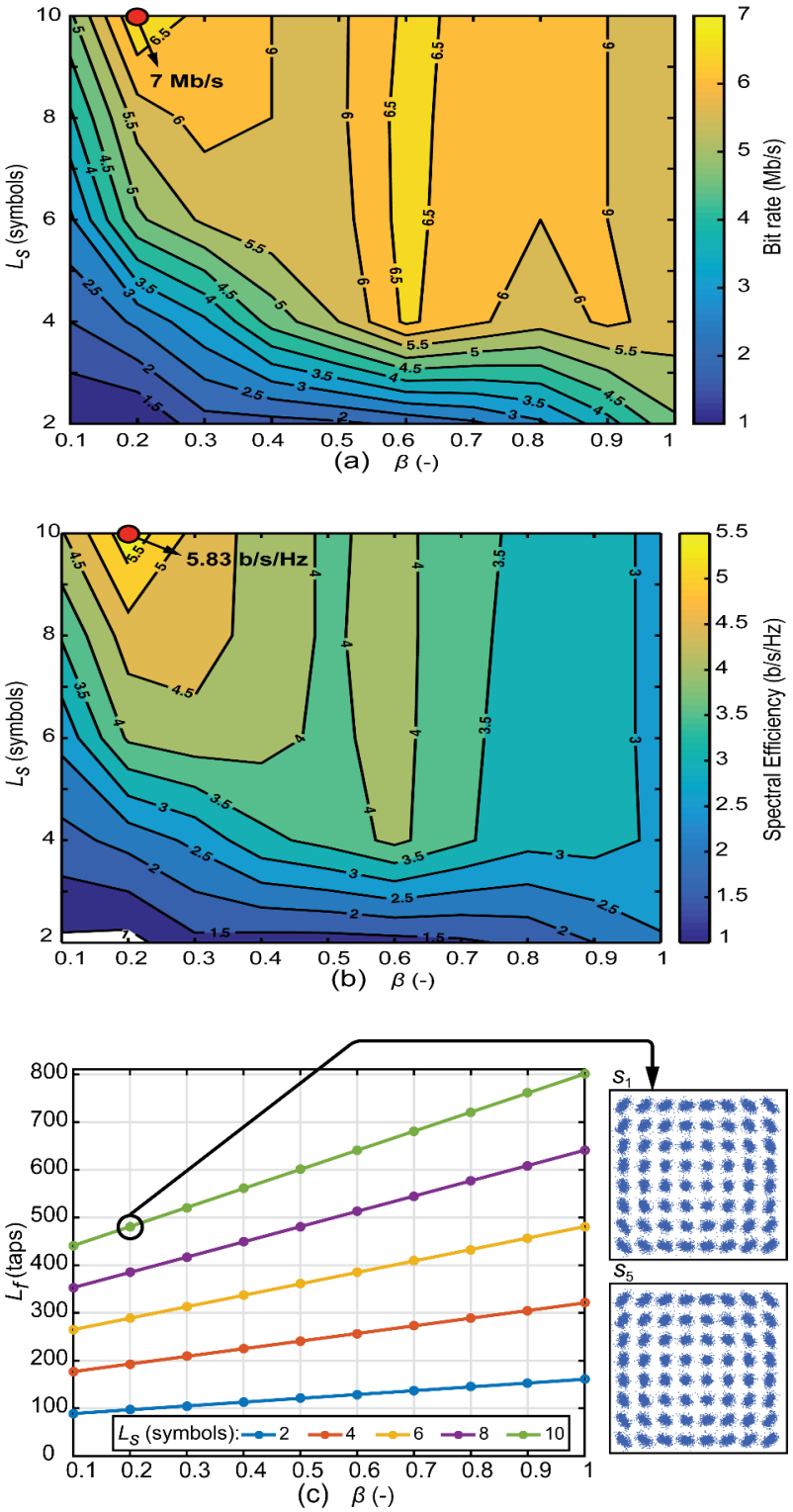

Figure 4.24. The 10-CAP system's (a) data rate as a function of L_s and β, (b) spectral efficiency as a function of L_s and β, and (c) filter length as a function of β. The insets show the received constellation diagrams for the sub-carriers $S = 1$ and $S = 5$ for $\beta = 0.2$ and $L_s = 10$ [122]

4.7 **Summary**

In this chapter, numerical simulations demonstrating the principles of implementing the *m*-CAP scheme enhanced by DFE for different *m*-CAP orders ($m = \{1, 2, 5, 10\}$) were presented. The simulations showed that deploying DFE introduces a noticeable improvement in the BER performance for the low orders of *m*-CAP (i.e., $m = \{1, 2\}$). However, the DFE fails to introduce any significant improvement in the BER performance for the high *m*-CAP order (i.e., $m = \{5, 10\}$). This chapter also discussed the impact of tuning the values of the L_f and β parameters of FIR filters on the BER performance when considering different sets of $m = \{2, 5, 10\}$. The results showed a huge impact of the two aforementioned parameters on the BER performance. Furthermore, it was demonstrated that deploying $L_f > 12$ symbols is impractical as it introduces an increased computational complexity without any improvement in the BER performance.

In addition, an experimental demonstration of *m*-CAP links utilising different parameters of the FIR filter (i.e., L_f and β) was carried out and the results showed that both parameters had a huge impact on the system throughput and spectral efficiency. In addition, it was shown that low order *m*-CAP links (e.g., 6-CAP) could be adopted in order to provide a similar R_b and η_s performance to that of higher order *m*-CAP links, while offering much lower filter taps requirements, which is considered as the main cause of computational complexity in such systems.

Chapter 5 NEW CONCEPT OF MULTI-BAND CAP FOR BAND-LIMITED VLC LINKS

5.1 Introduction

As explained in Chapter 3 (see section 3. 4), the concept behind the *m*-CAP modulation scheme was experimentally demonstrated for the first time in VLC. In the *m*-CAP scheme, B_{tot} is split into *m* sub-carriers in order to relax the requirement of a flat frequency response. In other words, the signal attenuation per equally spaced sub-carriers is less than that of a single sub-carrier (i.e., the conventional CAP) over the entire allocated B_{tot}. In the tested system, the conventional CAP signal was divided equally into $m = \{2, 4, 6, 8, 10\}$ sub-carriers over a fixed B_{tot} of 6.5 MHz. Dividing into *m*-sub-carriers led directly to an increase in the SNR per sub-carrier for increasing *m*, thus allowing bit-loading. The SNR was estimated via the EVM of a BPSK pilot for each sub-carrier, before updating each sub-carrier with the appropriate number of bits/symbol. It was shown that by increasing the number of sub-carriers, higher transmission speeds (spectral efficiency) of 31.53 Mb/s (4.85 b/s/Hz) could be achieved for $m = 10$. However, increasing the number of sub-carriers in an *m*-CAP system leads to the growth of the required number of pulse

shaping FIR filters both at the Tx and the Rx, and hence, a substantial rise in the overall system computational complexity.

In this chapter, motivated by the relationship between the improved performance and increased complexity, a new *m*-CAP concept is introduced, where instead of dividing the sub-carriers equally, the first sub-carrier bandwidth is set to be equal to the LED's B_{mod}, and the remaining sub-carriers are equally divided over the remaining B_{tot} in order to simulate a moderate band-limitation, and to investigate the impact of unequal B_{tot} distribution over all sub-carriers on the system performance against complexity. Note that, B_{tot} is normalised to 1 Hz/Hz in order to maintain generality, and B_{mod} is chosen to be $0.5B_{tot}$. By implementing this concept, it will be shown that by using m = 10, 8, 6 and 4, the computational complexity is reduced by 80%, 75%, ~67% and 50% when compared with the conventional 10, 8, 6 and 4-CAP, respectively, with a maximum power penalty of ~1.5 dB.

This chapter also provides a further insight into the new *m*-CAP system performance by investigating the achievable data throughput. However, in order to investigate all the possible sub-carriers distributions among the B_{tot}, the distribution of the sub-carriers is done such that x sub-carriers are allocated within the -3 dB shoulder region and $y = m\text{-}x$ sub-carriers are divided equally to the outside of the -3 dB shoulder region. An improvement in the R_b of ~36% compared to the conventional 6-CAP is achieved when implementing a $6_{x/y}$-CAP system.

5.2 **Proposed System**

Figure 5.1 illustrates the new *m*-CAP system concept for m = 4, 6, 8 and 10. The 1st sub-carrier S_1 is always set to B_{mod} (0.5 Hz/Hz) in order to relax the flat frequency response requirement for the 1st sub-carrier. The rest of B_{tot} is divided into m-1 equal parts as given by:

$$B_{\text{tot},i} = \begin{cases} \dfrac{B_{\text{tot}}}{2}, & i = 1 \\ \dfrac{B_{\text{tot}} - \dfrac{B_{\text{tot}}}{2}}{m-1}, & i = 2{:}m \end{cases} . \tag{5.1}$$

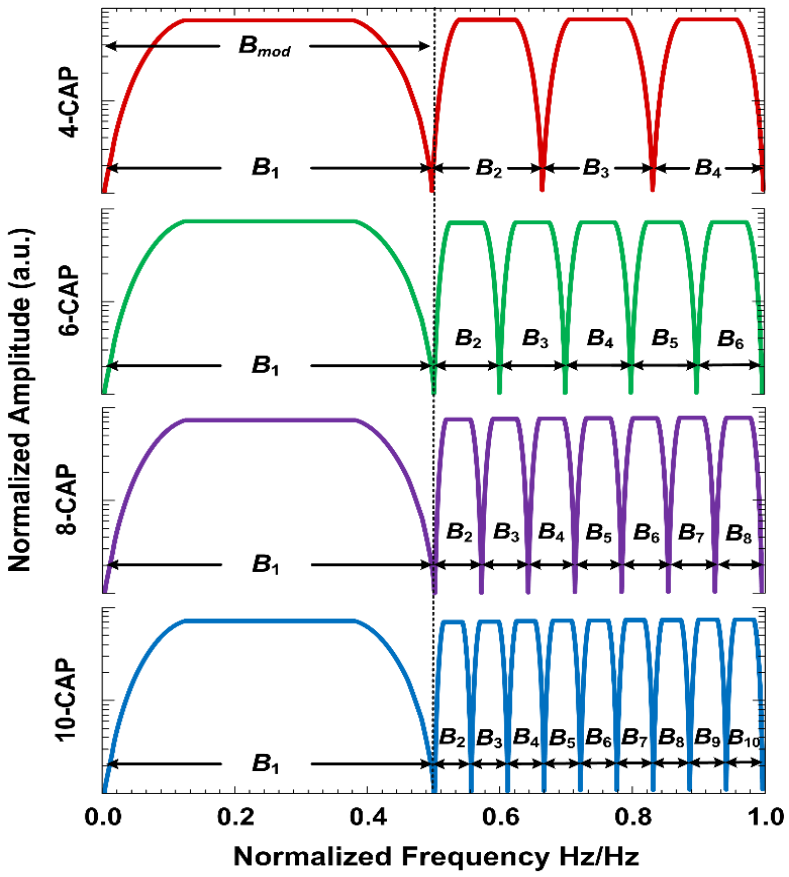

Figure 5.1. The new *m*-CAP concept in terms of frequency response for m = 4, 6, 8 and 10. It should be noted that B_{mod} indicates the modulation bandwidth which is set to 0.5 Hz/Hz [123]

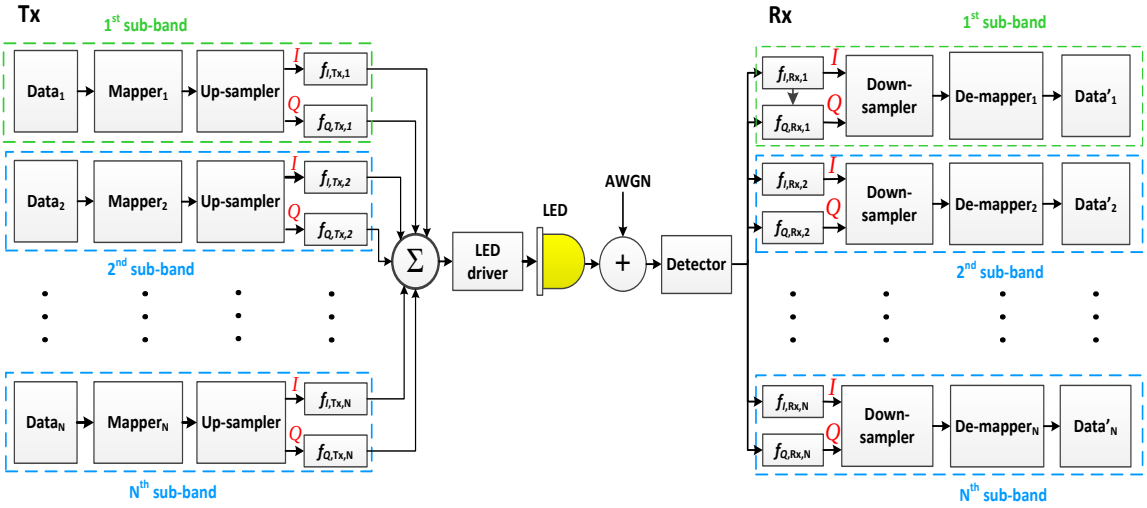

Figure 5.2. The block diagram of the proposed *m*-CAP system [123]

For instance, for $m = 4$; $S_1 = B_{\text{mod}} = 0.5$ Hz/Hz, while S_2, S_3, and S_4 are set to 0.166 Hz/Hz. Figure 5.2 illustrates the block-diagram of the proposed system. Firstly, for each sub-carrier, a 2^{17}-1 length PRBS is generated before mapping into *M*-QAM constellations. It should be noted that the QAM order adopted in this work is 16-QAM without any loss in generality, and that the predicted 16-QAM BER plot, which is sometimes known as the bit error probability without coding, is given as [124]:

$$P_{eb} \approx \frac{3}{8} \cdot \text{erfc}\left(\sqrt{\frac{2}{5} \cdot \frac{E_b}{N_o}}\right), \tag{5.2}$$

where erfc is the complementary error function.

The mapped data is up-sampled according to the number of samples n_{samp}, as given in (3.1). The up-sampled data is then split into *I* and *Q* components.

The pre-transmission signals of the transmit *I* and *Q* SRRC filters are given by, respectively:

$$S_{I,f}(t) = d_I(t) \otimes f_{I,Tx,i}(t), \tag{5.3}$$

$$S_{Q,f}(t) = d_Q(t) \otimes f_{Q,Tx,i}(t), \tag{5.4}$$

where $d_I(t)$ and $d_Q(t)$ are the I and the Q baseband data, respectively, $\otimes$ denotes convolution, and $f_{I,Tx,i}(t)$ and $f_{Q,Tx,i}(t)$ denote the IR of the I and Q SRRC filters for m^{th} of i^{th} sub-carrier, respectively, as given in (3.4) and (3.5).

In this work, β is set to 0.15 for consistency with the literature [45, 96]. As the sub-carriers are not divided equally over B_{tot}, the carrier frequency $f_{c,i}$ of the i^{th} sub-carrier is thus given in this work by:

$$f_{c,i} = \begin{cases} \dfrac{B_{mod}}{2} & i = 1 \\ \dfrac{B_{tot} - B_{mod}}{2(m-1)}(i-1) + \dfrac{B_{mod}}{2} & i = 2 \ \ldots, m \end{cases}. \tag{5.5}$$

The final transmission waveform is found by subtracting the pre-transmission signals as follows:

$$S(t) = S_{I,f}(t) - S_{Q,f}(t). \tag{5.6}$$

The signal is then used to intensity modulate the LED, which is modelled as an ideal analogue LPF with B_{mod} = 0.5 Hz/Hz. In the channel, AWGN is added to the transmission signal, and the signal is then detected by a PD at the Rx side. The detected signal is passed to the time-reversed in-phase $f_{I,Rx,i}(-t)$ and quadrature $f_{Q,Rx,i}(-t)$ SRRC filters following down-sampling. Finally, the constellation is de-mapped. In order to determine the BER, a symbol-by-symbol calculation is performed. In this work, the BER target is set at 10^{-4} to allow enough headroom for the 7% FEC BER limit of 3.8×10^{-3}.

5.3 Results and Discussion

This section presents the BER performance results of the new and conventional m-CAP systems for m = 4, 6, 8 and 10 as a function of E_b/N_0 when the modulation format is 16-QAM (without any loss of generality). It should be noted that for the conventional m-

CAP, the sub-carriers are divided equally across B_{tot}, whereas for the proposed *m*-CAP, the 1st sub-carrier is set to B_{mod}, while the remaining sub-carriers are evenly spaced across the out-of-band B_{tot}, as discussed in the previous section.

A performance comparison of the new *m*-CAP with the conventional *m*-CAP is presented below.

5.3.1 **10-CAP System**

Figure 5.3 depicts the performance of the new 10-CAP along with the average performance of the first five sub-carriers of the conventional *m*-CAP (dots-red). The 1st sub-carrier achieved the BER target of 10^{-4} at E_b/N_0 of ~15.5 dB. This BER performance is the same as the average BER performance of the first five sub-carriers of the conventional *m*-CAP, which occupy B_{mod} with a power penalty of ~1.5 dB. Note that, the average of the first five sub-carriers of the conventional *m*-CAP achieved the BER target at E_b/N_0 ~14 dB. This is remarkable as it indicates that by using one sub-carrier in the newly proposed 10-CAP, a similar performance to that of the average of the first five sub-carriers in the conventional 10-CAP could be achieved.

It should be noted that for each increment of *m*, two more pulse shaping FIR filters are needed (one for real data and one for imaginary data) at the Tx and another two FIR filters are required at the Rx as well. As such, for m = 10, 20 FIR filters are needed at the Tx and Rx. Thus, by sacrificing a power penalty of ~1.5 dB using the new 10-CAP system, the computational complexity can be reduced by up to 80% by using fewer FIR filters, therefore avoiding the major point of criticism in the traditional *m*-CAP system. It should be noted that, *S* indicates the individual sub-carriers within a given *m*, where *m* refers to the total number of sub-carriers in the given link.

The out of B_{mod} sub-carriers in the new 10-CAP achieved the designated BER target starting from E_b/N_0 ~16 dB for the 2nd sub-carrier, and it is clear that by increasing the number of sub-carriers, they experienced high-frequency attenuation being outside B_{mod}. However, in contrast with the conventional 10-CAP, the sub-carriers achieved slightly improved performance due to the fact that, the B_{sc} outside B_{mod} in the proposed 10-CAP was B_{sc} = 0.5/9 = 0.055Hz/Hz, which is less than B_{sc} = 0.1Hz/Hz in the conventional 10-CAP. As a result, they offer a closer approximation to a flat band response. The 10th sub-carrier converged to the BER target at E_b/N_0 ~20 dB, with ~8 dB and ~4.5 dB power penalties in comparison with the predicted curve and the 1st sub-carrier, respectively. This is reflected in the constellation diagram of the 10th sub-carrier shown in the inset of Figure 5.3, for E_b/N_0 of 20 dB.

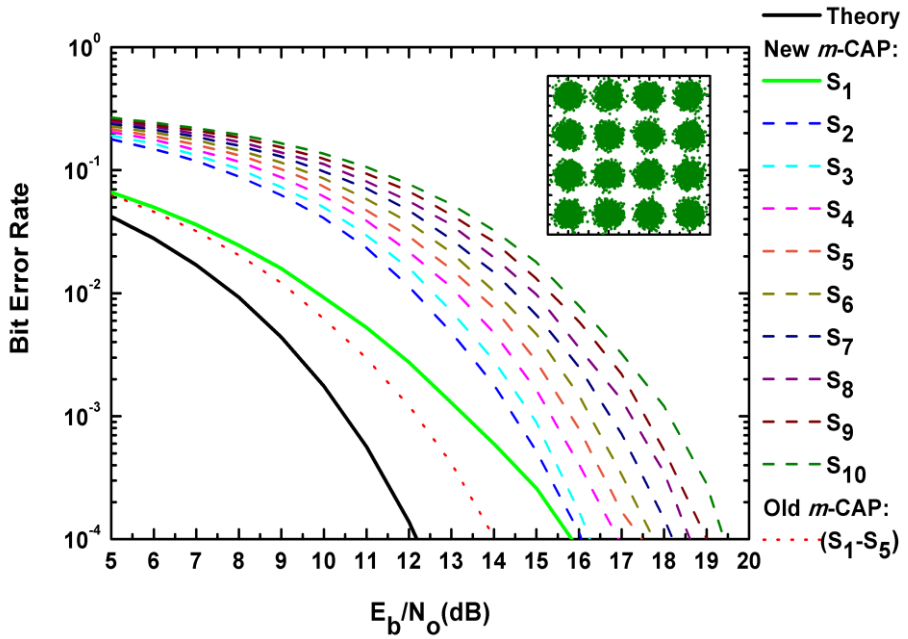

Figure 5.3. BER performance of: 16-QAM (theory, black solid line), the average of the first five sub-carriers of the conventional 10-CAP (red dots), the 1st sub-carrier (green solid line), and the out of B_{mod} sub-carriers S_2-S_{10} of the new 10-CAP (dashed lines), as a function of E_b/N_0. It should be noted that S indicates the individual number of sub-carriers [123]

5.3.2 **8-CAP System**

For the new 8-CAP system (Figure 5.4), the 1st sub-carrier performance was the same as that of 1st sub-carrier of the new 10-CAP, where it achieved the designated BER at E_b/N_0 of ~15.5 dB as expected as it is always set to B_{mod}. The average performance of the first four sub-carriers achieved the BER target at E_b/N_0 of ~14 dB, thus outperforming the 1st sub-carrier performance by ~1.5 dB. This is reasonable as it indicates that the average of the first four sub-carriers of the new 4-CAP, which are within B_{mod}, achieves a similar SNR requirement as the average of the first five sub-carriers of the new 10-CAP. Implementing the new 8-CAP system, the 1st sub-carrier showed a reduction of ~75% in computational complexity compared to the first four sub-carriers of the conventional 8-CAP, while incurring a ~1.5 dB power penalty. As expected, the out of B_{mod} sub-carriers experienced high-frequency attenuation imposed by the behaviour of the LED, which acts as a first order LPF. This is further illustrated by the inset constellation diagram in Figure 5.4 of the 8th sub-carrier of the new 8-CAP system.

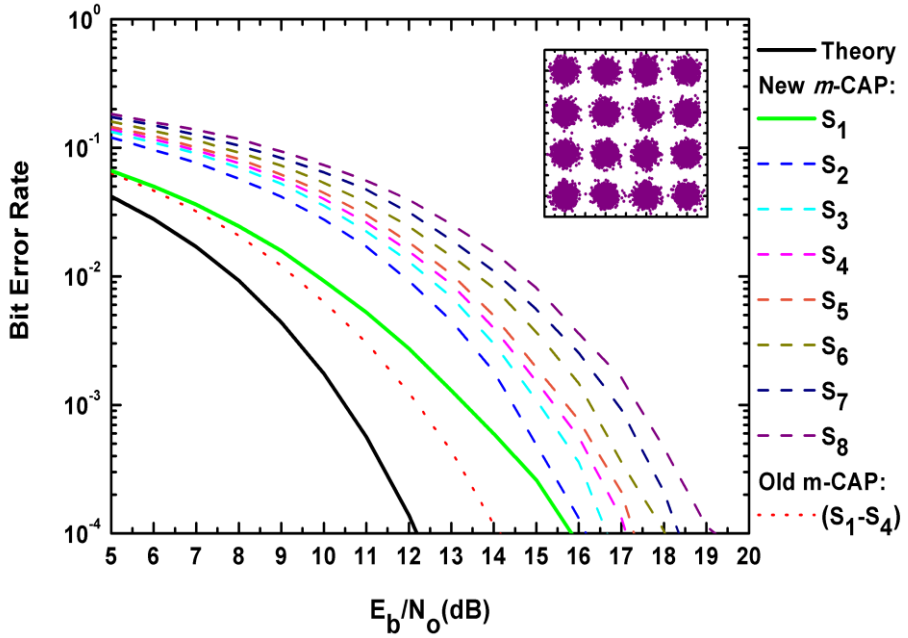

Figure 5.4. BER performance of: 16-QAM (theory, black solid line), the average of the first four sub-carriers of the conventional 8-CAP (red dots), 1st sub-carrier (green solid line), and the out of B_{mod} sub-carriers S_2-S_8 of the new 8-CAP (dashed lines), as a function of E_b/N_0. There is an attenuation due to the first order LPF behaviour of the LED, as can be clearly inspected from the constellation diagram [123]

5.3.3 **6-CAP System**

Figure 5.5 illustrates the performance of the new 6-CAP system, where the 1st sub-carrier had a power penalty of ~1.5 dB compared with the average of the first three sub-carriers in the conventional 6-CAP scheme (B_{sc} = 0.166 Hz/Hz). Such a performance is also identical to that of the new 10 and 8-CAP, but with a ~67% reduction in the system computational complexity. Once again, the out of B_{mod} sub-carriers experienced different high-frequency attenuation, as illustrated by the inset constellation diagram in Figure 5.5 at E_b/N_0 = 20 dB.

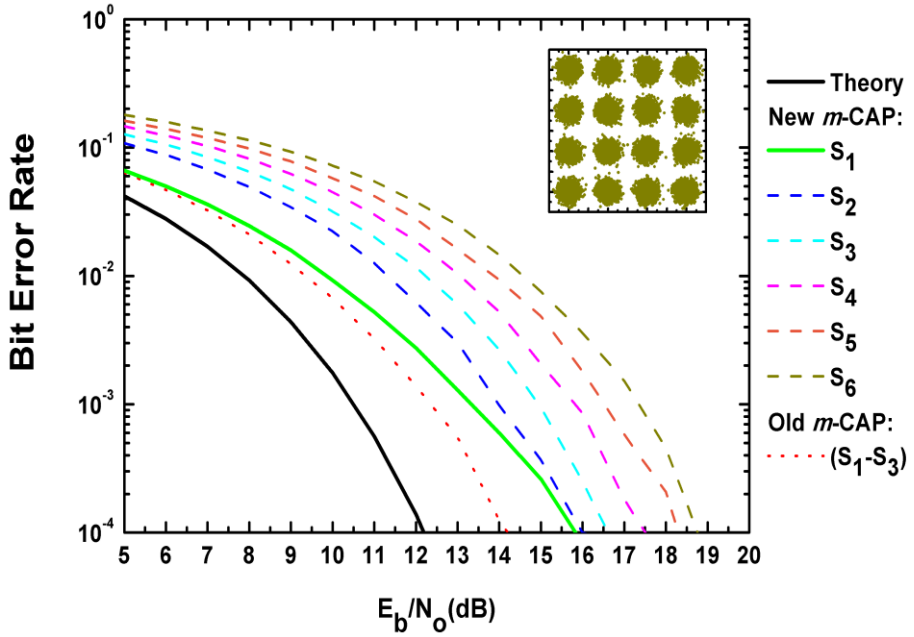

Figure 5.5. BER performance of: 16-QAM (theory, black solid line), the average of first three sub-carriers of the traditional 6-CAP (red dots), 1st sub-carrier (green solid line), and the out of B_{mod} sub-carriers S_2-S_6 of the new 6-CAP (dashed lines), versus E_b/N_0 [123]

5.3.4 **4-CAP System**

As depicted in Figure 5.6, the 1st sub-carrier of the new 4-CAP achieved a lower power penalty of ~1 dB compared with the average performance of the first two sub-carriers in the conventional 4-CAP system (B_{sc} = 0.25 Hz/Hz). This is due to the larger B_{sc} compared with B_{sc} of the conventional 6, 8 and 10-CAP**.** However, the computational complexity of the conventional 4-CAP system is increased by only ~50% in comparison with the new 4-CAP system. The inset constellation diagram in Figure 5.6 confirms the out of B_{mod} attenuation experienced by the 4th sub-carrier.

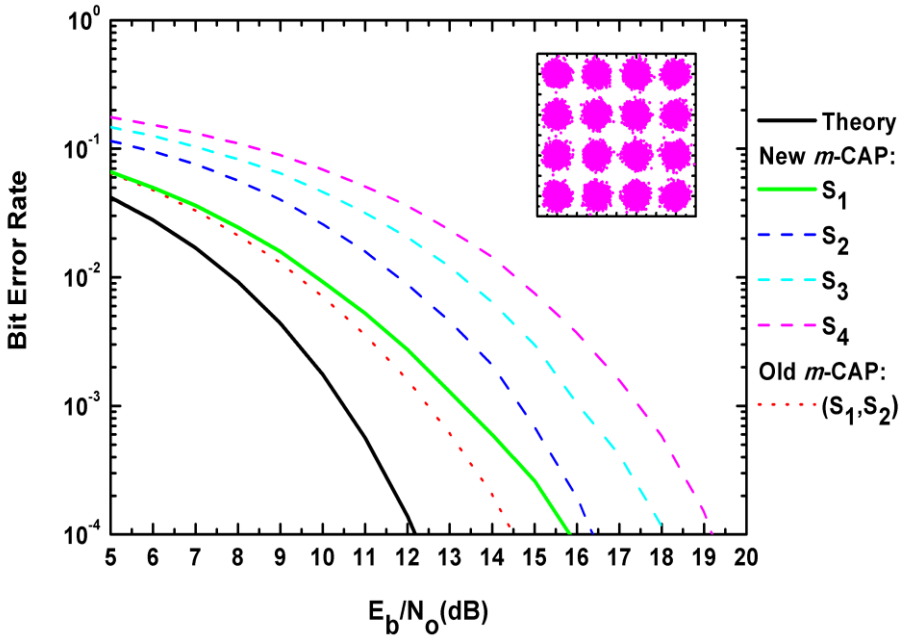

Figure 5.6. BER performance of: 16-QAM (theory, black solid line), the average of the first two sub-carriers of the conventional 4-CAP (red dots), the 1st sub-carrier of the new 4-CAP (green solid line), and the out of B_{mod} sub-carriers S_2-S_4 of the new 4-CAP (dashed lines), as a function of E_b/N_0. The high-frequency attenuation can be clearly seen from the constellation diagram of the last sub-carrier S_4 when E_b/N_0 = 20 dB [123]

5.4 Data Rate Performance of a Variable *m*-CAP VLC Link

In this section, the work presented in the previous section is extended. This time, the investigation focuses on the possible improvement in the system throughput. Furthermore, the investigation is conducted theoretically by variably splitting the sub-carriers in the newly proposed concept of the *m*-CAP system. In addition, the number of sub-carriers is divided into *m* sub-carriers, so that *x* sub-carriers are located within the LED's B_{mod} region, and the remaining $y = m\text{-}x$ sub-carriers are divided equally into the remaining part of B_{tot} as follows: 2-CAP (x/y = 1/1), 4-CAP (x/y = 1/3, 2/2, 3/1) and 6-CAP (x/y = 1/5, 2/4, 3/3, 4/2, 5/1).

5.4.1 Variable *m*-CAP System Setup

As discussed and demonstrated earlier, the traditional *m*-CAP system is based on dividing the sub-carriers into *m* equally distributed individual sub-carriers over the entire signal bandwidth (B_{tot}), as illustrated in Figure 5.7(a). However, adopting a nonuniform distribution of *m* over B_{tot} can improve the system throughput, and the extent of such an improvement is investigated in this section. In order to fulfil this, B_{tot} is not distributed among the sub-carriers in a way that the first sub-carrier occupies B_{mod} ($0.5B_{tot}$) and the rest of sub-carriers share the remaining part of B_{tot}, as adopted in the above section (section 5.2). Instead, in this work, B_{tot} is divided into *m* sub-carriers with *x* sub-carriers occupying the LED's B_{mod} region, and $y = m\text{-}x$ sub-carriers equally share the remaining B_{tot} (outside the LED's B_{mod} region), as illustrated in Figure 5.7(b) for 6-CAP (x = 2 and y = 4) and B_{mod} of $0.2B_{tot}$. This new implementation of the *m*-CAP system is denoted as $m_{x/y}$-CAP such that: $2_{x/y}$-CAP (x/y = 1/1), $4_{x/y}$-CAP (x/y = 1/3, 2/2, 3/1) and $6_{x/y}$-CAP (x/y = 1/5, 2/4, 3/3, 4/2, 5/1).

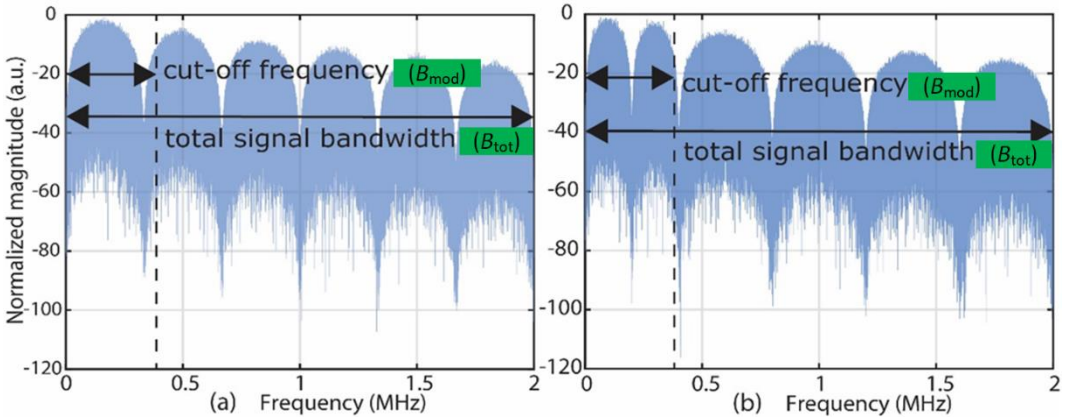

Figure 5.7. An example of the transmitted signal's frequency spectrum for: (a) traditional 6-CAP signals, and (b) variable 6-CAP signals with x = 2 and y = 4 sub-carriers within and outside the LED's B_{mod} region, respectively [125]

The generation and reconstruction of the variable m-CAP signals are achieved in an identical fashion to that explained in the earlier section (refer to section 5. 2).

As the sub-carriers are variably divided over B_{tot}, the carrier frequency $f_{c,i}$ of the i^{th} sub-carrier is thus given by:

$$f_{c,i} = \frac{1}{x}\left(i - \frac{1}{2}\right) \cdot B_{\text{tot}} \cdot B_{\text{mod}}, \qquad i = 1, \dots, x \tag{5.7}$$

for x sub-carriers, and:

$$f_{c,i} = B_{\text{tot}}\left(\frac{\left(i - x - \frac{1}{2}\right) \cdot (1 - B_{\text{mod}})}{y} + B_{\text{mod}}\right), \qquad i = x + 1, \dots, m \tag{5.8}$$

for the remaining y sub-carriers (i.e., $y = m$-x).

The utilised parameters for this numerical investigation are as follows: the number of sub-carriers m = {2, 4, 6}, B_{mod} = {0.1, 0.2, 0.3, 0.4, 0.5} of B_{tot} to guarantee sufficient band-limitation, and x = {1,…, m-1} and y = {1,…, m-1} in order to examine all possible sub-carrier distribution scenarios. As mentioned earlier, the investigation in this numerical simulations focuses on the possible improvement in the achieved R_b. This is achieved by utilising the bit-loading technique based on the EVM measurements of the BPSK pilot

signals, where the estimated SNR is then obtained from the measured EVM. Next, each sub-carrier (denoted as S) is loaded with the appropriate number of bits/symbol based on the estimated SNR, which is compared with $SNR_{thresholds}$ obtained from [113]. The $SNR_{thresholds}$ values are given according to the required BER target, which was set to 10^{-4} in this work (i.e., below the ITU's 7% FEC limit (3.8×10^{-3})) and for consistency with previous studies [45, 120].

5.4.2 **Results and Discussion**

In this section, the results of the achieved R_b using the aforementioned parameters (see section 5.4.1) are presented. In these simulations, the BPSK signals were transmitted over a band-limited (LPF) channel for E_b/N_0 values ranging from 5 to 25 dB. The EVM was calculated and the appropriate number of bits/symbol was loaded for each individual sub-carrier based on the estimated SNR, and the theoretical total R_b was calculated for all

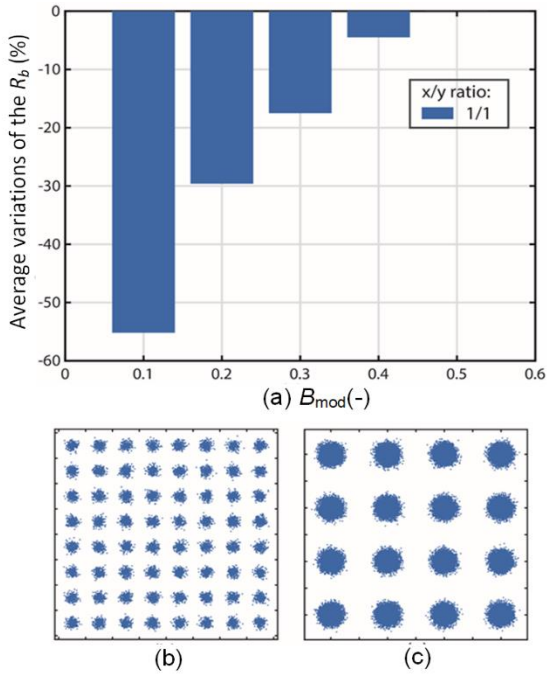

Figure 5.8. (a) The average variations of the total achieved R_b for the $2_{1/1}$-CAP link for a range of B_{mod} values when compared with the traditional 2-CAP link. Also depicted are the received constellation diagrams of (b) S = 1, and (c) S = 2, for B_{mod} of $0.3B_{tot}$ at E_b/N_0 = 20 dB [125]

possible $m_{x/y}$ distributions. The total achieved R_b of the new proposed $m_{x/y}$-CAP link was then subtracted from the total achieved R_b of the traditional m-CAP for each given value of E_b/N_0. It should be noted that, the results are shown here as the average variations of the resultant values, that is, the total R_b difference of $m_{x/y}$-CAP and m-CAP over a set of E_b/N_0 for a range of $B_{mod} = \{0.1, 0.2, 0.3, 0.4, 0.5\}B_{tot}$.

Figure 5.8(a) depicts the average variations of the total achieved R_b of the $2_{1/1}$-CAP link for a range of E_b/N_0 values (i.e., 5 to 25 dB) compared with the traditional 2-CAP link. As can be seen from the figure, for the band-limited channels (i.e., $B_{mod} < 0.5B_{tot}$), no improvement in the $2_{1/1}$-CAP system performance is predicted when compared with the traditional 2-CAP system. This is due to the fact that, the bandwidth requirement of the 2nd sub-carrier is larger than the 1st sub-carrier, which implies that it is more prone to the impact of the high-frequency attenuation outside the -3 dB shoulder. Even though the 1st sub-carrier is within the B_{mod} region, its bandwidth is too low to support a high R_b. It should be noted that the only case where the variation is zero is predicted at $B_{mod} = 0.5B_{tot}$. This is due to having the same bandwidth distribution of the sub-carriers (i.e., S_1 and S_2) as in the traditional 2-CAP system. Figure 5.8(b) and (c) show the received constellation diagrams of S_1 (64-QAM) and S_2 (16-QAM), respectively, for $B_{mod} = 0.3B_{tot}$ at $E_b/N_0 =$ 20 dB.

Figure 5.9(a) shows an R_b performance comparison between the $4_{x/y}$-CAP link and the conventional 4-CAP link in terms of the average variations of the total achieved R_b as a function of B_{mod} for all possible sub-carriers distributions (i.e., x/y = 1/3, 2/2 and 3/1). As can be observed from the figure, the $4_{1/3}$-CAP system shows the best performance enhancement, with average improvements of 10.2%, 16.1% and 20.8% for B_{mod} = 0.3, 0.4 and 0.5, respectively, in contrast to the traditional 4-CAP link. This improvement is achieved as a result of having the 1st sub-carrier within the LED's -3 dB region, bearing

in mind that the larger the B_{mod}, the larger the 1st sub-carrier's bandwidth, which was located in the B_{mod} region.

For $B_{mod} = 0.1B_{tot}$, the traditional 4-CAP link is predicted to outperform the proposed $4_{x/y}$-CAP link significantly regardless of the *x*/*y* distributions, as $m_{x/y}$-CAP show a recorded reduction of ~29.4%, 36.5% and 45.5% for *x*/*y* distributions of 1/3, 2/2 and 3/1, respectively, this is attributed to the impact of the high-frequency attenuation encountered by the out of the -3 dB band sub-carriers (or sub-carrier in $4_{3/1}$-CAP link) due to the high bandwidth requirement.

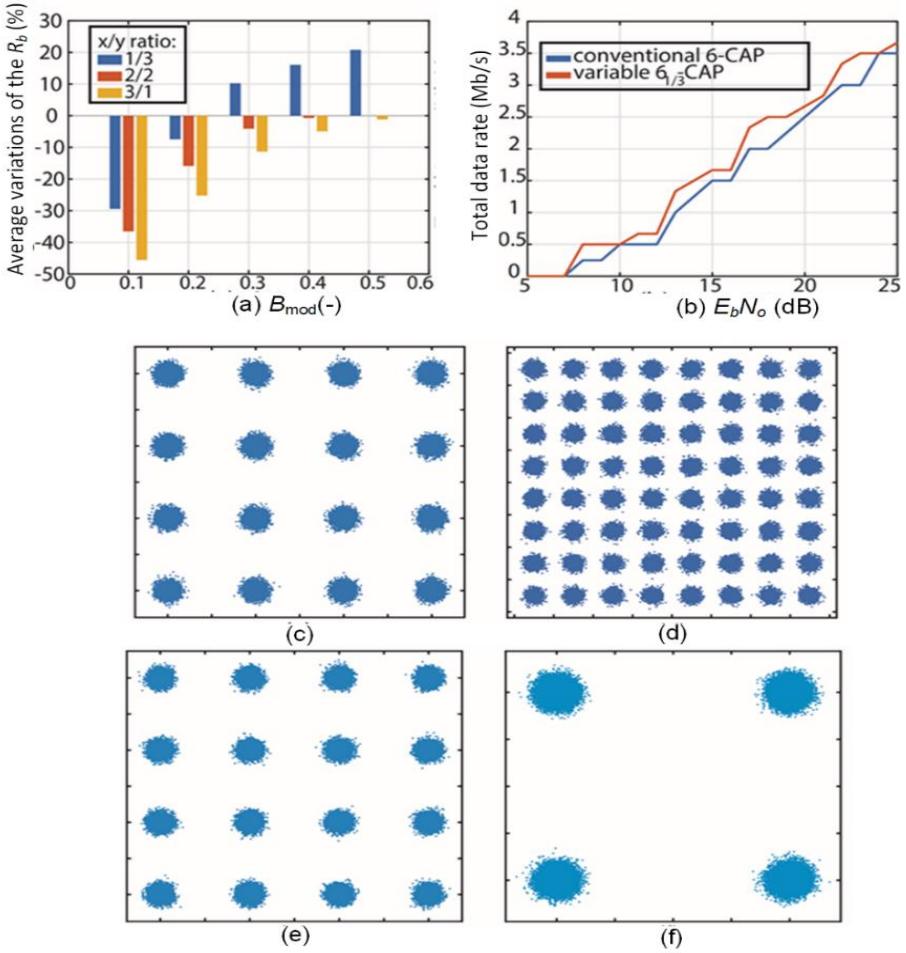

Figure 5.9. (a) The average variations of the total achieved R_b for the $4_{1/3}$-CAP link (blue), $4_{2/2}$-CAP link (red) and $4_{3/1}$-CAP (yellow) link for a range of B_{mod} values when compared with the traditional 4-CAP link. (b) The total achieved R_b of the $4_{3/1}$-CAP (red) and the conventional 4-CAP (blue) as a function of E_b/N_0. Also depicted are the received constellation diagrams of (c) S = 1, (d) S = 2, (e) S = 3, and (f) S = 4 of the $4_{1/3}$-CAP link, for B_{mod} of $0.3B_{tot}$ at E_b/N_0 = 20 dB [125]

The total achieved R_b of both the variable $4_{1/3}$ link and the conventional 4-CAP link is illustrated in Figure 5.9(b). It is clear that the $4_{1/3}$-CAP link outperforms the conventional 4-CAP link and that the largest difference in R_b of 0.5 Mb/s (i.e., 25%) is achieved at E_b/N_0 = 18 dB.

Furthermore, a more significant enhancement in R_b is expected by increasing B_{mod}. To further demonstrate the improvement in the system performance, the received constellation diagrams of the sub-carriers S = 1 (16-QAM), S = 2 (64-QAM), S = 3 (16-QAM) and S = 4 (4-QAM) for the best system performance of the $4_{x/y}$ links (i.e., $4_{3/1}$ link) for $B_{\text{mod}} = 0.3B_{tot}$ at E_b/N_0 = 20 dB are shown in Figure 5.9(c)-(f), respectively.

Figure 5.10(a) plots the average variations of R_b as a function of B_{mod} for all possible $6_{x/y}$-CAP link sub-carriers distributions when compared with the traditional 6-CAP link. The results follow the same pattern as those obtained by comparing the $4_{x/y}$ –CAP link with the conventional 4-CAP link. Moreover, as expected, the $6_{x/y}$-CAP link fails to introduce any improvement at very low B_{mod} values (i.e., $0.1B_{\text{tot}}$). However, the simulations show an enhanced performance is achieved for the $6_{1/5}$-CAP system starting from $B_{\text{mod}} = 0.2B_{\text{tot}}$, and reaching a best performance enhancement of ~30% for $B_{\text{mod}} = 0.4B_{\text{tot}}$ (see Figure 5.10(a)).

As illustrated in Figure 5.10(b), the biggest increase in R_b of 36% (~0.54 Mb/s) that the $6_{x/y}$-CAP link achieves over the traditional 6-CAP link occurs for $B_{\text{mod}} = 0.4B_{\text{tot}}$ and E_b/N_0 = 17 dB. The reason behind achieving enhanced performance for all the possible sub-carrier distributions of the $6_{x/y}$ link over the conventional 6-CAP link at $B_{\text{mod}} = 0.4B_{\text{tot}}$ is attributed to the reduced bandwidth requirements of sub-carriers within the -3 dB region. This is further demonstrated via the received constellation diagrams of S = 1 (64-QAM), S =2 (64-QAM), S =3 (16-QAM), S =4 (16-QAM), S =5 (4-QAM), and S =6 (4-QAM),

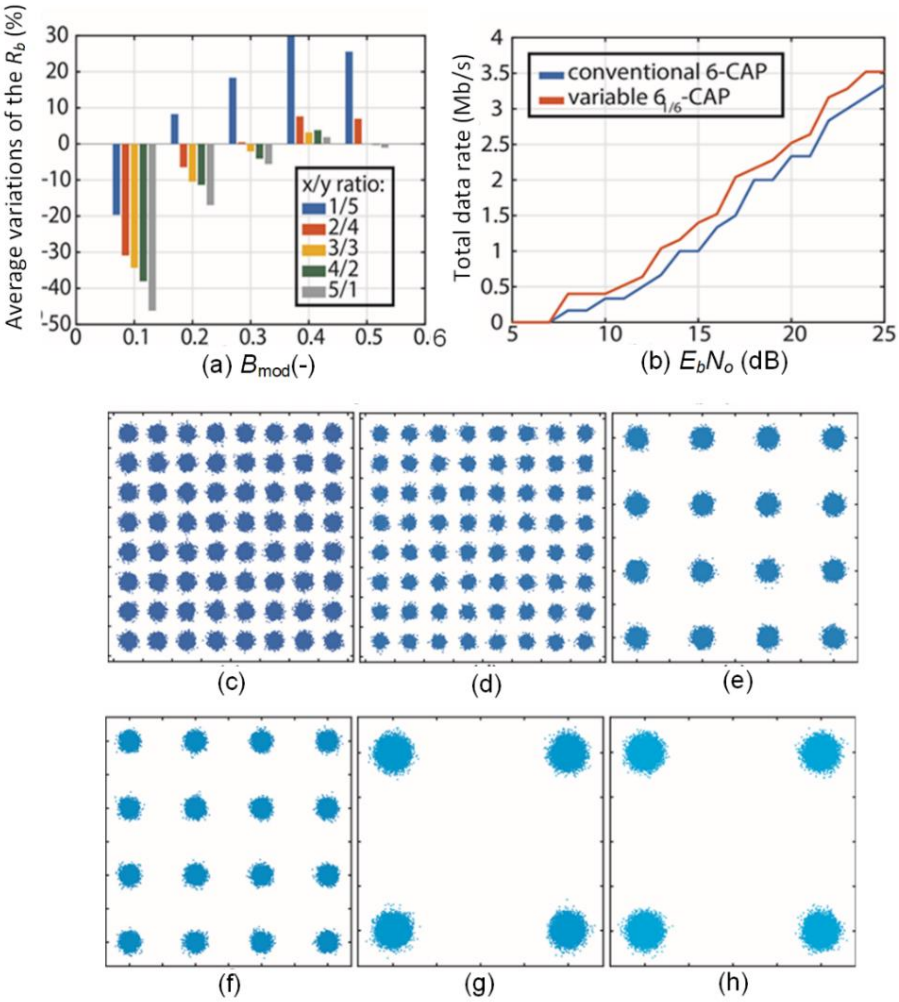

Figure 5.10. (a) The average variations of the total achieved R_b for the $6_{1/5}$-CAP link (blue), $6_{2/4}$-CAP link (red), $6_{3/3}$-CAP link (yellow), $6_{4/2}$-CAP link (green) and $6_{5/1}$-CAP link (grey) for a range of B_{mod} values when compared with the traditional 6-CAP link. (b) The total achieved R_b of the $6_{1/5}$-CAP link (red) and the conventional 6-CAP (blue) as a function of Eb/N_0. Also depicted are the received constellation diagrams of (c) S = 1, (d) S = 2, (e) S = 3, (f) S = 4, (g) S = 5 and (h) S = 6 of the $6_{1/5}$ –CAP link, for B_{mod} of $0.3B_{tot}$ at E_b/N_0 = 20 dB [125]

of the $6_{1/5}$ –CAP link depicted in Figure 5.10(c)-(h), respectively, for $B_{mod} = 0.3B_{tot}$ at E_b/N_0 = 20 dB.

5.5 Summary

This chapter presented and analysed a novel implementation of the *m*-CAP system. The new *m*-CAP concept is implemented by setting the sub-carriers bandwidth such that the first sub-carrier is the same as B_{mod}, and the remaining bandwidth is subsequently equally

shared between the remaining sub-carriers (i.e., m-1). In the first part of this chapter (see section 5. 3), it was shown that by implementing the new concept using m = 10, 8, 6 and 4, the computational complexity was reduced by 80%, 75%, ~67% and 50% when compared with the conventional 10, 8, 6 and 4-CAP systems, respectively, with a maximum power penalty of ~1.5 dB at the chosen BER target of 10^{-4}.

Furthermore, It was demonstrated that the first sub-carrier was able to achieve the target BER 10^{-4} (i.e., below the 7% FEC BER limits of 3.8×10^{-3}) at E_b/N_0 = 15.5 dB. This was achieved at a power penalty of ~1.5 dB relative to the same average performance of the first five, four and three sub-carriers of the conventional 10, 8 and 6-CAP systems, respectively, and a power penalty of ~1 dB relative to the same average performance of the first two sub-carriers of the conventional 4-CAP.

In the second part of this chapter (section 5. 4), a further look into the performance of the new m-CAP scheme was provided by numerically investigating the impact of allocating different bandwidths for the sub-carriers on the R_b performance when compared to the performance of the conventional m-CAP. The sub-carriers were variably distributed so that x sub-carriers were located within the LED's B_{mod} region and the remaining sub-carriers (i.e., $y = m\text{-}x$) were equally divided into the remaining part of B_{tot}. Simulations of the new variable $m_{x/y}$-CAP system predict an improvement of up to ~36% in R_b of the $6_{x/y}$-CAP link in comparison to the traditional 6-CAP link. In addition, it was shown that the larger the order of $m_{x/y}$-CAP, the greater the improvement in the R_b achieved is, in contrast to the traditional m-CAP system, even for a high band-limited VLC system (i.e., $B_{\text{mod}} = 0.2B_{\text{tot}}$).

Chapter 6 HIGH SPEED MIMO VLC EMPLOYING MULTI-BAND CAP

6.1 Introduction

In indoor optical systems, multiple LED-based lighting fixtures are used to provide sufficient illumination levels (i.e., 200-1000 lx [1]), which facilitates the implementation of a MIMO system for VLC [126]. The MIMO scheme can be readily adopted to increase R_b, as multiple data streams can be simultaneously sent and received utilising the multiple Txs and Rxs. Furthermore, since achieving a high data throughput in VLC is challenging and restricted mainly by the low B_{mod} introduced by the first order LPF behaviour of the LED, implementing the MIMO scheme creates an environment where a large number of LEDs with a low B_{mod} are utilised, thus offering a higher throughput communications system.

Moreover, MIMO systems are well known for achieving higher R_b levels than single-input single-output (SISO) systems and multiple-input single-output (MISO) systems. There are two types of optical MIMO schemes, *i*) non-imaging MIMO and *ii*) imaging MIMO. In non-imaging MIMO systems, the signals propagating from each individual LED are exposed to all individual PDs with different extents, which implies that a

different amount of interference among the individual transmitted signals (i.e., inter-channel crosstalk) takes place. Thus, signal processing becomes a crucial requirement in order to extract each individual original signal.

The non-imaging MIMO-VLC case is further illustrated in Figure 6.1, which shows a 4 × 4 non-imaging MIMO-VLC system. On the other hand, unlike the non-imaging MIMO scheme, in imaging MIMO links, an imaging lens is used in order to image (focus) each transmitted signal from each individual LED into its corresponding PD. In some scenarios (e.g., [31]), the focused signals may fall onto any individual PD or a group of PDs, thus requiring extra signal processing to retrieve each individual original signal. Figure 6.2 illustrates a 4 × 4 imaging MIMO-VLC system.

There have been several research studied investigating optical MIMO system. For instance, in [127], an investigation into both non-imaging and imagining MIMO-VLC approaches was carried out. It was shown that non-imaging optical MIMO links do not perform well when all expected different Rx positions are considered. However, the study demonstrated that optical imaging MIMO links are able to provide an alignment-free high

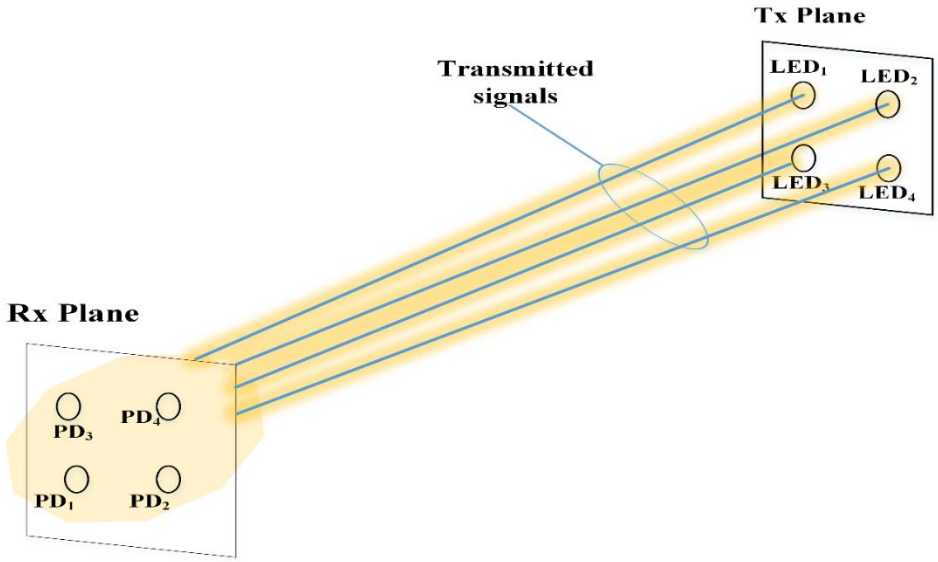

Figure 6.1. An illustration of a 4 × 4 non-imaging-MIMO-VLC system

data throughput for all predictable Rx positions. Moreover, an imaging MIMO-VLC system using micro-LEDs (B_{mod} > 20 MHz) and R_b of ~920 Mb/s over a link span L of 1 m was experimentally demonstrated in [31]. In [128], an experimental 4 × 4 optical non-imaging MIMO-VLC link with an aggregate R_b of 50 Mb/s over L of 2 m was demonstrated.

In this chapter, a 4 × 4 imaging MIMO-VLC system based on *m*-CAP (i.e., a combination of frequency- and space-division multiplexing) is experimentally demonstrated for the first time. Moreover, an investigation of the link's BER performance as a function of m (up to 20) for a range of B_{sig} and L values is presented. In addition, an examination of the net data rate R_{net} and the net spectral efficiency η_{net} is provided, showing that for a given m and L, increasing B_{sig} leads to an increase in R_{net} and a drop in η_{net}. A maximum R_b of ~249 Mb/s at a BER of 3.2×10^{-3} was achieved for m = 20, B_{sig} = 20 MHZ, and L = 1 m.

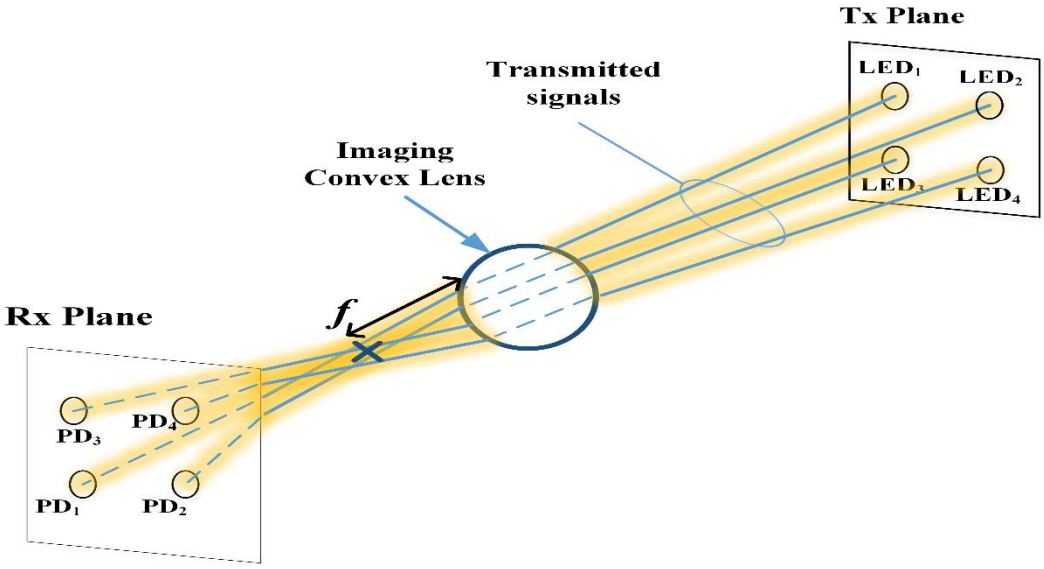

Figure 6.2. An illustration of a 4 × 4 imaging-MIMO-VLC system. Note that, *f* represents the lens focal length

6.2 Experimental Setup of the Imaging MIMO-VLC System

As a proof of concept, Figure 6.3 shows the schematic block diagram of the proposed experimental system, where m independent NRZ PRBS $d_d(t)$ of length 2^{17}-1 were generated in MATLAB. Following serial-to-parallel conversion (S/P), $d_d(t)$ was then mapped onto M-ary QAM (M-QAM) constellation symbols $x_{QAM}(t)$. The $x_{QAM}(t)$ symbols were then up-sampled by n_{samp} samples/symbol, as given in (3.1). β was set to 0.15 for consistency with literature [45, 96]. Both up-sampled signals $d_{I,i}(t)$ and $d_{Q,i}(t)$ of the i^{th} sub-carrier were then passed through the I and Q SRRC filters, the outputs of which are given by [45]:

$$s_{I,f,i}(t) = d_{I,i}(t) \otimes f_{I,i}(t), \tag{6.1}$$

$$s_{Q,f,i}(t) = d_{Q,i}(t) \otimes f_{Q,i}(t), \tag{6.2}$$

where $\otimes$ denotes time domain convolution, $f_{I,i}(t)$ and $f_{Q,i}(t)$ denote the impulse response of the I and Q SRRC filters of the i^{th} sub-carrier, respectively, which are given as in (3.4) and (3.5).

Considering all sub-carriers, the m-CAP output signal can be expressed as [92]:

$$s(t) = s_{I,f}(t) - s_{Q,f}(t). \tag{6.3}$$

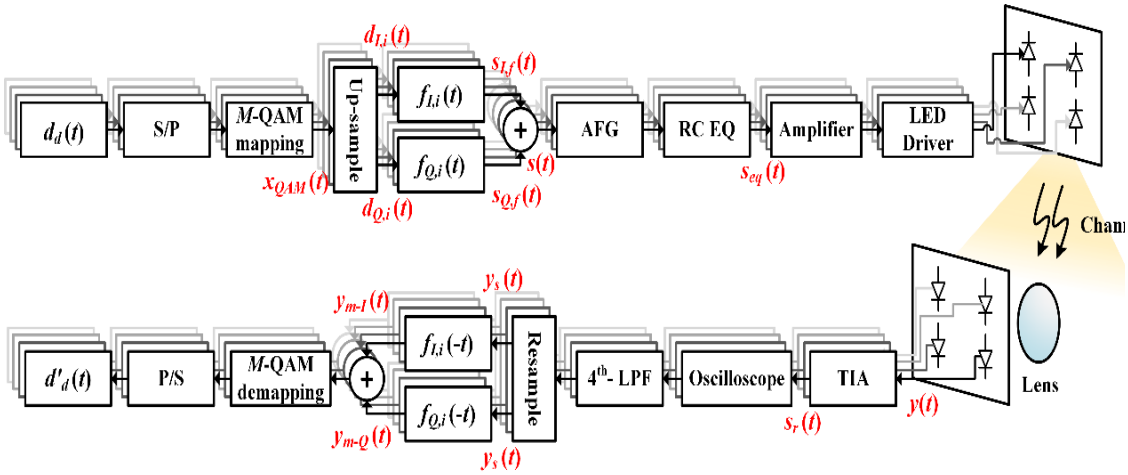

Figure 6.3. The schematic block diagram of the 4 x 4 imaging MIMO *m*-CAP system

The *m*-CAP signal was then applied to identical arbitrary function generators (AFGs) using LabVIEW to generate the signals for the 4 spatial channels. The outputs ($s(t)$) of the four channels were sampled at 2 GS/s with a vertical resolution of 8-bit, and subsequently passed through four independent RC based pre-equalisers (RC EQ) in order to extend B_{mod} from ~2 MHz to 3.8 MHz, as shown in Figure 6.4.

The four equalised signals ($s_{eq}(t)$) were then amplified (with a gain of 5 dB) prior to intensity-modulating the LEDs (4 cool white 565K LUXEON Rebel LEDs) using a bias

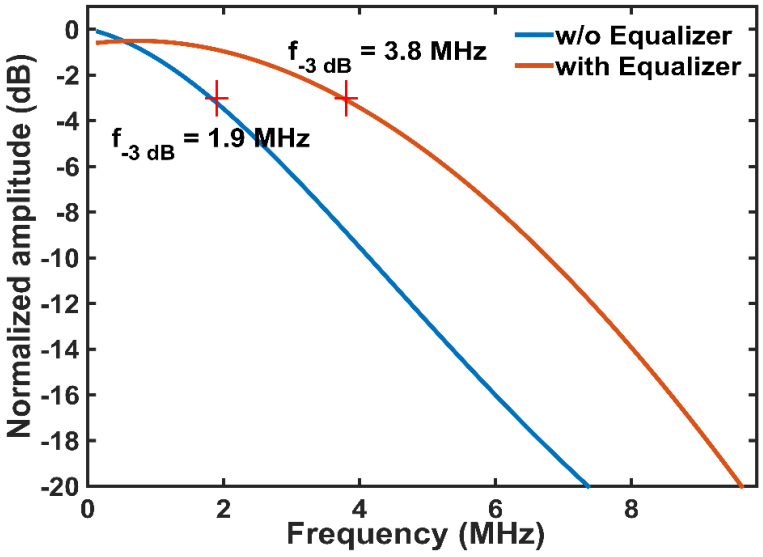

Figure 6.4. LED frequency response with and without an equaliser

tee. Figure 6.5 shows the experimental setup of the proposed system. Note that the distance between the Tx and the lens (L_t), and that between the lens and the Rx (L_r), are given by:

$$L_t = f_l \frac{(\alpha - 1)}{\alpha}, \tag{6.4}$$

$$L_r = f_l(1 - \alpha), \tag{6.5}$$

where f_l is the lens focal length with a magnification factor given by [129]:

$$\alpha = -\frac{d_r}{d_t} = -\frac{L_r}{L_t}, \tag{6.6}$$

where d_r and d_t are the spacing between the Rxs and Txs, respectively.

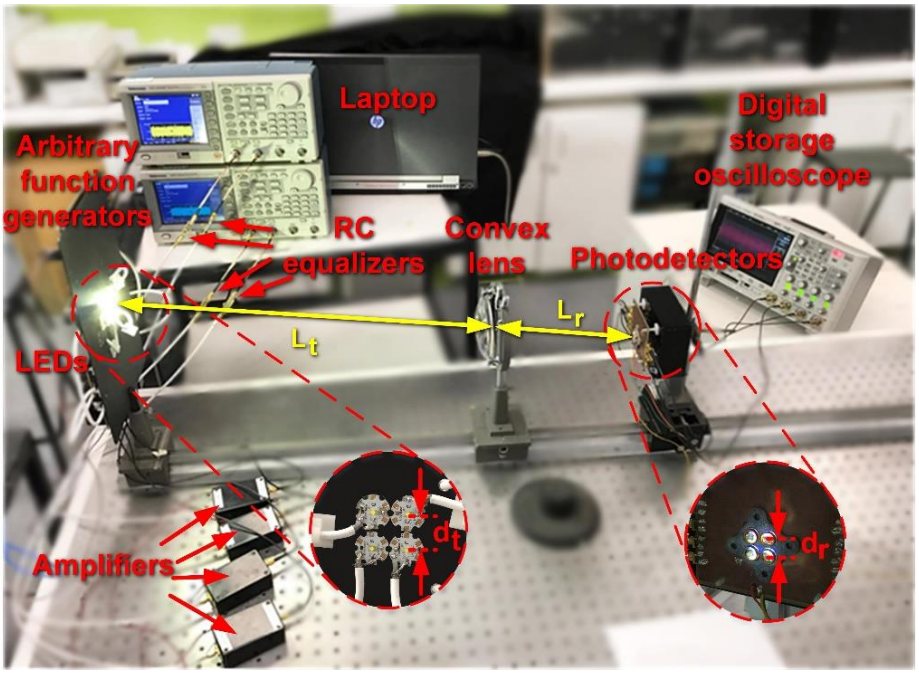

Figure 6.5. The experimental setup of the proposed system. The convex lens is used to focus the LEDs' lights beams onto the PDs. The spacing between the Rxs and Txs is denoted by d_r and d_t, respectively

Table 6.1. Setup and PD parameters

Parameter	**Value**
Data-NRZ pseudorandom binary sequences length	2^{17}-1
Amplifier gain	5 dB
Convex lens • Focal length f_l • Diameter d	 0.25 m, 0.40 m and 1 m 110 mm, 105 mm and 50 mm
LED modulation bandwidth B_{mod}	1.9 MHz
Photodetector - silicon OSD15-5T • Active area • Responsivity $\mathcal{R}$ • Bandwidth B_{PD}	 15 mm^2 0.21 A/W 29 MHz
Spacing between Txs d_t	0.01 m
Spacing between Rxs d_r	0.02 m
Signal bandwidth B_{sig}	5,10,15 and 20 MHz
Transmission span L	~1 m, 1.8 m and 4.5 m

Using the parameters presented in Table 6.1, the total link span $L = L_t + L_r = 4.5f_l$. For f_l of 0.25, 0.4 and 1 m, L is 1.125 m, 1.8 m and 4.5 m, respectively, which are representative dimensions for a typical indoor environment.

As shown in Figure 6.5, at the Rx, a convex lens with a focal length f_l was used to focus the received optical beam of each channel onto its corresponding PD (silicon PD OSD15-5T) with a large enough surfacing area to capture the entire optical foot print. Therefore, with the proposed system being an imagining MIMO system, the lens employed at the Rx ensured that each PD received the optical signal from its corresponding LED. As a result, as in [130], there was no inter-channel crosstalk, unlike in non-imaging MIMO VLC systems, where additional signal processing and filtering are needed to mitigate the channel correlation between individual Txs and Rxs, and the inter-channel crosstalk.[130].

The received signal $y(t)$ is given as in (2.3). Following optoelectronic conversion and amplification using TIAs, the regenerated electrical signals $s_r(t)$ were captured using a digital storage oscilloscope (DSO-X3034A) with a sampling rate of 4 GS/s for off-line

processing as outlined in the following paragraphs. $s_r(t)$ was first passed through a 4th order Butterworth LPF with cut-off frequency $f_{3dB} = B_{sig}$ [45] in order to reject the out-of-band noise. The filtered *m*-CAP signal was then resampled to match the transmitted sampling frequency prior to matched filtering, the output of which is given by:

$$y_{m-I}(t) = y_s(t) \otimes f_{I,i}(-t), \tag{6.7}$$

$$y_{m-Q}(t) = y_s(t) \otimes f_{Q,i}(-t), \tag{6.8}$$

where $y_s(t)$ is the resampled signal and $f_I(-t)$ and $f_Q(-t)$ are the impulse responses of the matched filters.

Following the *M*-QAM demodulation and parallel-to-serial conversion (P/S), the estimated data symbols $d'_{\mathrm{d}}(t)$ were recovered. As reported in the literature, a BPSK based signal was first transmitted on each sub-carrier to measure the EVM, prior to SNR estimation, following the procedures adopted from [110, 111]:

$$\mathrm{SNR}_i = 20\log_{10}\left(\frac{\mathrm{EVM}_{\mathrm{RMS}_i}(\%)}{100}\right). \tag{6.9}$$

Next, a sub-carrier-specific value of b was selected based on the estimated SNR. The proposed system performance was then assessed in terms of (*i*) R_b as a function of *m*; and (*ii*) the assigned *b* versus the order of *m*. Here, a BER target of 10^{-3} was adopted, allowing a margin for the 7% FEC limit, which has a BER limit of 3.8×10^{-3} [113].

The $\mathrm{SNR}_{\mathrm{threshold}}$ for the targeted BER can be found in [124]. Therefore, at the target BER, a set of values for $\mathrm{SNR}_{\mathrm{threshold}}$ of {6.8, 9.8, 16.6, 22.6, 28.5} dB were defined for b = {1, 2, 4, 6, 8}, respectively. Note that the reported net data rate $R_{\mathrm{net}} = \sum_i^N R_{b,i}$, where *N* is number of channels (i.e., 4 in this case) with no 7% FEC overhead. Through sequential isolation of the LEDs, the inter-channel crosstalk was measured to be < 0.2 dB. Therefore, the individual channels can be considered as a SISO link. Following the above procedure,

the *m*-CAP signals were transmitted and the BER was determined by comparing $d'_d(t)$ and $d_d(t)$.

6.3 Results and Discussion

In this section, an experimental evaluation of a 4 × 4 optical imaging MIMO-VLC system utilising the *m*-CAP scheme is presented. The experiment investigated the impact of (*i*) using a range of B_{sig} values while maintaining a fixed *L* of ~1 m; (*ii*) varying the number of sub-carriers *m* up to 20 sub-carriers, for B_{sig} of 5, 10, 15 and 20 MHz, and *L* of ~1 m at the adopted BER target of 10^{-3}; and (*iii*) using a range of *L* and *m* values of ~1, 1.8 and 4.5 m, and $m = \{20, 15, 10, 5\}$ for B_{sig} of 10 MHz.

6.3.1 Varying Signal Bandwidth B_{sig}

Figure 6.6(a) plots R_{net} as a function of *m* for a range of B_{sig} values, *L* of ~1 m and a BER of 10^{-3}. From the results, 20-CAP was found to achieve the highest R_{net} of ~249 Mb/s (the highest reported in this work) at a BER of 3.2×10^{-3} for B_{sig} = 20 MHz, while the value reduced to ~121 Mb/s for B_{sig} = 5 MHz. For B_{sig} of 5 MHz, the increase in R_{net} as a function of *m* was relatively small, since all the sub-carriers had a similar B_{sc}. For B_{sig} of 20 MHz, the drop in R_{net} was due to the reduced B_{sc} for a given *m* and B_{sig}. For example, for *m* = 20 and B_{sig} = 20 MHz, B_{sc} was measured to be 1 MHz, whereas, for *m* = 20 and B_{sig} = 5 MHz, B_{sc} reduced to 0.25 MHz. For B_{sig} of 15 and 10 MHz, R_{net} reached 237.75 Mb/s and 213.49 Mb/s, respectively. Moreover, for higher values of B_{sig} (e.g. 20 MHz) and *m* = 20, the out of band sub-carriers could still be loaded with *b* = 4 starting from the 7th sub-carrier, as shown in Figure 6.6(b), which depicts the assigned *b* values for 20-CAP and for a range of B_{sig} values {20, 15, 10 and 5 MHz}. Using a range of B_{sig} values of 20, 15, 10 and 5 MHz, η_{net} of 12.45, 15.85, 21.34, 24.26 b/s/Hz was measured, respectively,

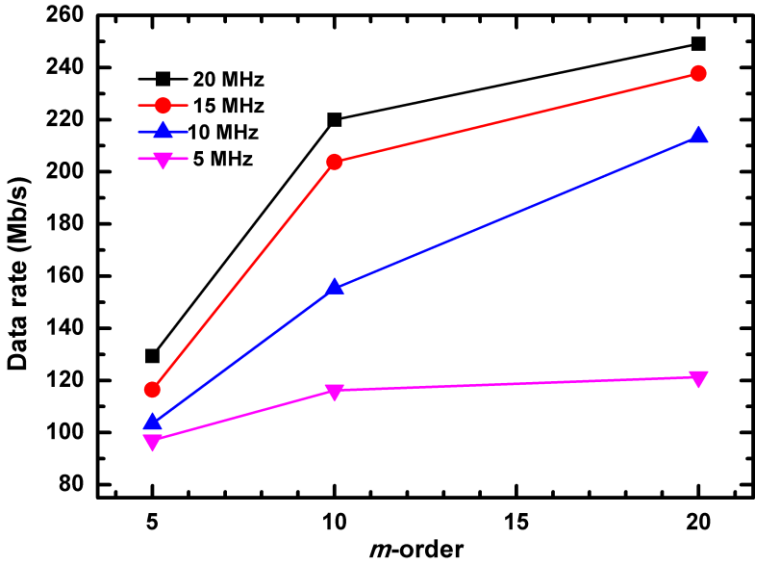

(a)

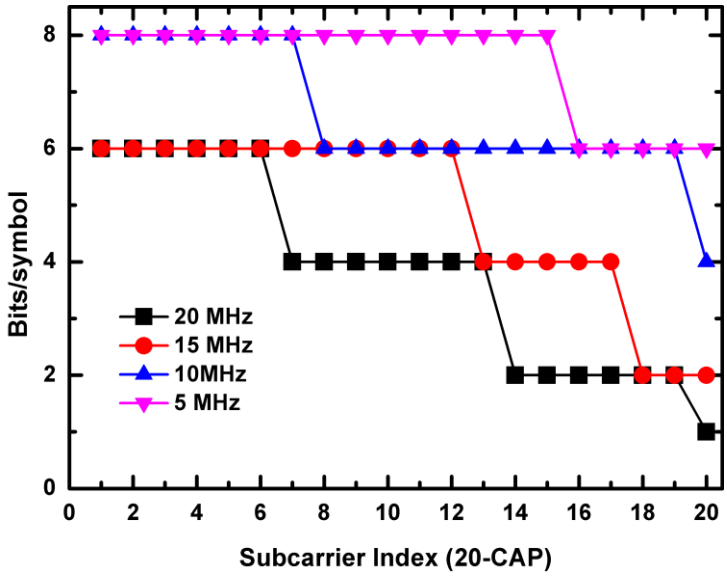

(b)

Figure 6.6. (a) The net data rate R_{net} against m for a range of B_{sig} and a BER of 10^{-3}, and (b) the assigned bits/symbol for 20-CAP for a range of B_{sig} (20, 15, 10 and 5 MHz). Note that in (b), the highest value of b = 8 is assigned for the first 7th and 15th sub-carriers, with B_{sig} of 10 and 5 MHz, respectively, since they are within B_{mod}

for m = 20. This is interesting as it shows that using higher B_{sig} leads to less utilisation of the spectrum, but a higher R_{net}. Moreover, for m = 20 and B_{sig}

of 5, 10 and 15 MHz, an improvement in η_{net} of ~95%, ~72% and ~27% was observed, respectively, compared to m = 20 and B_{sig} of 20 MHz. Hence, there is a trade-off between the achievable R_{net} and spectrum utilisation when considering different values of B_{sig} for

the same *m*-CAP system. This can be attributed to the fact that B_{sc} increases with B_{sig} since the sub-carriers are divided equally, which leads to reducing the SNR of each individual sub-carrier positioned outside the pass-band region (i.e., the 20 dB/decade roll-off region of the LED's LPF response) Therefore, they are assigned with a low *b* value (see Figure 6.6(b)). However, due to the increase in B_{sig}, R_{net} is boosted as it increases proportionally with B_{sig} (i.e., $\frac{1}{T_s}(1+\beta)m$). Moreover, $R_{\mathrm{net}} = \sum_{i=1}^{m} b_i \frac{1}{T_s}$ for all four channels after accounting for the removal of the 7% FEC overhead. In contrast, for a given *m*, decreasing B_{sig} leads to a higher SNR per sub-carrier, which is due to the lower B_{sc} that ensures higher *b* values (Figure 6.6(b)), therefore achieving higher spectral utilisation for a given B_{sig}. In Table 6.2, the results are summarised in a tabular form for simplicity.

Table 6.2. Summary of the achieved R_{net} and η_{net} for a range of B_{sig} and *m*

m \ B_{sig}	**5 MHz**	**10 MHz**	**15 MHz**	**20 MHz**
5	97.03 Mb/s 19.4 b/s/Hz	103.5 Mb/s 10.35 b/s/Hz	116.44 Mb/s 7.76 b/s/Hz	129.39 Mb/s 6.46 b/s/Hz
10	116.25 Mb/s 23.25 b/s/Hz	155.26 Mb/s 15.52 b/s/Hz	203.79 Mb/s 13.58 b/s/Hz	219.96 Mb/s 11 b/s/Hz
20	121.31 Mb/s 24.26 b/s/Hz	213.49 Mb/s 21.34 b/s/Hz	237.75 Mb/s 15.85 b/s/Hz	249.07 Mb/s 12.45 b/s/Hz

In order to demonstrate the performance of SISO under the same conditions as the imaging MIMO, R_{net} is plotted Figure 6.7 for a range of $m = \{20, 15, 10, 5\}$, *L* of ~1 m and a BER target of 10^{-3}, for one of the channels (i.e., Ch1). Note that, as stated earlier, since all four channels in MIMO had the same data rate, each channel could be considered as a SISO link. Figure 6.7 shows that the highest R_{net} that could be supported by SISO

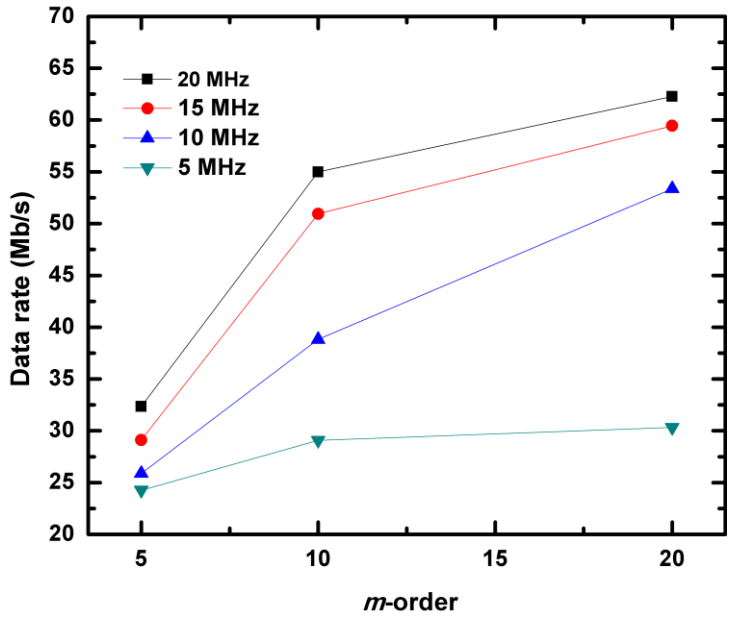

Figure 6.7. R_{net} against m of the SISO system (Ch1) for a range of B_{sig} values

link was 62.26 Mb/s for m = 20 and B_{sig} = 20 MHz. For B_{sig} = 5 MHz, R_{net} dropped to 24.25 Mb/s, which is the lowest value recorded for a SISO link in this work.

A summary of the achieved results for the SISO link for a range of m and B_{sig} values is given in Table 6.3.

Table 6.3. Summary of SISO's achieved R_{net} and η_{net} for a range of B_{sig} and m values

m \ B_{sig}	5 MHz	10 MHz	15 MHz	20 MHz
5	24.25 Mb/s 4.85 b/s/Hz	25.87 Mb/s 2.58 b/s/Hz	29.11 Mb/s 1.94 b/s/Hz	32.34 Mb/s 1.61 b/s/Hz
10	29.06 Mb/s 5.81 b/s/Hz	38.81 Mb/s 3.88 b/s/Hz	50.94 Mb/s 3.39 b/s/Hz	55 Mb/s 2.75 b/s/Hz
20	30.32 Mb/s 6.07 b/s/Hz	53.37 Mb/s 5.33 b/s/Hz	59.43 Mb/s 3.96 b/s/Hz	62.26 Mb/s 3.11 b/s/Hz

Figure 6.8(a) and (b) depict the measured frequency spectrum of the 20-CAP system for B_{sig} of 20 MHz and the corresponding constellation diagrams of the 1st (black), 7th (red), and 14th (green) sub-carriers, respectively. The spectrum in Figure 6.8(a) shows that the first six sub-carriers occupy a bandwidth of 6 MHz. Note that the EVM_{RMS} values for the

three constellations shown were 5.11%, 7.31% and 15.73%, respectively. Figure 6.9 then illustrates the spectral efficiency as a function of m for the range of B_{sig} values. Note that, from Figure 6.6(a), for m = 10 and B_{sig} of 20, 15, 10 and 5 MHz, R_{net} that could be supported was measured to be 219.96, 203.79, 155.26 and 116.25 Mb/s, respectively. This corresponds to η_{net} of 11, 13.58, 15.52 and 23.25 b/s/Hz for the aforementioned B_{sig} values. Moreover, an improved spectral utilisation of ~130%, ~54% and 34.45% for B_{sig} of 5, 10 and 15 MHz, respectively, was obtained in contrast to the B_{sig} of 20 MHz case. For m = 5 and B_{sig} of 20, 15, 10 and 5 MHz, η_{net} values were reduced to 6.46, 7.76, 10.35 and 19.4 b/s/Hz, respectively. Alternatively, for B_{sig} of 5, 10, and 15 MHz and m of 5, an improvement in the spectrum utilisation of 203% ~60% and ~74% was recorded compared to the B_{sig} of 20 MHz case.

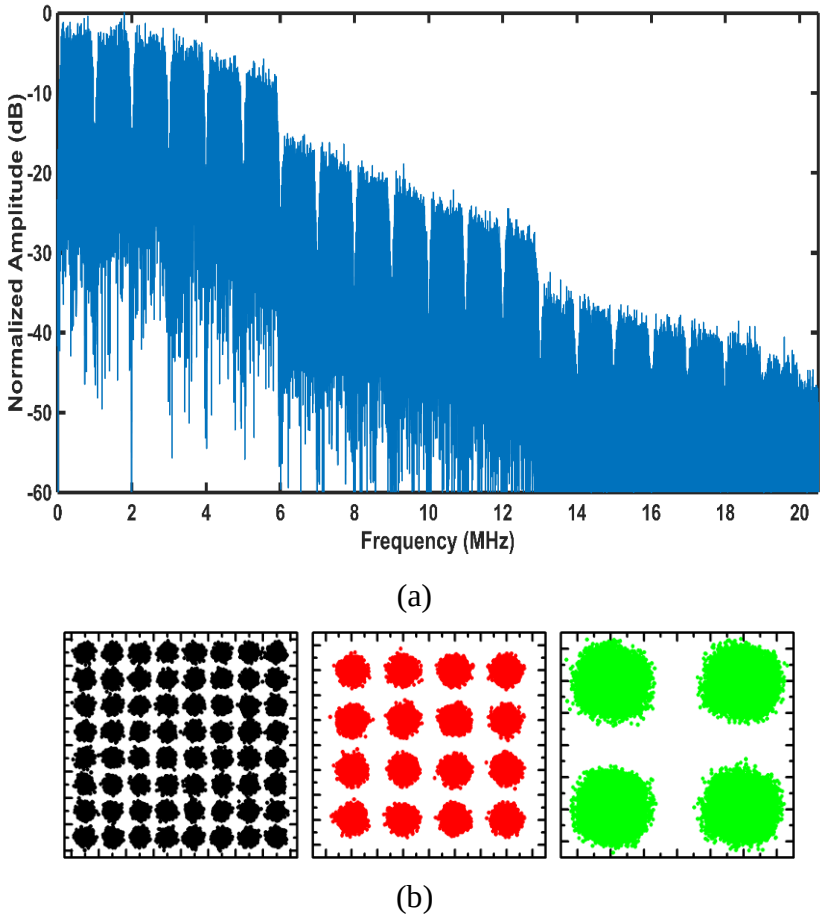

Figure 6.8. 20-CAP with B_{sig} of 20 MHz; (a) the measured frequency spectrum, and (b) constellation diagrams for the 1st, 7th and 14th sub-carriers

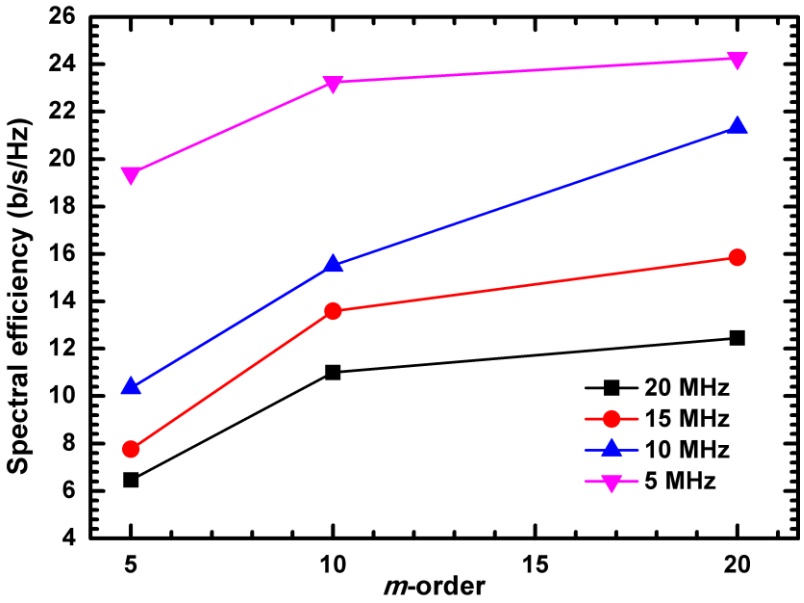

Figure 6.9. The spectral efficiency against m for a range of B_{sig} {20, 15, 10 and 5 MHz}

At this stage, it is worth mentioning that by combining both the space multiplexing (MIMO) and frequency multiplexing (m-CAP) schemes, the overall system transmission speed was improved by ~8 times, from 31.53 Mb/s to ~249 Mb/s, in contrast to the results reported in [45]. To the best of the author's knowledge, this is the only experimental work demonstrating the implementation of m-CAP (up to 10) in the VLC domain reported in the literature. While L was kept at ~1 m in this work, B_{sig} was increased by ~3 times, which is higher than the 6.5 MHz value reported in [45]. It should be noted that the aim of this work is not to achieve the highest R_{net} value, but to demonstrate the possible gain that can be achieved by combining the space and frequency multiplexing schemes.

Moreover, in order to increase R_{net}, the m-order was doubled to 20, but at the cost of increasing the computational complexity of the overall system, since for every increment in m, two additional pulse shaping FIR filters (i.e., one each for I and Q) are required at both the Tx and the Rx. Note that increasing m from 10 to 20, leads to increasing the number of convolution operations from 480 to 1840 at the Tx. For the m-CAP MIMO-VLC system with m = 10, R_{net} was increased to 213.49 Mb/s compared to the 31.53 Mb/s

figure reported in [45] (i.e., a factor of 6.77), over the same L of 1 m. Increasing B_{sig} to 10 MHz resulted in increasing η_{net} by a factor of 4.4, as the obtained η_{net} was 21.34 b/s/Hz compared to 4.85 b/s/Hz in [45], which is a considerable gain in the context of VLC systems.

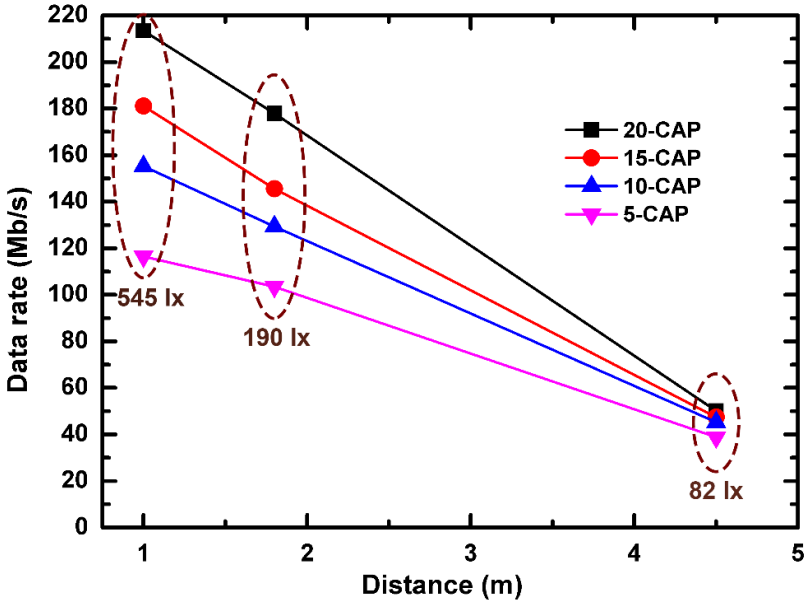

Figure 6.10. The measured net data rate R_{net} as a function of the transmission distance for B_{sig} of 10 MHz and a range of m-CAPs. Illuminance values at the Rx for the tested transmission distances are also labelled in the figure

6.3.2 **Extending the Transmission Span *L***

Figure 6.10 illustrates R_{net} as a function of L for a range of $m = \{20, 15, 10, 5\}$ and B_{sig} of 10 MHz. In addition, the illuminance values at the Rx for the targeted L are also depicted in the figure. As expected, the illuminance value dropped as L increased. Illuminance values of 545, 190 and 82 lx were recorded for L = ~1, 1.8 and 4.5 m, respectively. In addition, as expected, increasing L from 1 to 4.5 m resulted in reducing R_{net} from 213 Mb/s to approximately 50 Mb/s for 20-CAP. This thus resulted in η_{net} of 21.35 b/s/Hz and 5 b/s/Hz for the BER values of 1.2×10^{-3} and 3.7×10^{-3}, respectively. For $m = \{20, 15, 10, 5\}$ and L of ~1 m, R_{net} values of 213.49, 181.14, 155.26 and 116.44 Mb/s

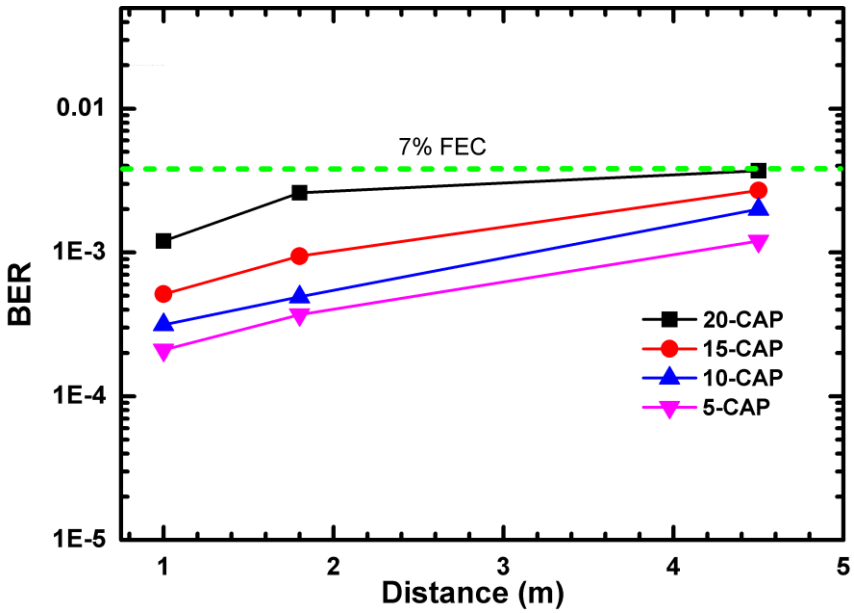

Figure 6.11. The measured BER as a function of distance for different values of *m*. Also included is the 7% FEC limit (dashed green line)

were recorded, respectively; where the corresponding values of η_{net} were 21.35, 18.11, 15.52 and 11.64 b/s/Hz. Finally, Figure 6.11 depicts the achievable BER performance as a function of *L* for a range of *m* values. As expected, the BER increased with *L* and *m*, reaching 3.7×10^{-3}, which is still below the 7% FEC limit of 3.8×10^{-3}, for $m = 20$ and *L* of 4.5 m.

By extending *L* to 1.8 m, R_{net} dropped to 177.9, 145.56, 129.39 and 103.5 Mb/s, respectively, for $m = \{20, 15, 10, 5\}$ (Figure 6.10), corresponding to a reduction in η_{net} of 17.79, 14.55, 12.94 and 10.35 b/s/Hz. The highest BER achieved for *L* of 1.8 m was 2.6×10^{-3} at $m = 20$ (see Figure 6.11); following the same upward trend as in *m* and *L*.

For the largest *L* value of 4.5 m, R_{net} reduced (refer to Figure 6.10) compared to the shorter distances, with values of 50.13, 47.43, 45.28 and 38.81 Mb/s at $m = \{20, 15, 10, 5\}$, respectively. Similar values of R_{net} were observed for lower values of *b* for each sub-carrier. In other words, the bit loading algorithm failed to introduce any improvement in the overall R_{net}, as a result of all sub-carriers having low SNR values (i.e., $\ll$16.6 dB;

which is the $SNR_{threshold}$ at $b = 4$). Furthermore, a reduction in the spectral efficiency was observed, as it fell below 5 b/s/Hz for the first time in this work.

Table 6.4 presents a tabular summary of the achieved R_{net} and η_{net} results for a set of L and m values.

Table 6.4. Summary of the achieved R_{net} and η_{net} for a range of L and m values

m \ ***L***	**~1 m**	**1.8 m**	**4.5 m**
5	116.44 Mb/s 11.64 b/s/Hz	103.5 Mb/s 10.35 b/s/Hz	38.81 Mb/s 3.88 b/s/Hz
10	155.26 Mb/s 15.52 b/s/Hz	129.39 Mb/s 12.94 b/s/Hz	45.28 Mb/s 4.52 b/s/Hz
15	181.14 Mb/s 18.11 b/s/Hz	145.56 Mb/s 14.55 b/s/Hz	47.43 Mb/s 4.74 b/s/Hz
20	213.49 Mb/s 21.35 b/s/Hz	177.9 Mb/s 17.79 b/s/Hz	50.13 Mb/s 5 b/s/Hz

6.4 Summary

This chapter presented an experimental evaluation of the performance of a 4 × 4 imaging MIMO-VLC system (i.e., space multiplexing) utilising the *m*-CAP scheme (i.e., frequency multiplexing) for a range of system parameters (i.e., m, B_{sig} and L). It was shown that by combing the two multiplexing schemes, a maximum R_b of ~249 Mb/s was achieved for $m = 20$, $B_{sig} = 20$ MHz, and $L = 1$ m, at a BER of 3.2×10^{-3}, utilising LEDs with ~4 MHz bandwidth. In addition, it was shown that for a given value of m and L, increasing B_{sig} resulted in substantially increasing R_{net}. However, η_{net} was found to reduce as a result, thus requiring a trade-off between R_{net} and η_{net} to be taken into account. Furthermore, it was observed that increasing L resulted in a reduction in R_{net}. More interestingly, for the largest distance of $L = 4.5$ m, increasing m did not introduce any

significant improvement in the system performance, but increased the computational complexity by the way of increasing the number of the pulse shaping FIR filters required.

Chapter 7 CONCLUSIONS AND FUTURE WORK

7.1 Conclusions

The main aim of this research was to address the limitations of VLC systems imposed mainly by the limited bandwidths of LEDs, which represents the main bottleneck towards implementing a high data throughput VLC-based infrastructure. This aim has been achieved by introducing a novel and promising modulation scheme (i.e., *m*-CAP) within the context of VLC technology, and investigating the potential performance improvement offered by the new scheme to VLC systems. The results of the research have demonstrated that the *m*-CAP scheme is a very promising candidate for improving the VLC system data throughput. Furthermore, dividing the available CAP B_{sig} into *m*-sub-carriers has been shown to result in making the frequency attenuation over these small sub-carriers less than that over the entire bandwidth, thus resulting in a higher SNR and a lower error rate.

This thesis opened with an introduction chapter, which highlighted the technical challenges, motivations behind conducting this study and the contributions to knowledge. Following this, Chapter two provided the fundamentals of VLC systems, including the Tx structure, channel model classification and the Rx structure. Moreover, the main source of noise in a VLC system was highlighted and discussed. This chapter also highlighted the most popular single-carrier and multi-carrier modulation schemes used in

VLC systems (i.e., OOK, PPM, PAM, PWM, QAM, CAP, and OFDM). In order to be able to carry out the objectives of this study, the fundamental principles of the proposed *m*-CAP scheme were outlined in Chapter Three. The chapter also presented a block diagram of the scheme along with a detailed explanation of the *m*-CAP signals generation process. In addition, for the first time in VLC, an experimental work utilising the *m*-CAP scheme was demonstrated for a transmission distance of 1 m. It was experimentally shown that the throughput of a fixed 6.5 MHz *m*-CAP system could be increased up to ~31.5 Mb/s with an η_s of 4.85 b/s/Hz by increasing the number of sub-carriers to $m = 10$. Furthermore, it was revealed that increasing the *m*-CAP order led to a reduction in the individual sub-carrier's bandwidth, which contributed towards gaining a substantial increase in R_{net}/η_{net} by allowing the implementation of the bit-loading technique. Moreover, increasing the number of sub-carriers within the set $m = \{1, 2, 4, 6, 8, 10\}$ over a fixed B_{tot} of 6.5 MHz, resulted in transmission speeds (spectral efficiencies) of 9.04 (1.4), 15.78 (2.43), 23.62 (3.63), 25.4 (3.9), 30.88 (4.75) and 31.53 (4.85) Mb/s (b/s/Hz) for the aforementioned values of *m*, respectively.

Chapter Four presented numerical simulations demonstrating the principles of implementing the *m*-CAP scheme enhanced by DFE for different *m*-CAP orders ($m = \{1, 2, 5, 10\}$). It was shown that employing DFE helped to improve the BER performance of the tested *m*-CAP {1, 2}; thanks to its ability to cancel the severe ISI imposed by the limited bandwidth of the LED-based VLC system. However, due to the inherent ability of *m*-CAP in improving the BER performance when increasing the order of $m = \{5, 10\}$, applying the DFE failed to introduce any noticeable improvement. Therefore, depending on the required application, applying equalisation to an *m*-CAP system can in some cases add an unnecessary extra complexity to the system. This chapter also highlighted the impact of tuning the values of the L_f and β parameters of the FIR filters utilised in the *m*-CAP scheme on the BER performance of VLC systems for a range of $m = \{2, 5, 10\}$.

Both parameters demonstrated a huge impact on the BER performance. Moreover, it was proven that deploying $L_f > 12$ symbols is to be avoided since it does not improve the BER performance, but induce more computational complexity by increasing the number of FIR filter taps. In addition, a further investigation of the impact of the aforementioned FIR filter parameters on R_b and η_s of VLC systems was carried out in the laboratory, whereby the achieved results showed that low order *m*-CAP links (e.g., 6-CAP) could be adopted to provide a similar R_b and η_s performance to that of higher order *m*-CAP systems, while offering much lower computational complexity as a result of requiring fewer filter taps.

In Chapter Five, a novel implementation of the *m*-CAP system was introduced. The new *m*-CAP concept is based on making the first sub-carrier bandwidth the same as B_{mod}, and sharing the remaining bandwidth equally between the *m*-1 sub-carriers. The study conducted revealed that by deploying the new *m*-CAP scheme at a designated BER of 10^{-4}, the performance of the first sub-carrier of high order *m*-CAP links (m = 10, 8, and 6) achieved an E_b/N_0 of 15.5 dB at a power penalty of ~1.5 dB compared with the average performance of the first five, four and three sub-carriers in the conventional 10, 8, and 6-CAP systems, respectively. Furthermore, for the new 4-CAP link, the performance of the first sub-carrier showed a power penalty of ~1 dB when compared with the average performance of the first two sub-carriers of the conventional 4-CAP system. Moreover, it was shown that by deploying the proposed 10, 8, 6 and 4-CAP links, a reduction in the computational complexity of 80%, 75%, ~67% and 50% was achieved compared to the conventional 10, 8, 6 and 4 CAP systems, respectively. In addition, the impact of variably allocating different bandwidths for the sub-carriers on the R_b performance was investigated. The sub-carriers were variably distributed so that *x* sub-carriers were located within the LED's B_{mod} region, and the remaining sub-carriers (i.e., $y = m\text{-}x$) were equally divided among the remaining part of B_{tot}. The new variable $m_{x/y}$-CAP system showed an average and maximum improvement in R_b of up to ~30% and ~36%, respectively, for the

$6_{1/5}$-CAP system in comparison to the conventional 6-CAP system. Based on the results, it was also revealed that an improvement in the R_b performance was attainable even for a very band-limited VLC link (i.e., $B_{mod} = 0.2B_{tot}$) by increasing the $m_{x/y}$-CAP order.

Chapter Six reported, for the first time, an investigation of the performance of a 4 × 4 *m*-CAP imaging MIMO (i.e., frequency and space multiplexing) VLC link considering a range of system parameters. By combining the two schemes (i.e., frequency and space multiplexing), an improvement in the transmission speed was experimentally demonstrated, where a maximum value of ~249 Mb/s was reached. It was also shown that there is a trade-off between R_{net} and η_{net}, since for a given value of *m* and *L*, increasing B_{sig} resulted in substantially improving R_{net}, while, interestingly, η_{net} reduced as a result. Moreover, the highest R_{net} of 249.07 Mb/s was achieved at a BER (i.e., 3.2×10^{-3}) for B_{sig} of 20 MHz and m = 20 over a transmission span of ~1 m. On the other hand, for lower B_{sig} of 5 MHz and m = 20, the achieved R_{net} reduced to 121.21 Mb/s, but the spectrum utilisation was almost 95% better in contrast to the B_{sig} =20 MHz case. It was also observed that for a given value of *m* and B_{sig}, increasing the distance resulted in reducing R_{net}. The overall R_{net} (η_{net}) for the proposed system (i.e., four channels) was measured to be 213.49 Mb/s (21.35 b/s/Hz), 177.9 Mb/s (17.79 b/s/Hz), and 50.13 Mb/s (5.01 b/s/Hz) for m = 20 and the B_{sig} of 10 MHz over a range of *L* (i.e., ~1 m, 1.8 m and 4.5 m), respectively, at BER values of 1.2×10^{-3}, 2.6×10^{-3}, and 3.7×10^{-3}. Finally, it was shown that for the highest *L* of 4.5 m, increasing *m* did not introduce any significant improvement in the system performance, but increased the computational complexity by the way of increasing the number of pulse shaping FIR filters.

In conclusion, this thesis has investigated a new modulation scheme, known as *m*-CAP, by modifying the existing CAP modulation scheme. The *m*-CAP scheme was experimentally demonstrated to be a feasible solution for achieving high R_b in the band-

limited VLC systems. In addition, coupling DFE with high order *m*-CAP (i.e., *m* = {5, 10}) was shown to be impractical, as it did not provide any BER improvement to the system, thus demonstrating the intrinsic ability of *m*-CAP in mitigating ISI. Furthermore. The new *m*-CAP concept is advantages in that a huge reduction in the computational complexity can be achieved at the cost of paying a BER penalty of ~1.5 dB. Finally, an experimental 4 × 4 *m*-CAP imaging MIMO-VLC link was implemented and investigated, showing an aggregate R_b of ~249 Mb/s at a BER of 3.2×10^{-3}, for B_{sig} of 20 MHz and *m* = 20, over *L* of ~1, utilising LEDs with ~4 MHz B_{mod}.

7.2 **Recommendations for Future Work**

Even though the objectives stated in Chapter One have been accomplished, the following future work is recommended in order to extend the work reported in this thesis.

FPGA implementation: Implementing *m*-CAP in a full online real system such as an FPGA is a straightforward progression of the work reported in this thesis. As the main challenge of implementing *m*-CAP is the computational complexity introduced by the utilised number of pulse shaping FIR filters, implementing *m*-CAP in systems with a limited integration density (i.e., FPGA) could potentially further prove the suitability and viability of the scheme.

PAPR reduction: In addition to the limited bandwidth induced by the LEDs utilised in VLC systems, LEDs-induced nonlinearities also pose a further challenge for VLC systems. These nonlinearities are caused as a result of the limited dynamic range of the LEDs, and become critical when implementing a very high PAPR modulation scheme such as OFDM, as such a phenomenon leads to a clipping in the transmitted signals, which results in lower SNR and higher BER levels. Within this context, *m*-CAP is not immune to this phenomenon, as it does suffer from high PAPR levels. Thus, as an emerging

scheme, it will be interesting to investigate how severe the impact of PAPR is on the performance of *m*-CAP in contrast to other famous modulation schemes (e.g., OFDM), and the possible solutions to such an issue.

Comparison with OFDM: The OFDM scheme has been extensively investigated in VLC systems, with results showing an achievable R_b of several Gb/s reported in literature. On the other hand, CAP has been shown to outperform OFDM in terms of R_b over the same physical link. Thus, interesting findings can be expected from comparing *m*-CAP and OFDM over the same physical link and investigating the computational complexity of both schemes.

References

[1] Z. Ghassemlooy, W. Popoola, and S. Rajbhandari, *Optical wireless communications: system and channel modelling with Matlab®*. CRC Press, 2012.

[2] A. G. Bell, "On the production and reproduction of sound by light," *American journal of science*, no. 118, pp. 305-324, 1880.

[3] T. M. Okon and J. R. Biard, "The first practical LED," *Edison Tech Center*, pp. 1-14, 2015.

[4] N. Holonyak Jr and S. Bevacqua, "Coherent (visible) light emission from Ga (As1− xPx) junctions," *Applied Physics Letters*, vol. 1, no. 4, pp. 82-83, 1962.

[5] S. P. Denbaars, "Gallium-Nitride-based materials for blue to ultraviolet optoelectronics devices," *Proceedings of the IEEE*, vol. 85, no. 11, pp. 1740-1749, 1997.

[6] S. Nakamura, T. Mukai, and M. Senoh, "Candela-class high-brightness InGaN/AlGaN double-heterostructure blue-light-emitting diodes," *Applied Physics Letters*, vol. 64, no. 13, pp. 1687-1689, 1994.

[7] R. Mueller-Mach, G. O. Mueller, M. R. Krames, and T. Trottier, "High-power phosphor-converted light-emitting diodes based on III-Nitrides," *IEEE Journal of Selected Topics in Quantum Electronics*, vol. 8, no. 2, pp. 339-345, 2002.

[8] C. M. Bourget, "An introduction to light-emitting diodes," *HortScience*, vol. 43, no. 7, pp. 1944-1946, 2008.

[9] Y. Tanaka, T. Komine, S. Haruyama, and M. Nakagawa, "Indoor visible light data transmission system utilizing white LED lights," *IEICE transactions on communications*, vol. 86, no. 8, pp. 2440-2454, 2003.

[10] A. Eslami, S. Vangala, and H. Pishro-Nik, "Hybrid channel codes for efficient FSO/RF communication systems," *IEEE Transactions on Communications*, vol. 58, no. 10, pp. 2926-2938, 2010.

[11] H. Haas, "High-speed wireless networking using visible light," *SPIE Newsroom*, vol. 1, pp. 1-3, 2013.

[12] P. A. Haigh, Z. Ghassemlooy, S. Rajbhandari, and I. Papakonstantinou, "Visible light communications using organic light emitting diodes," *Communications Magazine, IEEE*, vol. 51, no. 8, pp. 148-154, 2013.

[13] J. Song *et al.*, "Indoor hospital communication systems: An integrated solution based on power line and visible light communication," in *2014 IEEE Faible Tension Faible Consommation*, 2014, pp. 1-6.

[14] Z. Ghassemlooy, L. N. Alves, S. Zvanovec, and M. A. Khalighi, *Visible light communications: Theory and applications*. Boca Raton: CRC Press, 2017.

[15] D. Karunatilaka, F. Zafar, V. Kalavally, and R. Parthiban, "LED based indoor visible light communications: State of the art," *IEEE Communications Surveys & Tutorials*, vol. 17, no. 3, pp. 1649-1678, 2015.

[16] K. Cui, G. Chen, Z. Xu, and R. D. Roberts, "Line-of-sight visible light communication system design and demonstration," in *2010 7th International Symposium on Communication Systems, Networks & Digital Signal Processing (CSNDSP 2010)*, 2010, pp. 621-625.

[17] X. Wu, M. Safari, and H. Haas, "Access point selection for hybrid Li-Fi and Wi-Fi networks," *IEEE Transactions on Communications*, vol. PP, no. 99, pp. 1-1, 2017.

[18] -, "Cisco visual networking index: global mobile data traffic forecast update, 2015–2020, white paper," ed, 2016.

[19] S. Wu, H. Wang, and C. H. Youn, "Visible light communications for 5G wireless networking systems: from fixed to mobile communications," *IEEE Network*, vol. 28, no. 6, pp. 41-45, 2014.

[20] H. Burchardt, N. Serafimovski, D. Tsonev, S. Videv, and H. Haas, "VLC: Beyond point-to-point communication," *IEEE Communications Magazine*, vol. 52, no. 7, pp. 98-105, 2014.

[21] EUROCONTROL. (21/09/2017). *Spectrum management, a military perspective*. Available: https://www.eurocontrol.int/articles/spectrum-management-military

[22] K. Yao, N. Wu, X. Wang, X. Gai, and H. Feng, "A novel power efficient modulation scheme for VLC systems," in *2016 IEEE/CIC International Conference on Communications in China (ICCC)*, 2016, pp. 1-6.

[23] S. S. Saab and K. K. Saab, "A positioning system for photodiode device using collocated LEDs," *IEEE Photonics Journal*, vol. 8, no. 5, pp. 1-14, 2016.

[24] S. Buzzi, I. C. L, T. E. Klein, H. V. Poor, C. Yang, and A. Zappone, "A Survey of Energy-Efficient Techniques for 5G Networks and Challenges Ahead," *IEEE Journal on Selected Areas in Communications*, vol. 34, no. 4, pp. 697-709, 2016.

[25] K. Warmerdam, A. Pandharipande, D. Caicedo, and M. Zuniga, "Visible Light Communications for Sensing and Lighting Control," *IEEE Sensors Journal*, vol. 16, no. 17, pp. 6718-6726, 2016.

[26] S. Ahamed, "Visible light communication in railways," in *The International Conference on Railway Engineering (ICRE) 2016*, 2016, pp. 1-5.

[27] L. Hanzo, H. Haas, S. Imre, D. O'Brien, M. Rupp, and L. Gyongyosi, "Wireless myths, realities, and futures: from 3G/4G to optical and quantum wireless," *Proceedings of the IEEE*, vol. 100, no. Special Centennial Issue, pp. 1853-1888, 2012.

[28] A. M. Khalid, G. Cossu, R. Corsini, P. Choudhury, and E. Ciaramella, "1-Gb/s Transmission over a phosphorescent white LED by using rate-adaptive discrete multitone modulation," *IEEE Photonics Journal*, vol. 4, no. 5, pp. 1465-1473, 2012.

[29] P. A. Haigh *et al.*, "Exploiting equalization techniques for improving data rates in organic optoelectronic devices for visible light communications," *Journal of Lightwave Technology,* vol. 30, no. 19, pp. 3081-3088, 2012.

[30] Z. Ghassemlooy, Popoola, W.& Rajbhandari, S., " Optical Wireless Communications: System and Channel Modelling with MATLAB," 2013.

[31] S. Rajbhandari *et al.*, "Imaging-MIMO visible light communication system using μLEDs and integrated receiver," in *2014 IEEE Globecom Workshops (GC Wkshps)*, 2014, pp. 536-540.

[32] Z. Ghassemlooy, S. Arnon, M. Uysal, Z. Xu, and J. Cheng, "Emerging optical wireless communications-advances and challenges," *IEEE Journal on Selected Areas in Communications,* vol. 33, no. 9, pp. 1738-1749, 2015.

[33] A. Halder and A. D. Barman, "Nonlinear compensation of LEDs for improved performance in CSK based indoor visible light communication," in *2015 6th International Conference on Computers and Devices for Communication (CODEC)*, 2015, pp. 1-4.

[34] H. L. Minh *et al.*, "100-Mb/s NRZ Visible Light Communications Using a Postequalized White LED," *IEEE Photonics Technology Letters,* vol. 21, no. 15, pp. 1063-1065, 2009.

[35] P. A. Haigh, Z. Ghassemlooy, S. Rajbhandari, I. Papakonstantinou, and W. Popoola, "Visible light communications: 170 Mb/s using an artificial neural network equalizer in a low bandwidth white light configuration," *Journal of Lightwave Technology,* vol. 32, no. 9, pp. 1807-1813, 2014.

[36] L. Grobe *et al.*, "High-speed visible light communication systems," *IEEE Communications Magazine,* vol. 51, no. 12, pp. 60-66, 2013.

[37] C. L. Liao, Y. F. Chang, C. L. Ho, and M. C. Wu, "High-speed GaN-based blue light-emitting diodes with Gallium-doped ZnO current spreading layer," *IEEE Electron Device Letters,* vol. 34, no. 5, pp. 611-613, 2013.

[38] D. Tsonev *et al.*, "A 3-Gb/s single-LED OFDM-based wireless VLC link using a Gallium Nitride μLED," *IEEE Photonics Technology Letters,* vol. 26, no. 7, pp. 637-640, 2014.

[39] P. A. Haigh *et al.*, "A 20-Mb/s VLC link with a polymer LED and a multilayer perceptron equalizer," *IEEE Photonics Technology Letters,* vol. 26, no. 19, pp. 1975-1978, 2014.

[40] J.-Y. Sung, C.-W. Chow, and C.-H. Yeh, "Is blue optical filter necessary in high speed phosphor-based white light LED visible light communications?," *Optics express,* vol. 22, no. 17, pp. 20646-20651, 2014.

[41] S. W. Wang *et al.*, "A high-performance blue filter for a white-LED-based visible light communication system," *IEEE Wireless Communications,* vol. 22, no. 2, pp. 61-67, 2015.

[42] W. O. Popoola and H. Haas, "Demonstration of the merit and limitation of generalised space shift keying for indoor visible light communications," *Journal of Lightwave Technology,* vol. 32, no. 10, pp. 1960-1965, 2014.

[43] H. L. Minh *et al.*, "100-Mb/s NRZ visible light communications using a postequalized white LED," *IEEE Photonics Technology Letters,* vol. 21, no. 15, pp. 1063-1065, 2009.

[44] J. Armstrong, "OFDM for optical communications," *Journal of Lightwave Technology,* vol. 27, no. 3, pp. 189-204, 2009.

[45] P. A. Haigh *et al.*, "A multi-CAP visible light communications system with 4.85 b/s/Hz spectral efficiency," *IEEE Journal on Selected Areas in Communications,* vol. 33, no. 99, pp. 1771-1779, 2015.

[46] G. Cossu, A. Wajahat, R. Corsini, and E. Ciaramella, "5.6 Gbit/s downlink and 1.5 Gbit/s uplink optical wireless transmission at indoor distances (≥ 1.5 m)," in *Optical Communication (ECOC), 2014 European Conference on*, 2014, pp. 1-3.

[47] F. M. Wu *et al.*, "Performance comparison of OFDM signal and CAP signal over high capacity RGB-LED-based WDM visible light communication," *IEEE Photonics Journal* vol. 5, no. 4, pp. 7901507-7901507, 2013.

[48] D. Bykhovsky and S. Arnon, "An experimental comparison of different bit-and-power-allocation algorithms for DCO-OFDM," *Journal of Lightwave Technology,* vol. 32, no. 8, pp. 1559-1564, Apr 15 2014.

[49] L. Chen, B. Krongold, and J. Evans, "Theoretical characterization of nonlinear clipping effects in IM/DD optical OFDM systems," *IEEE Transactions on Communications,* vol. 60, no. 8, pp. 2304-2312, 2012.

[50] H. Ochiai and H. Imai, "Performance analysis of deliberately clipped OFDM signals," *IEEE Transactions on Communications,* vol. 50, no. 1, pp. 89-101, 2002.

[51] T. Jiang and Y. Wu, "An overview: peak-to-average power ratio reduction techniques for OFDM signals," *IEEE Transactions on Broadcasting,* vol. 54, no. 2, pp. 257-268, 2008.

[52] C. X. Wang *et al.*, "Cellular architecture and key technologies for 5G wireless communication networks," *IEEE Communications Magazine,* vol. 52, no. 2, pp. 122-130, 2014.

[53] S. Zvanovec, P. Chvojka, P. A. Haigh, and Z. Ghassemlooy, "Visible light communications towards 5G," *Radioengineering,* vol. 24, no. 1, pp. 1-9, 2015.

[54] M. Yasir, H. Siu-Wai, and B. N. Vellambi, "Indoor positioning system using visible light and accelerometer," *Lightwave Technology, Journal of,* vol. 32, no. 19, pp. 3306-3316, 2014.

[55] C. Yew-Kiat, N. Xiao-Wei, and C. Wan-Young, "Hazardless biomedical sensing data transmission using VLC," *Sensors Journal, IEEE,* vol. 13, no. 9, pp. 3347-3348, 2013.

[56] Y. Tanaka, S. Haruyama, and M. Nakagawa, "Wireless optical transmissions with white colored LED for wireless home links," in *Personal, Indoor and Mobile Radio Communications, 2000. PIMRC 2000. The 11th IEEE International Symposium on*, 2000, vol. 2, pp. 1325-1329: IEEE.

[57] OMEGA. (04/09/2017). *European home gigabit access project*. Available: http://www.ict-omega.eu

[58] S. Nishimoto, T. Yamazato, H. Okada, T. Fujii, T. Yendo, and S. Arai, "High-speed transmission of overlay coding for road-to-vehicle visible light communication using LED array and high-speed camera," in *Globecom Workshops (GC Wkshps), 2012 IEEE*, 2012, pp. 1234-1238: IEEE.

[59] M. Uysal, Z. Ghassemlooy, A. Bekkali, A. Kadri, and H. Menouar, "Visible light communication for vehicular networking: performance study of a V2V system

using a measured headlamp beam pattern model," *IEEE Vehicular Technology Magazine*, vol. 10, no. 4, pp. 45-53, 2015.

[60] M. D. Higgins, R. J. Green, and M. S. Leeson, "Optical wireless for intravehicle communications: A channel viability analysis," *IEEE Transactions on Vehicular Technology*, vol. 61, no. 1, pp. 123-129, 2012.

[61] D. O'Brien, G. Faulkner, S. Zikic, and N. Schmitt, "High data-rate optical wireless communications in passenger aircraft: Measurements and simulations," in *Communication Systems, Networks and Digital Signal Processing, 2008. CNSDSP 2008. 6th International Symposium on*, 2008, pp. 68-71: IEEE.

[62] I. Association, "IEEE standard for local and metropolitan area networks-Part 15.7: short-range wireless optical communication using visible light," *IEEE Std*, vol. 802, pp. 7-2011, 2011.

[63] R. J. Green, H. Joshi, M. D. Higgins, and M. S. Leeson, "Recent developments in indoor optical wireless [Optical wireless communications]," *IET Communications*, vol. 2, no. 1, pp. 3-10, 2008.

[64] P. A. Haigh, T. T. Son, E. Bentley, Z. Ghassemlooy, H. L. Minh, and L. Chao, "Development of a visible light communications system for optical wireless local area networks," in *2012 Computing, Communications and Applications Conference*, 2012, pp. 351-355.

[65] I. S. Jang, J. D. Jeong, M. S. Kim, I. Kim, S. K. Lim, and T. K. Kang, "Implementation of VLC transmitter using MCU for promotion lighting ID services," in *16th International Conference on Advanced Communication Technology*, 2014, pp. 1012-1016.

[66] W. Jiayuan, K. Zhe, and Z. Nianyu, "Research on indoor visible light communication system employing white LED lightings," in *IET International Conference on Communication Technology and Application (ICCTA 2011)*, 2011, pp. 934-937.

[67] J. Grubor, S. Randel, K. D. Langer, and J. W. Walewski, "Broadband information broadcasting using LED-based interior lighting," *Journal of Lightwave Technology*, vol. 26, no. 24, pp. 3883-3892, 2008.

[68] S. Natasha, S. Muhammad, V. Charusluk, S. Poompat, and W. S. Mohammed, "Demonstration of visible light communications using RGB LEDs in an indoor environment," in *ECTI-CON2010: The 2010 ECTI International Confernce on Electrical Engineering/Electronics, Computer, Telecommunications and Information Technology*, 2010, pp. 1159-1163.

[69] W. Fang-Ming, L. Chun-Ting, W. Chia-Chien, C. Cheng-Wei, C. Zhen-Yu, and H. Hou-Tzu, "3.22-Gb/s WDM visible light communication of a single RGB LED employing carrier-less amplitude and phase modulation," in *2013 Optical Fiber Communication Conference and Exposition and the National Fiber Optic Engineers Conference (OFC/NFOEC)*, 2013, pp. 1-3.

[70] Y. Se-Hoon, K. Hyun-Seung, S. Yong-Hwan, and H. Sang-Kook, "Reduction of optical interference by wavelength filtering in RGB-LED based indoor VLC system," in *16th Opto-Electronics and Communications Conference*, 2011, pp. 551-552.

[71] D. color. (02/10/2017). *RGBLEDs spectra*. Available: https://dot-color.com/2011/10/18/quantum-dots-unleash-high-color-gamut-performance-in-led-backlit-displays/

[72] G. Cossu, A. M. Khalid, P. Choudhury, R. Corsini, and E. Ciaramella, "3.4 Gbit/s visible optical wireless transmission based on RGB LED," (in eng), *Opt Express,* vol. 20, no. 26, pp. B501-6, Dec 10 2012.

[73] G. Cossu, R. Corsini, and E. Ciaramella, "High-speed bi-directional optical wireless system in non-directed line-of-sight configuration," *Journal of Lightwave Technology,* vol. 32, no. 10, pp. 2035-2040, 2014.

[74] A. Paraskevopoulos, J. Vučić, S. H. Voß, R. Swoboda, and K. D. Langer, "Optical wireless communication systems in the Mb/s to Gb/s range, suitable for industrial applications," *IEEE/ASME Transactions on Mechatronics,* vol. 15, no. 4, pp. 541-547, 2010.

[75] T. Komine and M. Nakagawa, "Fundamental analysis for visible-light communication system using LED lights," *Consumer Electronics, IEEE Transactions on,* vol. 50, no. 1, pp. 100-107, 2004.

[76] J. H. Choi, S. W. Koo, and J. Y. Kim, "Influence of optical path difference on visible light communication systems," in *2009 9th International Symposium on Communications and Information Technology*, 2009, pp. 1247-1251.

[77] T. Komine, J. H. Lee, S. Haruyama, and M. Nakagawa, "Adaptive equalization system for visible light wireless communication utilizing multiple white LED lighting equipment," *IEEE Transactions on Wireless Communications,* vol. 8, no. 6, pp. 2892-2900, 2009.

[78] J. M. Kahn and J. R. Barry, "Wireless infrared communications," *Proceedings of the IEEE,* vol. 85, no. 2, pp. 265-298, 1997.

[79] Y. Chen, C. W. Sung, S.-W. Ho, and W. S. Wong, "BER analysis for interfering visible light communication systems," in *Communication Systems, Networks and Digital Signal Processing (CSNDSP), 2016 10th International Symposium on IEEE,* 2016, pp. 1-6.

[80] S. Hranilovic, *Wireless optical communication systems*. Springer Science & Business Media, 2006.

[81] P. H. Pathak, X. Feng, P. Hu, and P. Mohapatra, "Visible light communication, networking, and sensing: A survey, potential and challenges," *IEEE communications surveys & tutorials,* vol. 17, no. 4, pp. 2047-2077, 2015.

[82] J. Grubor, S. C. J. Lee, K. D. Langer, T. Koonen, and J. W. Walewski, "Wireless high-speed data transmission with phosphorescent white-light LEDs," in *33rd European Conference and Exhibition of Optical Communication - Post-Deadline Papers (published 2008)*, 2007, pp. 1-2.

[83] D. Zwillinger, "Differential PPM has a higher throughput than PPM for the band-limited and average-power-limited optical channel," *IEEE transactions on information theory,* vol. 34, no. 5, pp. 1269-1273, 1988.

[84] K.-I. Ahn and J. K. Kwon, "Capacity analysis of M-PAM inverse source coding in visible light communications," *Journal of Lightwave Technology,* vol. 30, no. 10, pp. 1399-1404, 2012.

[85] L. Grobe and K.-D. Langer, "Block-based PAM with frequency domain equalization in visible light communications," in *Globecom Workshops (GC Wkshps), 2013 IEEE,* 2013, pp. 1070-1075: IEEE.

[86] H. Sugiyama, S. Haruyama, and M. Nakagawa, "Brightness control methods for illumination and visible-light communication systems," in *Wireless and Mobile*

Communications, 2007. ICWMC'07. Third International Conference on, 2007, pp. 78-78: IEEE.

[87] E. Cho *et al.*, "NRZ-OOK signaling with LED dimming for visible light communication link," in *Networks and Optical Communications (NOC), 2011 16th European Conference on*, 2011, pp. 32-35: IEEE.

[88] G. Ntogari, T. Kamalakis, J. Walewski, and T. Sphicopoulos, "Combining illumination dimming based on pulse-width modulation with visible-light communications based on discrete multitone," *Journal of Optical Communications and Networking*, vol. 3, no. 1, pp. 56-65, 2011.

[89] H.-J. Jang, J.-H. Choi, Z. Ghassemlooy, and C. G. Lee, "PWM-based PPM format for dimming control in visible light communication system," in *Communication Systems, Networks & Digital Signal Processing (CSNDSP), 2012 8th International Symposium on*, 2012, pp. 1-5: IEEE.

[90] K. Raveendranathan, *Communication systems modelling and simulation: using MATLAB and Simulink*. Universities Press, 2011.

[91] D. Falconer, "Carrierless Am/Pm," *Bell Laboratories, NJ, USA, Bell Laboratories Technical Memorandum, Tech. Rep*, 1975.

[92] J. Zhang, J. Yu, F. Li, N. Chi, Z. Dong, and X. Li, "11× 5× 9.3 Gb/s WDM-CAP-PON based on optical single-side band multi-level multi-band carrier-less amplitude and phase modulation with direct detection," *Optics express*, vol. 21, no. 16, pp. 18842-18848, 2013.

[93] M. I. Olmedo, T. Zuo, J. B. Jensen, Q. Zhong, X. Xu, and I. T. Monroy, "Towards 400GBASE 4-lane solution using direct detection of multiCAP signal in 14 GHz bandwidth per lane," in *Optical Fiber Communication Conference and Exposition and the National Fiber Optic Engineers Conference (OFC/NFOEC), 2013*, 2013, pp. 1-3.

[94] L. Tao, Y. Wang, Y. Gao, A. P. T. Lau, N. Chi, and C. Lu, "Experimental demonstration of 10 Gb/s multi-level carrier-less amplitude and phase modulation for short range optical communication systems," *Optics express*, vol. 21, no. 5, pp. 6459-6465, 2013.

[95] R. Rodes *et al.*, "Carrierless amplitude phase modulation of VCSEL with 4 bit/s/Hz spectral efficiency for use in WDM-PON," *Optics express*, vol. 19, no. 27, pp. 26551-26556, 2011.

[96] M. I. Olmedo *et al.*, "Multiband carrierless amplitude phase modulation for high capacity optical data links," *Journal of Lightwave Technology*, vol. 32, no. 4, pp. 798-804, 2014.

[97] M. Zhang and Z. Zhang, "An optimum DC-biasing for DCO-OFDM system," *IEEE Communications Letters*, vol. 18, no. 8, pp. 1351-1354, 2014.

[98] J. Armstrong and A. Lowery, "Power efficient optical OFDM," *Electronics Letters*, vol. 42, no. 6, pp. 370-372, 2006.

[99] S. C. J. Lee, S. Randel, F. Breyer, and A. M. Koonen, "PAM-DMT for intensity-modulated and direct-detection optical communication systems," *IEEE Photonics Technology Letters*, vol. 21, no. 23, pp. 1749-1751, 2009.

[100] V. S. C. Teichmann, A. N. Barreto, T. T. Pham, R. Rodes, I. T. Monroy, and D. A. A. Mello, "SC-FDE for MMF short reach optical interconnects using directly modulated 850 nm VCSELs," *Opt. Express*, vol. 20, no. 23, pp. 369-25377, 2012.

[101] A. F. Shalash and K. K. Parhi, "Multidimensional carrierless AM/PM systems for digital subscriber loops," *IEEE Transactions on Communications*, vol. 47, no. 11, pp. 1655-1667, 1999.

[102] "Asymmetric digital subscriber line (ADSL) transceivers," *ITU-T Recommendation G. 992.1, June*, 1999.

[103] J. L. Wei, L. Geng, R. V. Penty, I. H. White, and D. G. Cunningham, "100 Gigabit Ethernet transmission enabled by carrierless amplitude and phase modulation using QAM receivers," in *Optical Fiber Communication Conference and Exposition and the National Fiber Optic Engineers Conference (OFC/NFOEC), 2013*, 2013, pp. 1-3.

[104] R. Rodes, M. Wieckowski, T. T. Pham, J. B. Jensen, and I. T. Monroy, "VCSEL-based DWDM PON with 4 bit/s/Hz spectral efficiency using carrierless amplitude phase modulation," in *Optical Communication (ECOC), 2011 37th European Conference and Exhibition on*, 2011, pp. 1-3.

[105] P. A. Haigh *et al.*, "Multi-band carrier-less amplitude and phase modulation for bandlimited visible light communications systems," *IEEE Wireless Communications*, vol. 22, no. 2, pp. 46-53, 2015.

[106] K. Gentile, "The care and feeding of digital, pulse-shaping filters," *RF DESIGN*, vol. 25, no. 4, pp. 50-58, 2002.

[107] S. Daumont, B. Rihawi, and Y. Lout, "Root-raised cosine filter influences on PAPR distribution of single carrier signals," in *Communications, Control and Signal Processing, 2008. ISCCSP 2008. 3rd International Symposium on*, 2008, pp. 841-845: IEEE.

[108] C. Langton. *Inter symbol interference and root raised cosine filtering*. Available: http://complextoreal.com/tutorials/tutorial-14-inter-symbol-interference-isi-and-raised-cosine-filtering/#.Wk0RmDenzcs

[109] P. A. Haigh *et al.*, "Multi-band carrier-less amplitude and phase modulation for highly bandlimited visible light communications; Invited paper," in *Wireless Communications & Signal Processing (WCSP), 2015 International Conference*, 2015, pp. 1-5.

[110] R. Schmogrow *et al.*, "Error vector magnitude as a performance measure for advanced modulation formats," *IEEE Photonics Technology Letters*, vol. 24, no. 1, pp. 61-63, 2012.

[111] R. A. Shafik, M. S. Rahman, and A. R. Islam, "On the extended relationships among EVM, BER and SNR as performance metrics," in *2006 International Conference on Electrical and Computer Engineering*, 2006, pp. 408-411.

[112] H. A. Mahmoud and H. Arslan, "Error vector magnitude to SNR conversion for nondata-aided receivers," *IEEE Transactions on Wireless Communications*, vol. 8, no. 5, 2009.

[113] J. G. Proakis, *Digital Communications*. New York: McGraw-Hill, 2004.

[114] N. Chi, Y. Zhou, S. Liang, F. Wang, J. Li, and Y. Wang, "Enabling technologies for high speed visible light communication employing CAP modulation," *Journal of Lightwave Technology*, 2017.

[115] J. G. Proakis, M. Salehi, N. Zhou, and X. Li, *Communication systems engineering*. Prentice-hall Englewood Cliffs, 1994.

[116] S. Haykin, *Adaptive Filter Theory*. New Jersy, USA: Prentice Hall International, 2001.

[117] E. Biglieri, J. Proakis, and S. Shamai, "Fading channels: information-theoretic and communications aspects," *IEEE Transactions on Information Theory,* vol. 44, no. 6, pp. 2619-2692, 1998.

[118] L. Honglei, C. Xiongbin, H. Beiju, T. Danying, and C. Hongda, "High bandwidth visible light communications based on a post-equalization circuit," *Photonics Technology Letters, IEEE,* vol. 26, no. 2, pp. 119-122, 2014.

[119] K. Bandara and C. Yeon-Ho, "Reduced training sequence using RLS adaptive algorithm with decision feedback equalizer in indoor Visible Light Wireless Communication channel," in *ICT Convergence (ICTC), 2012 International Conference on*, 2012, pp. 149-154.

[120] K. Werfli *et al.*, "Multi-band carrier-less amplitude and phase modulation with decision feedback equalization for bandlimited VLC systems," in *Optical Wireless Communications (IWOW), 2015 4th International Workshop*, 2015, pp. 6-10.

[121] R. Kruglov, S. Loquai, C. A. Bunge, M. Schueppert, J. Vinogradov, and O. Ziemann, "Comparison of PAM and CAP modulation schemes for data transmission over SI-POF," *Photonics Technology Letters, IEEE,* vol. 25, no. 23, pp. 2293-2296, 2013.

[122] P. Chvojka *et al.*, "On the m-CAP performance with different pulse shaping filters parameters for visible light communications," *IEEE Photonics Journal,* vol. 9, no. 5, pp. 1-12, 2017.

[123] K. Werfli, P. A. Haigh, Z. Ghassemlooy, N. B. Hassan, and S. Zvanovec, "A new concept of multi-band carrier-less amplitude and phase modulation for bandlimited visible light communications," in *2016 10th International Symposium on Communication Systems, Networks and Digital Signal Processing (CSNDSP)*, 2016, pp. 1-5.

[124] B. Sklar, *Digital communications fundamentals and applications*. Prentice Hall Upper Saddle River, 2001.

[125] P. Chvojka, S. Zvanovec, K. Werfli, P. A. Haigh, and Z. Ghassemlooy, "Variable m-CAP for bandlimited visible light communications," in *Communications Workshops (ICC Workshops), 2017 IEEE International Conference on*, 2017, pp. 1-5.

[126] P. A. Haigh *et al.*, "A MIMO-ANN system for increasing data rates in organic visible light communications systems," in *2013 IEEE International Conference on Communications (ICC)*, 2013, pp. 5322-5327.

[127] L. Zeng *et al.*, "High data rate multiple input multiple output (MIMO) optical wireless communications using white LED lighting," *IEEE Journal on Selected Areas in Communications,* vol. 27, no. 9, pp. 1654-1662, 2009.

[128] A. Burton, H. L. Minh, Z. Ghassemlooy, E. Bentley, and C. Botella, "Experimental demonstration of 50-Mb/s visible light communications using 4 × 4 MIMO," *IEEE Photonics Technology Letters,* vol. 26, no. 9, pp. 945-948, 2014.

[129] N. Giordano, *College Physics*. Nelson Education, 2012.

[130] T. Q. Wang, Y. A. Sekercioglu, and J. Armstrong, "Hemispherical lens based imaging receiver for MIMO optical wireless communications," in *Globecom Workshops (GC Wkshps), IEEE*, 2012, pp. 1239-1243.